LYOTROPIC LIQUID CRYSTALLINE MESOPHASES FROM ACID-SALT-SURFACTANT SYSTEMS: SYNTHESIS AND CHARACTERIZATION OF MESOPOROUS $LiMPO_4$ (M=Mn(II),Fe(II),Co(II) AND Ni(II))

A THESIS SUBMITTED TO

THE GRADUATE SCHOOL OF ENGINEERING AND SCIENCE

OF BILKENT UNIVERSITY

IN PARTIAL FULFILLMENT OF THE REQUIREMENTS FOR

THE DEGREE OF

MASTER OF SCIENCE

IN

CHEMISTRY

By

Işıl Uzunok

September 2019

LYOTROPIC LIQUID CRYSTALLINE MESOPHASES FROM ACID-SALT-SURFACTANT SYSTEMS: SYNTHESIS AND CHARACTERIZATION OF MESOPOROUS $LiMPO_4$ (M=Mn(II),Fe(II),Co(II) AND Ni(II))

By Işıl Uzunok

September 2019

We certify that we have read this thesis and that in our opinion it is fully adequate, in scope and in quality, as a thesis for the degree of Master of Science.

_____

Ömer Dağ (Advisor)

_____

Ceyhan Kayran İşçi

_____

Ayşen Yılmaz

_____

Ferdi Karadaş

_____

Burak Ülgüt

Approved for the Graduate School of Engineering and Science:

_____

Ezhan Karaşan

Director of the Graduate School

ABSTRACT

LYOTROPIC LIQUID CRYSTALLINE MESOPHASES FROM ACID-SALT-SURFACTANT SYSTEMS: SYNTHESIS AND CHARACTERIZATION OF MESOPOROUS $LiMPO_4$ (M=Mn(II),Fe(II),Co(II) AND Ni(II))

Işıl Uzunok

M. S. in Chemistry

Advisor: Ömer Dağ

September 2019

This study presents the synthesis and characterization of mesoporous lithium metal phosphates (LMPs) of Mn(II), Fe(II), Co(II), and Ni(II). The LMPs were synthesized using a modified molten salt self-assembly (MASA) method. Clear and homogeneous solutions of lithium nitrate ($LiNO_3$), transition metal nitrate ($[M(H_2O)_6](NO_3)_2$, phosphoric acid (H_3PO_4, PA), and surfactant (pluronic P123, $EO_{20}PO_{70}EO_{20}$, where EO is ethylene oxide and PO is propylene oxide) in water were spread on a microscope slide by drop-cast coating method to from a lyotropic liquid crystalline (LLC) mesophase. The mesophases were characterized using polarized optic microscope (POM) and x-ray diffractrometer (XRD) techniques. In the mesophase, the mole ratio of the inorganic components was kept constant (1:1:1, Li(I):M(II):PA) but the inorganic ingredient (lithium salt, transition metal salt, and PA) to surfactant mole ratios were varied from 10 to 90. The mesophases are ordered and diffract at small angles in all compositions. However, the mesophases slowly undergo transformation from LLC mesophase to semisolid mesostructured particles by the hydrolysis of PA and LMP formation over time.

The drop-cast coated samples were calcined to produce mesoporous LMPs. The samples were characterized using N_2 adsorption-desorption, XRD, scanning electron microscopy (SEM), transmission electron microscopy (TEM), and Attenuated total

reflectance - fourier-transform infrared spectroscopy (ATR-FTIR) techniques. The LMPs are amorphous up to 400 ^{o}C but become crystalline above this temperature. The amorphous mesoporous LMPs have large Brunauer, Emmett and Teller (BET) surface area, around 30-100 m^2/g but drops down to a few m^2/g upon annealing at 500 ^{o}C. The SEM images show that the particle morphology depends on the inorganic/surfactant ratio in the initial mesophase.

Both Mn(II) and Co(II) produce the olivine phase of $LiMnPO_4$ (LMnP) and $LiCoPO_4$ (LCoP), respectively, under our reaction conditions. However, Ni(II) samples need either excess lithium source or adjustment of pH of the clear solutions to form olivine phase of $LiNiPO_4$ (LNiP). This adjustment can be done by using LiH_2PO_4 as the Li(I) and phosphate source in place of $LiNO_3$ and PA. Unlike iron compound, the olivine phases of LMPs of Mn(II), Co(II) and Ni(II) were successfully obtained. In the iron case, it is difficult to keep iron in 2+ oxidation state under our reaction conditions. It undergoes an oxidation to form Fe^{3+} species. Therefore, mesoporous $FePO_4$ and $Li_3Fe_2(PO_4)_3$ materials were synthesized, where the iron has 3+ oxidation state.

Most synthesis has been carried out over glass slides that simply contain 16% of sodium. We found that our samples undergo Na^+ ion-exchange reaction with the glass substrates above 300 ^{o}C. Therefore, the samples were first calcined at 300 ^{o}C over glass substrates and further annealed at higher temperatures in alumina sample holder to produce mesoporous forms. However, if the annealing step is carried over the glass slides, sodium metal phosphates (NaMPs) form in maricite phase. These samples were also characterized by XRD, SEM, TEM, and ATR-FTIR techniques. To eliminate the ion-exchange reactions, other substrates like quartz, pyrex or fluorine doped tin oxide (FTO) were used. However, notice that ion-exchange can also be performed to synthesize mesoporous maricite NaMPs as another synthesis method.

Keywords: Mesoporous Materials, Lyotropic Liquid Crystals, Lithium Metal Phosphate, Molten-Salt-Assisted Self-Assembly.

ÖZET

ASİT-TUZ-YÜZEY AKTİF MADDE KARIŞIMLARINDAN ELDE EDİLEN LİYOTROPİK SIVI KRİSTAL ARAFAZLAR: MEZOGÖZENEKLİ $LiMPO_4$' LERİN (M=Mn(II),Fe(II),Co(II) VE Ni(II)) SENTEZİ VE KARAKTERİZASYONU

Işıl Uzunok

Kimya, Yüksek Lisans

Tez Danışmanı: Ömer Dağ

Eylül, 2019

Bu tez çalışması, Mn(II), Fe(II) Co(II) ve Ni(II) mezogözenekli lityum metal fosfatlarının (LMPs) sentez ve karakterizasyonu üzerine bir çalışmadır. LMPs eriyik tuz yardımlı kendiliğinden oluşma yöntemi (MASA) modifiye edilerek sentezlenmiştir. Liyotropik sıvı kristal (LSK) arafazları, lityum nitrat ($LiNO_3$), geçiş metal nitrat ($[M(H_2O)_6](NO_3)_2$) tuzları, fosforik asit (H_3PO_4, PA) ve yüzey aktif madde (pluronik P123, EO etilen oksit ve PO propilen oksit, $EO_{20}PO_{70}EO_{20}$) maddelerinin suda hazırlanmış saydam ve homojen çözeltilerinin mikroskop camı üzerine damlatma ve yayma metodu ile hazırlanmış; POM ve XRD teknikleri kullanılarak karakterize edilmişlerdir. Arafazda, anorganic bileşenlerin mol oranı sabit tutulurken (1:1:1, Li(I):M(II):PA), anorganik bileşenlerin (lityum tuz, geçiş metali tuzu ve PA) yüzey aktif maddeye oranı 10'dan 90'a değiştilmiştir. Arafazlar düzenli ve bütün oranlarda x-ışınlarının küçük açılarda kırar. Fakat bu arafazlar zamanla PA hidrolizi ve LMP'lerin oluşumu ile yavaşça LSK arafazdan yarıkatı haldeki arayapılı taneciklere dönüşür.

Mezogözenekli LMP'leri üretmek için, damlatma yöntemiyle hazırlanmış örnekler, kalsine edilmiştir. Bu örnekler N_2 adsorpsiyon-desorpsiyon yöntemi, XRD, SEM, TEM ve ATR-FTIR teknikleri kullanılarak karakterize edilmiştir. LMP'ler 400 ^oC'ye kadar amorftur; fakat bu derecenin üstüne çıkıldığında ise kristal hallerine

dönüşürler. Amorf mezogözenekli LMP'ler, 30-100 m^2/g civarında yüksek BET (Brunauer, Emmett and Teller) yüzey alanına sahiptirler; fakat bu yüzey alanı, sıcaklık 500 ^oC civarına getirildiğinde daha küçüktür. SEM görüntüleri gösteriyor ki, tanecik morfolojisi başlangıç arafazındaki anorganik/yüzey aktif madde oranına bağlıdır.

Mn(II) ve Co(II) maddeleri sırasıyla $LiMnPO_4$ (LMnP) ve $LiCoPO_4$ (LCoP) maddelerinin olivin fazları bizim sağladığımız tepkime koşullarında oluşturulmuştur. Fakat $LiNiPO_4$ (LNiP) maddesinin olivin fazını oluşturmak için, Ni(II) örnekleri, ya fazladan lityum kaynağı kullanımına ya da saydam çözeltilerin pH ayarlanmasına ihtiyaç duyar. Bu pH ayarlaması, $LiNO_3$ ve PA yerine, Li(I) ve fosfat kaynağı olarak LiH_2PO_4 kullanılarak yapılabilir. Demir örnekleri dışında, Mn(II), Co(II) ve Ni(II)'lerin LMP'lerinin olivin fazları elde edilmiştir. Demirli örneklerde, oluşturduğumuz tepkime koşullarında demiri 2+ yükseltgenme basamağında korumak zor olduğundan, demir oksidasyona uğrayarak Fe^{3+} türlerini oluşturur. Bu sebeple, mezogözenekli, demirin 3+ yükseltgenme basamağında olduğu $FePO_4$ ve $Li_3Fe_2(PO_4)_3$ materyalleri sentezlenmiştir.

Çoğu sentez, %16'sını sodyumun oluşturduğu mikroskop cam üzerinde gerçekleştirilmiştir. 300 ^oC üzerindeki sıcaklıklarda, mikroskop camı üzerinde hazırlanan örnekler ile cam arasında Na^+ iyon-değişim tepkimelerinin meydana geldiği belirlenmiştir. Bu sebeple, ilk olarak örnekler yine mikroskop camları üzerinde 300 ^oC sıcaklıkta kalsine edildi ve daha sonra alumina kap içinde, mezogözenekli formlarını oluşturmak için daha yüksek sıcaklığa çıkarıldı. Fakat sıcaklık artırma adımı alumina kap yerine mikroskop camı üzerinde yapılırsa, marisit faz halindeki sodyum metal fosfatlar (NaMPs) oluşmaktadır. Bu örnekler, XRD, SEM, TEM ve ATR-FTIR teknikleri kullanılarak karakterize edilmiştir. İyon-değişim tepkimelerini engellemek için kaplanan yüzey olarak quartz, pyrex ya da FTO kullanıldı. Fakat iyon-değişim tepkimesi mezogözenekli marisit NaMPs maddesini sentezlemek için başka bir sentez metodu olarak kullanılabileceği de not edilmelidir.

Anahtar kelimeler: Mezogözenekli malzemeler, Liyotropik Sıvı Kristaller, Lityum Metal Fosfat, Eriyik Tuz Yardımlı Kendiliğinden Oluşma.

Acknowledgement

I, firstly, would like to thank to my supervisor Ömer Dağ for all of his support and guidance. Since the beginning from my third year of bachelor, he taught me all academic way of thinking. When I needed help throughout my senior and master studies, he was always there to solve my problems and guide me through.

I thank TÜBİTAK for financial support during my master education under the project number 215Z193.

I also thank to my all group members, who are Ezgi Yılmaz Topuzlu, Nesibe Akmanşen, Işık Tunçay, Mete Turgut and Guvanch Gurbandurdyyev for their collaborations and supports in any time. I am appreciated for friendship of my another group member, Assel Amirzhanova as we had time to have fun together in lab and also out of lab. In addition to my current group members, I would like to thank to my old group members; especially Gülbahar Saat to teach me all things about lab operations and my senior studies, Tuluhan Olcayto Çolak, Muammer Yusuf Yaman, and Nüveyre Canbolat. I cannot ignore supports of my classmates who are Merve Yence and Selin Ezgi Dönmez. I also want to thank Kerem Emre Ercan for helping us in Jordan throughout our data measurement and analysis.

I cannot thank Irmak Karakaya enough for her unbelievable support. She is not just my lab mate, but also she is my old roommate, current home mate, in short she was my everything during all of my Bilkent years. I could not be that successful if she were not my friend.

I am sincerely grateful that I have a perfect family, my mom İkbal Uzunok, my dad Rafet Uzunok and my brother Rıfatcan Uzunok for always being with me throughout all my academic life. I cannot payback their sacrifices for me in all my hard times. Also, I want to thank to my sister from another mother, Ayşe Sezgin, to share experiences from her own thesis and she leaded me to win the poster presentation award.

I have special thanks to my dear love, Burak Ulu, for all his patience and hardworking with me during bachelor and master years. He was always there whenever I needed.

Table of Contents

List of Figures

List of Tables

List of Abbreviations

LC : Liquid Crystal

LLC : Lyotropic Liquid Crystal

LMP : Lithium Metal Phosphate

PA : Phosphoric Acid

EISA : Evaporation Induced Self Assembly

MASA : Molten salt Assisted Self Assembly

XRD : X-Ray Diffraction

POM : Polarized Optical Microscopy

SEM : Scanning Electron Microscopy

TEM : Transmission Electron Microscopy

EDX : Energy Dispersive X-Ray Analysis

ATR-FTIR : Attenuated Total Reflection Fourier-Transform Infrared

BET : Brunauer, Emmett and Teller

ICP-MS : Inductively Coupled Plasma Mass Spectrometry

XANES : X-Ray Absorption near Edge Structure

EXAFS : Extended X-Ray Absorption Fine Structure

IUPAC : International Union of Pure and Applied Chemistry

SC : Supercapacitor

MPP : Metal Pyrophosphates

FTO : Fluorine Doped Tin Oxide

CTAB : Cetyltrimethylammonium bromide

Chapter 1

1. Introduction

1.1. Transition Metal Phosphates

High performance batteries are needed for the usage of electronic devices in daily life and for the hybrid technology of automobile industry. To meet the battery requirements, transition metal oxides such as $LiCoO_2$, $LiMn_2O_4$ have been investigated for over a century [1], [2].

This thesis focuses on the synthesis of transition metal phosphates that are also widely employed as cathode materials for the lithium-ion batteries. The reason of choosing these materials for the applications is due to their low cost and having thermodynamic and kinetic stability [1], [3]. Beginning with the studies of Padhi and his coworkers, metal phosphates and lithium metal phosphates have gained significant importance in the field of battery applications. The phosphate based electrode materials, particularly the olivine phase of $LiFePO_4$, $LiMnPO_4$, and mixed $LiMPO_4$ (M is Fe and Mn) can be cycled reversibly between $LiMPO_4$ and MPO_4 at 3.4-4.0 V voltage range [4]. Whittingham et al. showed that of $Fe_{1.33}PO_4OH$ has a very high lithium intercalation capacity even though it is lithium free. They also synthesized vanadium phosphates (H_2VOPO_4) with extra two protons that can be replaced with lithium ions [5].

In addition to $LiFePO_4$, the olivine phase of $LiCoPO_4$ is also considered to be a good candidate for lithium ion batteries [6]. Amine et al. demonstrated that the extraction and insertion of lithium ion to these materials occur at 4.8 V and measured the charge/discharge capacities [6]. Okada et al. have also studied the charge capacities

of $LiCoPO_4$ [7] and found out that $LiCoPO_4$ displays a high discharge plateau (at 4.8 V), reaching a maximum charge capacity of 100 mAh/g after initial 5.1 V charging.

$LiMnPO_4$ has also drawn attention due to its good capacity for the energy application. The olivine phase of $LiMnPO_4$ has been used for charging-discharging experiments in the range of 4.1-4.8 V with an overall reversible capacity of 140 mAh/g [8]. The $LiNiPO_4$ materials have also been investigated by many groups. Deniard et al. have worked on high potential (3-4.8 V) electrochemical cycling of $LiMPO_4$ (where M is Fe, Mn, Co, and Ni). Due to lack of stable electrolytes at such high potentials and need for high voltage charging/discharging of $LiNiPO_4$ most of these materials have been investigated by the DFT calculations [9].

Almost in all studies, olivine phases of the metal phosphates have been the target in the synthesis and applications [10]. In addition to the olivine phase, there is a maricite phase of sodium metal phosphates, which have also been utilized in the energy applications as a cathode material. The difference between olivine and maricite structures is that the olivine phase has higher interest as a cathode material for lithium and sodium ion batteries, whereas the maricite phase is thermodynamically more stable phase of the same compositions [11]. The maricite phase has also been preferred due to its low cost and environmental concerns,[12] like the olivine phase [13].

The maricite phase of metal phosphates is generally used for sodium ion batteries as a positive-electrode material [14], [15]. Actually, the maricite has been discovered from a natural mineral [16]. The maricite phases of $NaMPO_4$s have also been prepared for the hybrid capacitors by solution combustion method [17].

There are many differences between the olivine and maricite structures even though their space groups are same; Pnma orthorhombic. The differences are mostly based on their potential range, phase stability and diffusion barriers. The voltages calculated for Na^+ ion batteries are in the range of 0.18-0.57 V which is lower than the voltages calculated for Li^+ ion batteries. This lower voltage is originated from the cathodic effect of Na^+ insertion, compared to the Li^+ insertion in the material. Based

on these features, the maricite structure is used for Na^+ ion batteries, whereas the olivine structure is preferred for the Li^+ ion batteries [18].

Moreover, there are also differences in structures of olivine and maricite phases based on the locations of the atoms. The maricite structure consists of an alkali metal (generally sodium ion) and a transition metal surrounded by oxygen atoms giving it tetrahedral coordination [16]. Half of the oxygen atoms in the unit cell are bonded to two alkali metals, two transition metal and one phosphorus atom whereas the other half are bonded to three alkali metals, one transition metal and one phosphorus atom [19]. Between the two phases, the position of alkali metal and the position of the transition metal in the olivine phase are reversed in the maricite structure; which makes their structures quite different [20].

The other crucial part is the synthesis methods of lithium transition metal phosphates. There are many different methods to obtain better conductive LMPs in the literature. The earliest and easiest method was performed by Delacourt et al. who tried to synthesize $LiMnPO_4$ powders by one step low temperature route [21]. In that method, they obtained pure and well-crystalline olivine $LiMnPO_4$ powders by simply precipitation from an aqueous media of all ingredients in an arranged pH range. Another group had tried to synthesize olivine phase of $LiMPO_4$ by non-aqueous sol-gel route [22]. In this method, they mixed all chemicals in an organic solvent at room temperature in different mole ratios. The obtained homogenous gels were aged over various time and then heated at higher temperatures to obtain the desired crystals. There is also another general technique for the synthesis of cathode materials, called hydrothermal synthesis [23]. This synthesis method has many steps and uses autoclaves to obtain the crystals of these materials. Polyol method is usually employed to synthesize fine particles of $LiMnPO_4$ [24]. In the polyol method, the metal acetate salt is mixed in a polyol medium that produces quite small crystals. The majority of the synthesis methods produces the bulk materials [25], [26] with a very low surface area; the surface in these non-conductive cathode materials is important for a good conductivity. Therefore, researchers have tried to synthesize porous materials. For this purpose, they generally used a sol-gel method by using acetate or citrate salts of metal ingredients [27]. The obtained xerogel from the sol-gel method

is calcined in an inert atmosphere at 700 ^{o}C. The prepared samples are mixed with carbon and some other active materials to test their activity towards a counter electrode. Carbon containing or coated samples of LMPs, especially $LiFePO_4$, have been analyzed by many groups [28], [29].

1.2. Mesoporous Materials

Porous materials have 3 main classifications based on their pore size; i) microporous materials that have pores smaller than 2 nm, ii) mesoporous materials that have pores in 2-50 nm range, and iii) macroporous materials having pore size higher than 50 nm [30].

Mesoporous materials have high surface area and pore volume, which may provide special conditions and high reactivity in a confined space, such as high interfacial surface, size selectivity for molecules, better ionic and electronic conductivity etc. [31]. These features could be useful for many applications in different fields (such as energy generation, storage and conversion, catalysis, drug delivery, adsorption, and photonics) compared to their bulk materials [32]–[35]. Definition of bulk depends on the type of material and also on the property under question. For instance, electronically, it is the size of an electron-hole pair, exciton Bohr radius. Below this size the electronic property scales with the size of the particle. Therefore, bulk is defined as a size of a material that displays no size-effect on a specific property. Mesoporous materials have pore-wall size usually smaller than Bohr radius of electron-hole pair and display properties depending on the wall-thickness. Therefore, they are important in many applications that the size dependent property may bring new properties and enhanced functions.

First examples of mesoporous materials have been introduced almost 30 years ago on silicates [36]. The discovery of a hexagonally ordered mesoporous silicate began with studies of M41S materials [37], [38] and FSM-16 materials [39], [40]. Later, formation mechanism for silicate rod assembly was proposed using TEM images. [41], [42]. Moreover, effect of different anions to porosity, morphologies, thermal stability, and structures of mesoporous silicates were examined. It has been

established that the Hofmeister series of anions are responsible for the hydrolysis rates of silica species and formation of micelle structures of the surfactants that are used in the assembly process [43], [44]. In addition, rather than direct interactions between surfactants and inorganic species, the surface interactions between silicates and water adsorbed on the surfaces of micelle structures were discussed to elucidate the structure formation in the mesoporous silicates.

The mesoporous silicates have also been investigated by Dag et al. to control the morphology and stability, and also to determine the role of the charged (cethyltrimethylammonium bromide, CTAB) in a non-ionic surfactant (pluronic P123) assembly of mesoporous thin films [45]. These materials have been investigated over several decades to overcome some of their disadvantages due to low thermal stabilities and low chemical reactivity of the mesoporous silicates with amorphous walls [46].

In addition to silica based mesoporous materials that have been studied for a long time by using different silica sources and various types of surfactants, many new methods have also been developed for the synthesis of non-siliceous mesoporous materials [47]. Among the non-siliceous materials, the mesoporous metal oxides have drawn interest due to their useful applications; confinement effect in their nanospace, active surfaces, and well-ordered pore network that make these materials special [48].

There are many examples of mesoporous metal oxides[49] synthesized by soft[50] and hard[51] templating methods in the literature. Also, in our group, some mesoporous metal oxides have been studied for sometimes. Mesoporous transition metal titanates and lithium titanates have been synthesized as thin films by using molten salt assisted self-assembly (MASA) method. The method uses two surfactants, such as CTAB and 10-lauryl ether ($C_{12}EO_{10}$) [52]. First examples of mesoporous $LiCoO_2$ and $LiMn_2O_4$ thin films have also been demonstrated by Dag et al. by using two surfactants systems (10-lauryl ether and CTAB or CTAN, cethyltrimethylammonium nitrate). The salts and surfactants form lyotropic liquid crystalline mesophases (LLCM), in which the salt species are in their molten phase.

The LLCMs have been used to synthesize those materials that have been already employed as electrodes for the electrocatalytic oxidation of water [53].

1.2.1. Hard Templating Methods

In order to synthesize some of the mesoporous materials, hard templating method has been developed as a powerful process for the synthesis of metal oxides. Hard templating process have 3 steps: in the first step, a mesoporous silicate or carbon is synthesized by soft templating method, followed by a calcination to evocate the pores, in the second step, the target precursors are filled into the mesopores of the mesoporous silica or carbon and then heat treated to obtain metal oxide coated silica or carbon and finally in the third step, the first template (silica or carbon) is removed via washing in a highly basic or HF solutions to obtain the mesoporous metal oxides [50]. The process is schematically shown in Figure 1.1.

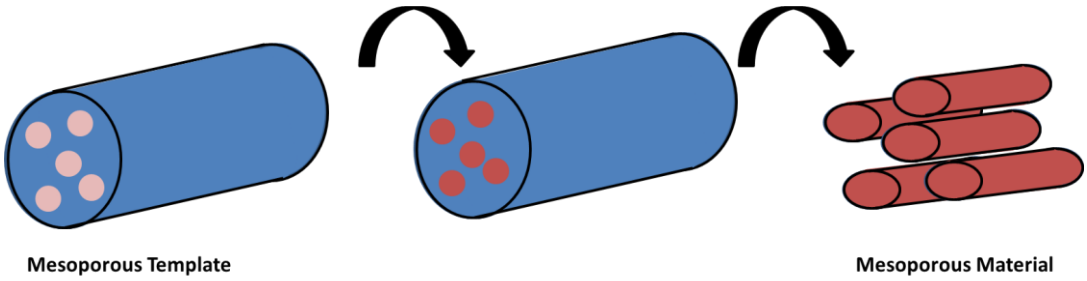

Figure 1.1. Schematic representation of hard-templating method.

Choose of template is very crucial in this method. The template must have ordered mesopores and should be easily removed by washing with an appropriate solution in the last step of the method. For this purpose, generally mesoporous carbon is preferred to produce porous metal oxides by controlling the size and compositions [51].

Besides mesoporous metal oxides, it is also possible to synthesize nanostructured materials with hard-templating method by using siliceous mesoporous templates [54]. Even though, hard-templating is a very powerful method to synthesize mesoporous materials, it is hard to employ for the synthesis of thin films or monoliths. Note that many applications may require thin films or monoliths.

Moreover, the stability of the metal precursors in the pores is also crucial for the synthesis. There should not be any side reactions, such as reaction between the precursors and hard template [48]. Therefore, the hard templating may not be useful for many materials, new soft templating method are needed for the synthesis of those mesoporous materials, such as metal oxides, metal chalcogenites, and metal phosphates.

1.2.2. Soft Templating Methods

Soft-templating method is widely utilized for the synthesis of many mesoporous materials using lyotropic liquid crystalline phase made by surfactants. The hydrophobic and hydrophilic interactions among the surfactant molecules enforces these molecules to aggregate into micelle structure (aggregates of certain number of surfactant molecules forming structure with a shell (hydrophilic) and a core (hydrophobic)). Then the micelles assemble into lyotropic liquid crystalline (LLC) phases. The LLC phase can be used as a media and architecture for the precursors that transform into a mesostructured solid, keeping the meso-order in the product by thermal treatments. In this assembly process, firstly, a clear solution of inorganic ingredients (this could be a silica, titania, or salts precursors) and surfactant is prepared; with the evaporation of the volatile components of the solution a gelation process takes place to obtain the mesophase and finally the mesophase is heated to remove surfactant from the structure by calcination [52] or solvent extraction [55] methods, leaving the mesoporous material behind [50]. Figure 1.2 shows a schematic representation of the soft-templating method.

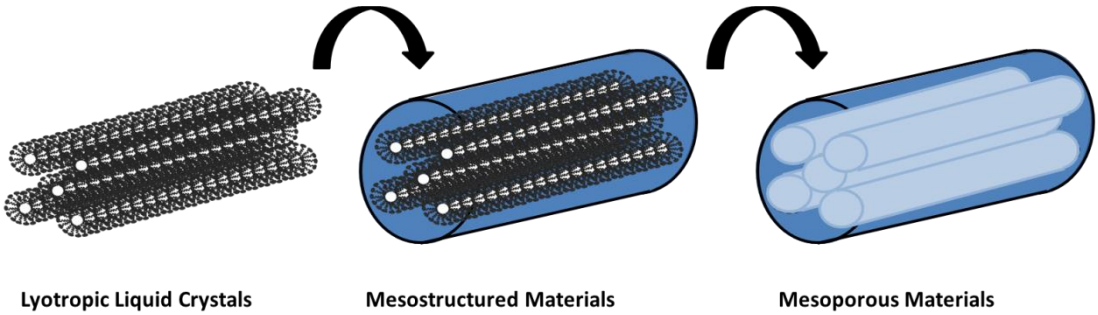

Figure 1.2. Schematic representation of soft-templating method.

Even though, it seems like it is easy to produce mesoporous materials by soft-templating methods, controlling morphology of a desired material is harder than the hard templating method due to condensation or crystallization of the inorganic ingredients during the gelation process and complicated interaction between surfactants and inorganic precursors. This is why most investigation has been devoted to hard-templating method for the synthesis of mesoporous metal oxide materials. The control of morphology is easier in the hard templating method[55].

There are two major processes under the topic of soft-templating method, specifically on the LLC templating approach. First one is evaporation induced self-assembly (EISA) method, discovered by Brinker et al. in 1999 [56]. The EISA is a new method to produce both siliceous and non-siliceous mesoporous metal oxides with an easier and faster way than the hard-templating method. Briker et al. showed that the solution consisting of all the ingredients should not be very concentrated, not to exceed the critical micelle concentration [57]. With the help of low concentration of surfactants and other species, solidified network of mesophase can form easily with the evaporation of the volatile solvent. Solidification process occurs due to the interaction between the surfactant domains and inorganic species. Generally, dip coating method is preferred to obtain solidified phase from the EISA method. The EISA method is easy to apply but unfortunately limited to those materials that their precursors undergo hydrolysis and condensation reaction in the solution and in the mesophase to form a mesostructured solid prior to heat treatment and/or calcination at high temperatures. This method offers to synthesize highly mesoporous ultrathin films of metal oxide [58], such as SiO_2, TiO_2, ZrO_2, etc.. Note that all these materials have their alkoxide precursors ($M(OR)_4$) that are suitable for room temperature hydrolysis and condensation reactions. Moreover, it is also possible to produce mesoporous materials of alumina, titania, and mixed metal oxides ($SrTiO_3$, $MgTa_2O_6$, $Co_xTi_{1-x}O_{2-x}$) via EISA method [59], [60].

Even though there are many advantages of the EISA method due to the usage of low cost and non-toxic species and easy control based on size and morphology of the desired material, there are some disadvantages to take into account. The problems generally originate in the hydrolysis and condensation process of the inorganic

precursors. This also limits the method because many inorganic species do not undergo hydrolysis and condensation reactions under the conditions of the EISA process. Moreover, the system is very sensitive to the humidity of the environment, which affects the assembly and stability of the mesostructure [48], [61], [62]. Therefore, new methods are needed for more challenging precursors, such as some metal oxides, metal sulfides, and metal phosphates, etc.

1.3. Molten Salt Assisted Self Assembly (MASA) Method

A new method for the synthesis of mesoporous materials had been developed by using transition metal nitrates and $C_{12}EO_{10}$ (10-laurly ether) by Dag et al. in 2011. They have used $[Zn(H_2O)_6](NO_3)_2$ and $[Cd(H_2O)_4](NO_3)_2$ salts as inorganic species and $C_{12}EO_{10}$ (non-ionic) and CTAB (ionic) as surfactants and showed that the metal nitrates form a mesostructure by assembling both ionic and non-ionic surfactants. Moreover, they have focused on the metal salts as a secondary solvent in the molten phase, since the mixture of salts and surfactants form LLC phases [63]. As a proof of concept, mesoporous silica metal oxides (such as $CdO\text{-}SiO_2$ and $ZnO\text{-}SiO_2$) have been synthesized and converted into mesoporous metal sulfide (CdS and ZnS) and selenide (CdSe and ZnSe) thin films by H_2S or H_2Se reaction and dilute HF treatments [64].

These studies are the first examples of synthesizing mesoporous materials by MASA (Molten Salt Assisted Self Assembly) method in which two surfactants and two solvents have been utilized. This method has also been used for the synthesis of mesoporous metal titanates (such as $Li_4Ti_5O_{12}$, $MnTiO_3$, $CoTiO_3$, Zn_2TiO_4, $CdTiO_3$) that they could be converted into metal sulfide-titania thin films and monoliths [52], [65].

The most important advantage of the MASA method is keeping the salts in the molten phase as a secondary solvent. The first solvent could be water or ethanol (or a mixture of water and ethanol); the new method offers versatility to produce different mesoporous materials and also processing ability. It helps to control the thickness of coatings of the gel phase over a substrate. For instance, diluter solutions can be used

to make thinner films and more concentrated ones for thicker films. The MASA differs from the EISA method, in which the mesophase is formed by coating of ingredient (metal precursors and surfactant) solution that converts to a solidified mesostructure by polymerization of the inorganic precursor(s) during aging process. However, in most cases in the MASA, aging of the gels produce only stable LLC phases. Further heating may be necessary to produce mesostructured solid in the MASA process. It is more correct to say that the MASA process is applicable for those metal precursors that cannot be hydrolyzed and polymerized at room temperature. Note also that many transition metal oxides precursors are stable salts at room temperature and therefore, they are not good precursors for EISA process. The secondary solvent, salts or acids or salt and acid altogether, organizes the surfactant species in an LLC mesophase. The ionic surfactant in the mesophase stabilizes the mesophases by charge balancing the molten salt-surfactant interface in the LLC phase and also enhances the molten salt up take of the mesophase[63]. To prevent the condensation reactions, in some circumstances nitric acid can be added to the media to protonate the M-OH species in the medium to slow the hydrolysis and condensation process. Uncontrolled condensation reactions most of the time produce bulk or large nanoparticles that may not be organized into mesostructures by surfactant assembly.

1.4. Lyotropic Liquid Crystalline Mesophases

In the previous sections of the introduction, the term lyotropic liquid crystals have been mentioned in almost every stage of the synthesis of mesoporous materials. It will be useful to describe what liquid crystals is and its one common type the lyotropic one to make, what has been achieved in this thesis is, easy to understand.

We have learned from the primary and high schools that there are three states of matter under normal conditions: solid, liquid, and gas. Unfortunately, this is not correct. There is also a fourth phase of matter, called liquid crystalline (LC) phase. The LC phase is a phase having both characteristics of solid and liquid; it has some degree of order like in solid and it has fluidity like liquid. For sure, the order is less than a solid, but more than a liquid. Therefore, the LC phase is also called as

mesophase [66]. The word meso is a Greek word for in between. The mesophase is the phase between liquid and solid (describes liquid crystals) and mesoporous materials are porous materials between microporous and macroporous materials. The term is used together with phase or pores between well know two phases and pores, respectively, to describe some of the new materials.

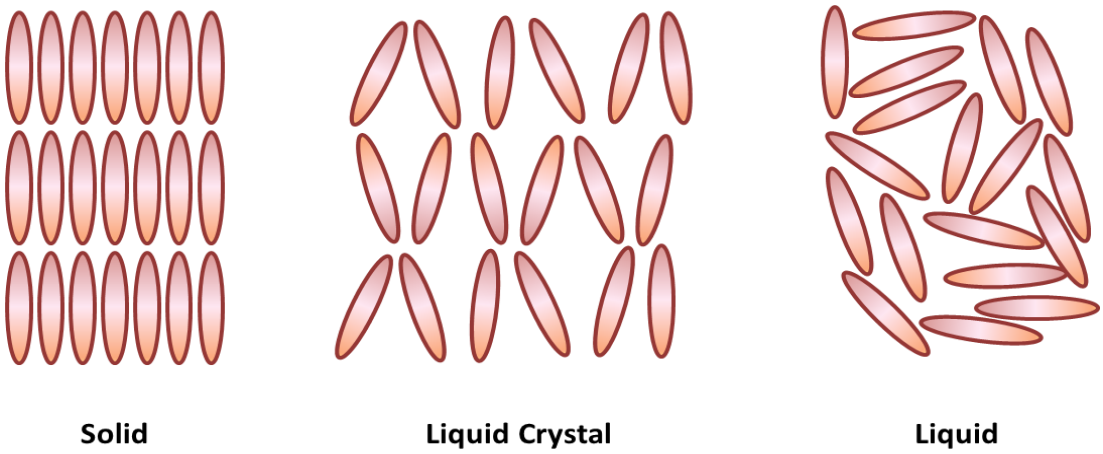

Figure 1.3. Schematic representation of solid, liquid crystal, and liquid phases.

Liquid crystalline phase was first discovered accidentally by Friedrich Reinitzer in 1888, while studying the natural organic compounds based on their melting behaviors [67]. He observed that there is a fuzzy temperature region between the solid and liquid phases of these compounds. These compounds have different melting and freezing points. The different types of LC phases have already been characterized based on their ordered structures.

The LC phases have been divided into two subgroups: i) thermotropic and ii) lyotropic liquid crystals. Thermotropic liquid crystalline phase is observed by heat treatments of certain type of molecular compounds. Those compounds become liquid crystalline in a temperature range and generally form as isotropic LCs [68]. However, the lyotropic liquid crystalline (LLC) mesophases are formed by 2 or more species, one is usually a surfactant and the other is a solvent and also sensitive to temperature. In this thesis, only the LLC phases have been investigated and used, therefore the details of this phase (constructed by micelle building blocks) and the term micellization (important to understand this phase) will be described in detail.

Micelle is a structure formed by amphiphilic molecules called surfactants with the help of solubility difference between the hydrophilic and hydrophobic domains of the surfactant in a solvent. Surfactants are amphiphiles that contains both polar (can be neutral or charged) and a nonpolar block. For instance, CTAB is a charged surfactant and P123 is a tri-block copolymer with ethylene oxide polar (two ends) and non-polar propylene oxide (middle) blocks. In a polar solvent like water, the hydrophilic domains of the surfactant (polar head) interact with the water, whereas the hydrophobic domains (non-polar tail) accommodate on the center of a structure, called micelle.

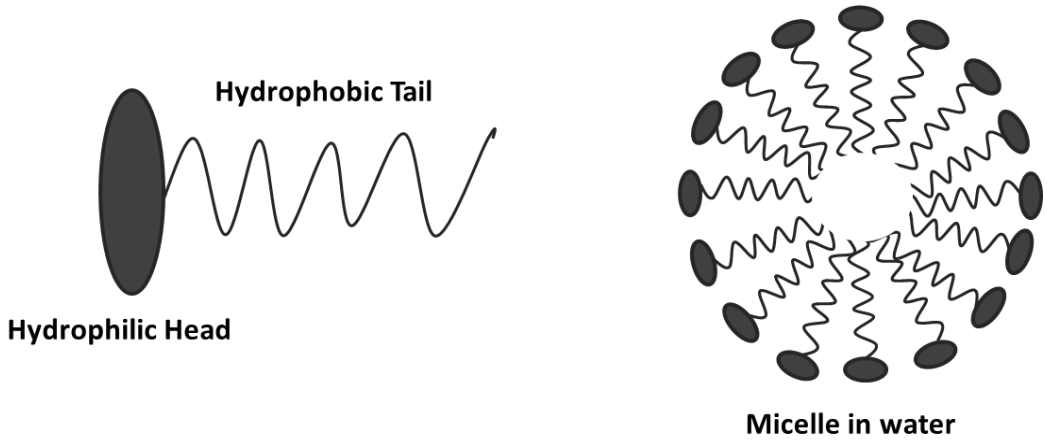

Figure 1.4. Schematic representation of surfactant and a cross-section of a micelle structure in water.

Having optimum surfactant/solvent ratio is called critical micelle concentration (CMC) to obtain assembled micelle structure of surfactants. Further increasing the amount of surfactant in the solution enforces micelles to pack into an LLC mesophase and depending on the amount of surfactant in the mesophase, lamellar, hexagonal, or cubic mesophases form [69].

The LLC mesophases have been used as a template for the synthesis of mesoporous materials. The first example was demonstrated by Kresge et al. in 1992 [38]. Beck et al. used this method to prepare, characterize and show the mechanisms of the silicate/aluminosilicate mesoporous molecular species in 1995 [37]. Attard et al. also firstly synthesized oriented monolithic mesoporous silica by using the liquid crystalline mesophase [70]. Dag et al. reported that self-assemblies between non-

ionic surfactant (10- lauryl ether) and transition metal salts of Co(II), Ni(II), Zn(II), and Cd(II) by showing the LC features at different mole ratios [71]. The LLC have been studied to understand what happens to salts and nonionic surfactant in the mesophase by diffraction, microscopy, and spectroscopy techniques [72]. Our group also worked on the effects of anions to the LLC phase, prepared by surfactant-metal salts. Moreover, they have studied not only the small surfactants but also larger surfactants, like pluronics [73]–[75].

Ionic surfactants have also an important role in the synthesis of mesoporous materials by LLC phases. The ionic surfactants in the liquid crystalline phases provide the charge balance and also increase the amount of salt in the media and stabilize the mesophase. CTAB can be given as an example for the ionic surfactant. By using two surfactants and LLC phase for the synthesis mesoporous materials, Dag et al. introduced the molten salt-assisted self-assembly (MASA) method to the literature by adding salts into the two surfactant LLC phase as mentioned before [63]. Here, the salts are used as a secondary solvent providing a control of the structure of LLC.

1.5. The LLC Mesophase and Mesoporous $LiMPO_4$ (M=Co(II), Mn(II), Fe(II), Ni(II))

In this thesis, a modified MASA method is utilized by changing the charge surfactant, CTAB with phosphoric acid (H_3PO_4) to obtain a stabile LLC mesophase through the H-bonding between acid and surfactant. The purpose of forming stabile LLC phase is to obtain mesoporous $LiMPO_4$, as mentioned that these materials are very important for the lithium ion batteries.

In the literature, there are many examples of usage of LLC phases for the synthesis of various materials and lots of methods to produce LMP for the energy applications, but there is no successful example for the synthesis of mesoporous LMPs yet. Here, the aim of this thesis is to combine all these concepts to synthesize mesoporous LMPs by using the LLC mesophase as a template.

1.6. Lithium to Sodium Exchange

In this thesis, there is also one more term, ion-exchange, needs to be addressed to fully understand what is happening during synthesis of LMPs. We observed an ion-exchange process that occurs between the glass substrate that was used as flat platform for the synthesis and our synthesis products, LMPs. Most glasses, including microscope slide contains sodium ion in their structure and provide strength to glass.

In order to understand the term 'ion-exchange' deeply, the examples of cation exchanges can be examined. Cation exchange has been investigated to obtain new materials by using other materials via exchanging one cation with another one or more [76]. Usually, ion-exchange is carried in solid-solution type media, like zeolite modification by changing framework cations with another cation in the solution phase and ion exchange resins used for water cleaning etc. However, here the ion exchange occurs between two solids. In the chemical transformations, solid-solid reactions take place. Therefore, the reactions are mostly very slow due to the diffusion rates of the ions in the solid phase; it generally requires high temperatures or pressure [77]. This exchange can occur for both bulk and nanocrytalline materials. The exchange in the nanocrytalline structure has been found to be much faster and much controllable based on size, shape, and compositions of the material[78]. Son et al. reported that cation exchange between Ag^{+} and Cd^{2+} ions to obtain nanocrystals of Ag_2Se from CdSe nanoparticles in a methanolic solution of $AgNO_3$ to preserve/transfer the size uniformity and morphology of CdSe into Ag_2Se. Cation exchange is also used for optimizing the CO_2 adsorption properties of metal organic frameworks (MOFs). An et al. demonstrated that the exchange of tetramethylammonium, tetraethylammonium, or tetrabutylammonium cations via post-synthetic cation exchange in MOF to modify the pore dimensions [79].

There are limited examples about the cation exchange of Na^{+} and Li^{+} ions in solid phases. Garfinkel et al. reported that the diffusion profile of the Na^{+} and Li^{+} in Li_2O-Al_2O_3-SiO_2 glass. They analyzed the stress data of the glasses by heating and collecting to obtain diffusion coefficient of these two ions [80]. Similar experiments were done by another group based on the inter diffusion of hydrogen atom and alkali

ions in glass substrates. In an acidic solution, Na^+ ion, in the glass, and hydronium ion in water undergoes ion-exchange to produce H^+ ions in the glass [81].

Ion exchange of Na^+ with Li^+ was also performed in soda-lime glass by using molten salts of Li^+ ion at high temperature (higher than 500 ^oC). They aimed that exchange of Na^+ ion in a soda-lime glass with a smaller ion like Li^+ to have strengthened glass since the diffusion of Li^+ is easy and Li-rich glasses are much stronger. Moreover, they studied the effect of some anions to the ion exchange of Na^+ to Li^+ [82].

The ion exchange of Li^+ with Na^+ in our samples is quite different from those studies. We prepared mesophases of lithium metal phosphates over glass substrates. During calcination or annealing steps, lithium in our samples undergoes exchanged with sodium ion in the glass at higher temperatures.

Chapter 2

2. Experimental Section

2.1. Materials

All materials were supplied from Sigma-Aldrich and used without purification.

Phosphoric acid (85-88% w/w, Sigma-Aldrich) was used as a phosphate precursor and also to stabilize the mesophase. Manganese(II) nitrate tetrahydrate ($[Mn(H_2O)_4](NO_3)_2$ 97%, Sigma-Aldrich), iron(II) chloride tetrahydrate ($[Fe(H_2O)_4]Cl_2$ 99%, Sigma-Aldrich), iron(III) nitrate nonahydrate ($[Fe(H_2O)_6](NO_3)_2.3H_2O$ 99%, Sigma-Aldrich), cobalt(II) nitrate hexahydrate ($[Co(H_2O)_6](NO_3)_2$ 98%, Sigma-Aldrich), nickel(II) nitrate hexahydrate ($[Ni(H_2O)_6](NO_3)_2$ 99.9%, Sigma-Aldrich) were used as metal sources and $LiNO_3$, LiCl, and LiH_2PO_4 (both >99%, Sigma-Aldrich) were used as lithium source and phosphate source. As a surfactant, PEG-PPG-PEG, Pluronic® P-123 (Poly(ethylene glycol)-block-poly(propylene glycol)-block-poly(ethylene glycol), (Mw~5800g/mol) 99.9% Sigma-Aldrich) was used without further treatment.

All ratios for all $LiMPO_4$ amounts are shown below:

For $LiCoPO_4$;

Mole ratio/ingredients	P123	H_3PO_4	$LiNO_3$	$[Co(H_2O)_6](NO_3)_2$
1:10	1 g	0.200 g	0.119 g	0.506 g
1:20	1 g	0.400 g	0.239 g	1.012 g
1:30	1 g	0.600 g	0.359 g	1.518 g
1:40	1 g	0.800 g	0.479 g	2.025 g
1:50	1 g	1.002 g	0.599 g	2.531 g
1:60	1 g	1.201 g	0.719 g	3.037 g
1:70	1 g	1.402 g	0.839 g	3.543 g
1:80	1 g	1.604 g	0.959 g	4.049 g
1:90	1 g	1.804 g	1.079 g	4.555 g

For $LiMnPO_4$;

Mole ratio/ingredients	P123	H_3PO_4	$LiNO_3$	$[Mn(H_2O)_4](NO_3)_2$
1:10	1 g	0.200 g	0.119 g	0.437 g
1:20	1 g	0.400 g	0.239 g	0.873 g
1:30	1 g	0.600 g	0.359g	1.309 g
1:40	1 g	0.800 g	0.479 g	1.746 g
1:50	1 g	1.002 g	0.599 g	2.182 g
1:60	1 g	1.201 g	0.719 g	2.619 g
1:70	1 g	1.402 g	0.839 g	3.055 g
1:80	1 g	1.604 g	0.959 g	3.492 g
1:90	1 g	1.804 g	1.079 g	3.929 g

For $LiNiPO_4$;

Mole ratio/ingredients	P123	H_3PO_4	$LiNO_3$	$[Ni(H_2O)_6](NO_3)_2$
1:30	1 g	0.600 g	0.359 g	1.517 g
1:60	1 g	1.201 g	0.719 g	3.034 g
1:90	1 g	1.804 g	1.079 g	4.552 g

Table 2.1. Amounts of ingredients used for the solutions of given molar ratios for $LiCoPO_4$, $LiMnPO_4$ and $LiNiPO_4$.

For $LiFePO_4$;

Mole ratio/ingredients	P123	H_3PO_4	$LiNO_3$	$[Fe(H_2O)_6](NO_3)_2.3H_2O$
1:30	1 g	0.600 g	0.359 g	1.038 g
1:60	1 g	1.201 g	0.719 g	2.075 g
1:90	1 g	1.804 g	1.079 g	3.112 g

Mole ratio/ingredients	P123	H_3PO_4	LiCl	$[Fe(H_2O)_4]Cl_2$
1:30	1 g	0.600 g	0.221 g	1.038 g
1:60	1 g	1.201 g	0.442 g	2.075 g
1:90	1 g	1.804 g	0.664 g	3.112 g

Table 2.2. Amounts of ingredients used for the solutions of given molar ratios for $LiFePO_4$

2.2.Synthesis of materials

2.2.1. Solution Preparation

The solutions were prepared according to mole of acid/P123 in 10 g of water in 20 ml vials. The amounts of salts ($LiNO_3$, LiCl and $M(NO_3)_2$ (M=Mn(II), Fe(II), Co(II), and Ni(II))) were kept the same as the acid amount. In order to minimize the high concentrated acid effect, for each solution two vials were used. First vial was used to dissolve the salts and half of the required surfactant (0.5 g) in 5 ml of water (solution A), whereas the second vial was used to dissolve the acid and the other half of the surfactant in 5 ml water (solution B). To prepare solution A, first the required amount of salt was dissolved in 5 ml water (takes around 2-3 minutes) and then 0.5 g melted surfactant (at around 80 ^oC) was added and stirred for a night to obtain a homogenous solution. In the second vial, firstly 5 ml water was put and then required amount of acid was added, finally the other portion of the melted surfactant was added and stirred again for one night until solution B became homogenous. These two separate solutions were stirred for about 1 day to dissolve the surfactant completely. These two solutions were mixed after 1 day and stirred for another 1 day until the mixture was a clear and homogeneous solution. If there was any

precipitation in the solutions, they were centrifuged and the precipitate was taken before doing any characterization (it was happening for Mn case, explained in the chapter 3).

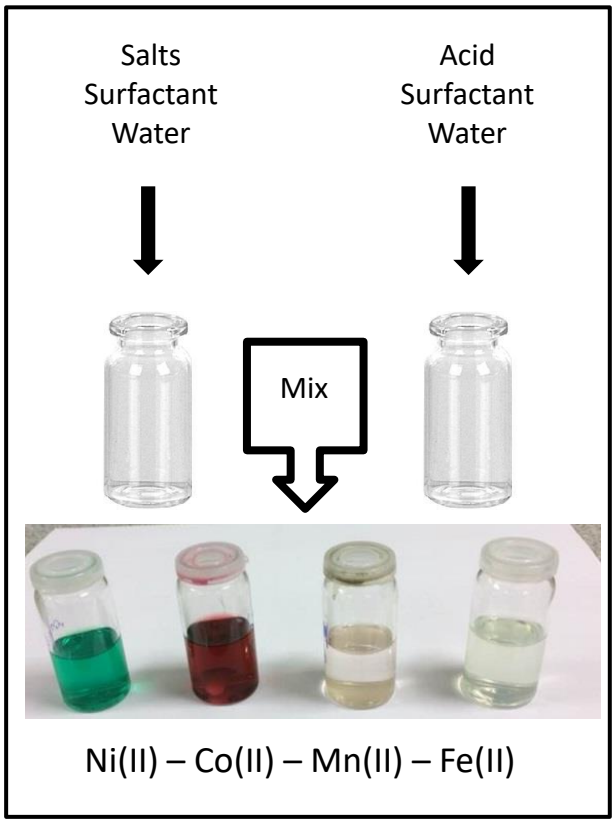

Figure 2.1. Schematic representation of solution preparation

2.2.2. Preparation of Mesophases and Mesoporous Materials

The following general procedure was employed for all metal systems to prepare gel-like mesophases and mesoporous LMPs.

After obtaining homogeneous solutions, they were spin coated (typically at 1500 rpm for 10 sec) or drop-cast coated on the microscope or quartz slides, FTO or petri dishes by spreading a few drops of the solution for further analysis. Spin coated glass slides can be used for calcination process or characterization directly without waiting some time to get rid of the excess water whereas the drop-cast coating samples need further process to evaporate the excess solvent in the samples on the glass substrate. After dropping few droplets from the solution to the glass substrate, excess solution was poured back to the own vial and the gel like thin solution was spread over the

glass to fully cover the glass substrate. Then, it was aged for some time (around 1-2 min) in a vertical position to the bench on a paper towel to obtain homogeneous thick films. These gel-like films were characterized using various techniques (such as ATR-FTIR, XRD, and POM).

The films, drop-cast coated or spin coated, were calcined at different temperatures (mostly 300ºC- 500ºC) in preheated ovens for 1 hour. The calcined samples were scraped from the glass substrate and used for the characterization using XRD, ATR-FTIR, SEM, TEM, XANES, N_2 adsorption-desorption, and ICP-MS techniques.

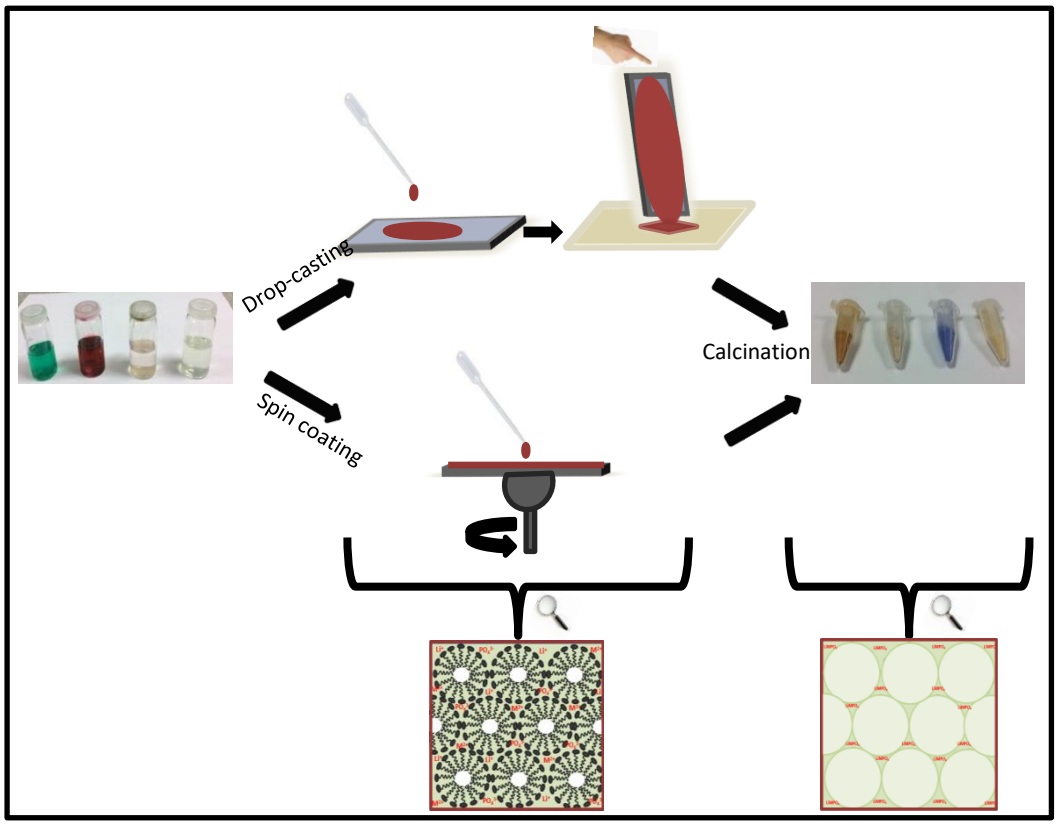

Figure 2.2. Schematic representation of preparation of mesophases and mesopores.

2.3.Instrumentation

2.3.1. X-Ray Diffraction

Small angle (1-5^o) XRD patterns were recorded by a Rigaku Minifle diffractometer equipped with a CuK$_\alpha$ (λ=1.5405 Å) x-rays source, operating at 30 kV/15 mA and a Scintillator NaI (T1) detector with a Be window for the gels on the glass microscope slides. Diffraction measurements were carried by directly inserting the microscope slides into sample holder position. For the wide angle (10-80^o) XRD patterns, Pananalytical Multipurpose x-ray diffractrometer, equipped with a CuK$_\alpha$ (λ = 1.5405 Å) x-rays source operating at 45 kV/40 mA was used to record the XRD patterns of the powder samples, collected from any glass substrate after calcination. Samples were packed uniformly on a silicon wafer.

2.3.2. Attenuated Total Reflection Fourier-Transform Infrared (ATR-FTIR) Spectroscopy

The ATR-FTIR spectra were recorded using a Bruker Alpha Platinum ATR-FTIR spectrometer with a Digi Tect TM DLATGS detector with a resolution of 4 cm^{-1} and 64 scans in 400-4000 cm^{-1} range. The spectra were measured by putting a few drops of solution for the gel phase or a powder sample on the diamond ATR crystal from calcined samples.

2.3.3. Fourier-Transform Infrared (FTIR) Spectroscopy

A Bruker Tensor 27 model FTIR spectrometer with a Digi Tect TM DLATGS detector with a resolution of 4 cm^{-1} and 64 scans in 400-4000 cm^{-1} range was used for recording the FTIR spectra. The powder samples were pressed by mixing with 0.190 g KBr and around 0.01 g of our sample into pallet.

2.3.4. Scanning Electron Microscope (SEM)

The SEM images were recorded using a FEI Quanta 200 FEG at an operating voltage of 15 kV under a high vacuum (about 10^{-6} Torr). The samples were scraped from the glass substrate and put on a carbon tape which attached to the aluminum stub. Furthermore, EDAX data of the samples were collected using the same samples using same microscope.

2.3.5. Transmittance Electron Microscope (TEM)

For the transmittance electron microscope (TEM) images, a FEI Technai G2 F30 was used at an operating voltage of 200kV. For TEM imaging, spin coated and calcined

samples were mostly used. The samples were scraped and grinded well in a mortar using 5 ml of absolute ethanol and dispersed using a sonicator for 30 min. A few drops of the dispersed solution was put on a TEM grid (holey carbon film on 200 mesh cupper grid) and heated under powerful light for drying.

2.3.6. N_2-Adsorption-Desorption Measurements

The N_2 adsorption-desorption (77.4 K) measurements were carried using Micrometerics Tristar 3000 automated gas adsorption analyzer in a relative pressure range, P/P_0 from 0.01 to 0.99 over 5 min intervals. The powder samples collected by strapping from the glass substrate were placed to tube sample holders and dehydrated under vacuum until it reaches to 35-40 mTorr for 2 hrs at 200 ^oC before the N_2 adsorption-desorption measurement. Before the measurements, the sample tubes were also cleaned by washing (with aqua-regia, water, and then ethanol, separately) and evacuated using a vacuum pump so that the weight of the sample was accurately determined. The tubes with dehydrated samples were placed to the instrument with an isothermal jacket to keep the temperature stable inside since the measurement was carried at liquid nitrogen temperature.

2.3.7. ICP-MS (Inductively Coupled Plasma-Mass Spectrometry) Measurements

Concentration determination was done by suing an Agilent 7700x ICP-MS (Agilent Technologies Inc., Tokyo, Japan), equipped with an octopole reaction system and a helium collision cell for spectral interference removal. MicroMist glass concentric nebulizer, quartz Scott-type spray chambers (both from Agilent Technologies, Inc.) and Ni sampler/skimmer cones were operated for the operation of ICP-MS. For the short term stability 1 μg/L tuning solution was used to perform daily instrumental optimization. External calibration solutions were prepared by using Agilent ICP-MS Multi-element calibration standard-2A (Li, Na, Mn, Ni, Fe, Co) and 4 (P). To plot the calibration curves, fourteen points of standard solutions of which the concentrations varies between 10 and 0.78125 ppm were recorded. As a preparation of measured solutions, firstly, 7 mg of powder samples were dissolved in concentrated nitric acid (10 ml) and diluted it to 100 ml with deionized water to optimize the concentration in the range of calibration curves.

2.3.8. Polarized Optic Microscope (POM)

POM images were collected using a ZEISS Axio Scope A1 polarizing optic microscope with different optic lenses (5X, 10X, 20X and 50X) between crossed polarizers to see the mesophases of gels on the microscope slides, prepared by drop-cast coating or spin coating.

2.3.9. X-Ray Absorption Spectroscopy

The XANES and EXAFS measurement were done at the XAFS/XRF beamline of SESAME (Synchrotron-Light for Experimental Science and Applications in the Middle East, Allan, Jordan). The monochromator was set to each element (Ni, Fe, and Co K-edge) for the corresponding samples and the XANES and EXAFS regions were collected with 0.5 eV and 1 eV resolutions, respectively. For the calibration, Ni, Fe and Co metallic foils were used in transmission mode. Each spectrum was repeated 3 times to amplify the signal to noise ratio.

The further analysis (merging, normalization, etc.) of the collected XANES and EXAFS data was carried by using Athena software.

Chapter 3

3. Results and Discussions

3.1. Mesophases of Acid-Surfactant System

3.1.1. Gels of Only P123 and H_3PO_4

The mesophases of acid-salt-surfactant have been only investigated for the phosphoric acid (H_3PO_4, PA)-calcium nitrate-10-lauryl ether ($C_{12}H_{25}(OCH_2CH_2)_{10}OH$, represented as $C_{12}E_{10}$) system by our group [83]. The mesophase of PA-$C_{12}E_{10}$ is also known in the literature from our group's previous work [84]. This thesis expands both mesophases (acid-surfactant and acid-salt-surfactant) to some other metal salts and a pluronic (P123, $(EO_{20}PO_{70}EO_{20}$, EO = ethylene oxide, PO = propylene oxide) in place of $C_{12}E_{10}$. Since there is no investigation on the lyotropic liquid crystalline (LLC) mesophases of phosphoric acid (PA)-pluronic (P123) systems, firstly the PA-P123 mesophases have been prepared and analyzed to establish background information for the synthesis of mesoporous lithium metal phosphates (LMPs). In the acid-salt-P123 system, this thesis is the first example that it brings two salts (lithium salt and a transition metal salt), PA, and P123 together for the synthesis of the LMPs. Previously, lithium nitrate-transition metal nitrate (transition metal is Mn(II), Co(II), or Ni(II))-$C_{12}E_{10}$ have also been investigated by our group [85]. Therefore, P123 has been used and optimized (salt/surfactant ratios, temperature, coating methods) for the synthesis of mesoporous LMPs the first time in this thesis.

For this purpose, P123 was mixed with PA in different mole ratios (see Table 2.1) and homogenized to obtain the PA-P123 LLC mesophases. Simply, the mesophases were prepared by shaking the mixture of all ingredients in a water-bath at 80 ºC for one night. Shaking and heating process was needed, because it is difficult to dissolve surfactant in PA at room temperature. The mixture became homogeneous in the form of a gel LLC, see Figure 3.1 and 3.2.

Figure 3.1. Photos of the homogeneous gels of PA-P123 in vials (from left to right, the PA/P123 mole ratio is changing from 10 to 90 by 10 increments).

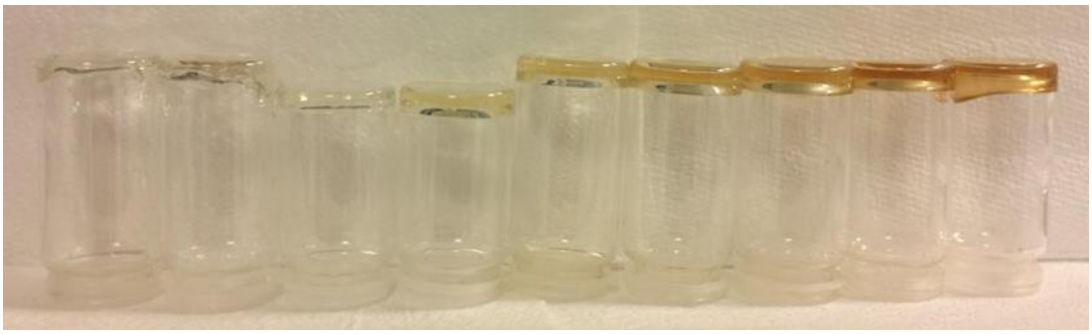

Figure 3.2. Photos the same vials, upside down, of previous figure.

Then, the gels were characterized using XRD and POM techniques. Small angle XRD patterns of the PA-P123 gels were recorded by spreading the gels on microscope slides by applying a sheer force; this ensures a smooth and flat film for the XRD measurement. The small angle XRD patterns show that the LLC mesophases of P123 and PA are formed in all compositions; the XRD patterns show that there is an ordered mesostructure in all compositions. There is no obvious trend among the patterns; the number and shapes of the diffraction lines vary with increasing PA-P123 mole ratios; see Figure 3.3.

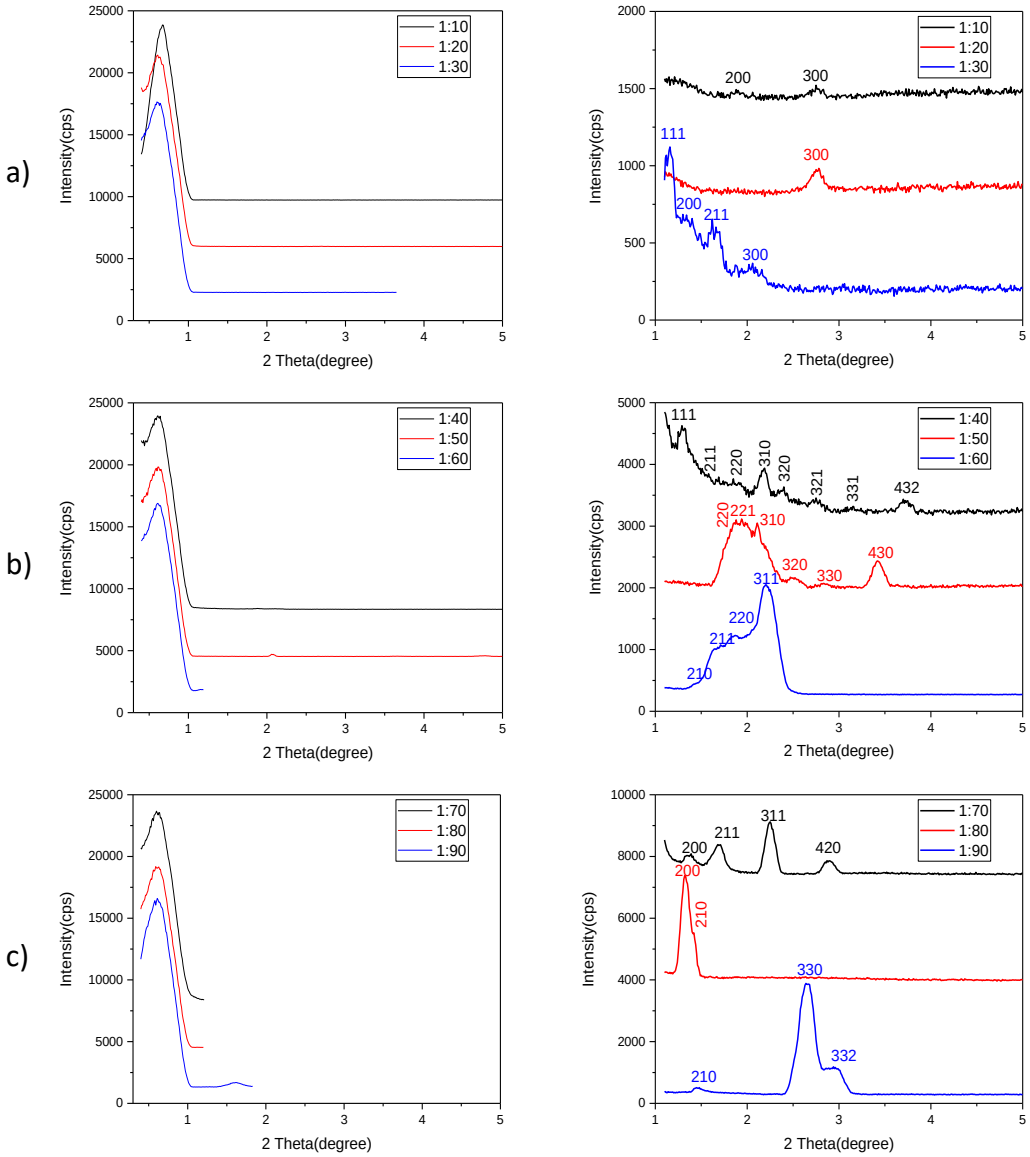

Figure 3.3. Small angle XRD patterns of the PA-P123 LLC phase with different PA/P123 mole ratios of a) 10, 20, and 30, b) 40, 50, and 60, and c) 70, 80, and 90.

The samples are abbreviated as PA-P123-XX, where the XX shows the mole ratio of PA to P123. The diffraction patterns of the PA-P123-10 and PA-P123-20 can be indexed to a 2D hexagonal structure. The XRD patterns of PA-P123-10 and PA-P123-20 displays lines from (200), (300) and (300) planes and the unit cell parameter **a** is 93.9 and 95.9 Å, respectively.

When the mole ratio in the PA-P123 sample is increased to 30, the structure changes from 2D hexagonal to a cubic mesostructure. The PA-P123-30 displays more diffraction lines in its XRD pattern. The structure is more ordered than the previous

mole ratios. The diffraction pattern displays lines at a d-spacing values of 76.1, 66.4, 54.5 and 43.1 Å, that can be indexed to (111), (200), (211) and (300) planes, respectively, of the cubic phase with a unit cell parameter **a** of 131.8 Å. Upon this phase change, the size of unit cell is increased drastically from around 95 to 132 Å, indicating a centered cubic system. Since the unit cell dimension is increased proportionally to the unit cell parameter of the hexagonal phase ($(2)^{1/2}$ a = 134 Å), the micelle domain size does not alter much as expected going from hexagonal to cubic structure.

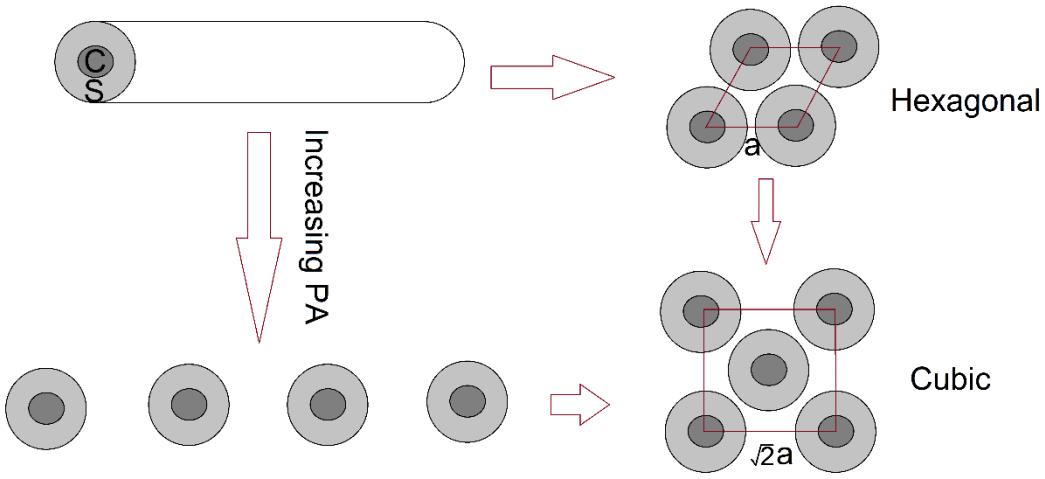

Figure 3.4. Schematic representation of the hexagonal to cubic transformation. (C = core, PPO units, and S = shell, PEO units)

In the PA-P123-40, the LLC mesophase preserves the cubic mesostructure that display 8 diffraction lines. This is quite unusual in LLC phases. These lines have d-spacing values of 68.4, 52.9, 47.7, 40.5, 36.8, 32.1, 28.2, and 23.9 Å and can be indexed to the (111), (211), (220), (310), (320), (321), (331), and (432) planes, respectively, with a unit cell parameter **a** of 128.0 Å, which is almost the same as the PA-P123-30.

When the mole ratio of PA is increased to 50 and 60, the diffraction patterns display broader lines, originated from overlapping of many diffraction lines. The patterns are indexed to (220), (221), (310), (320), (330), and (430) planes in the PA-P123-50 and

(210), (211), (220) and (311) planes in the PA-P123-60. The unit cell parameters, **a**, are 130.9 and 134.9 Å, respectively. The unit cell parameters show that increasing of the inorganic ingredients does not alter the unit cells, maybe indicating the formation of the same cubic mesostructure in all samples.

The XRD pattern of the PA-P123-70 shows that it also has a quite ordered cubic mesostructure. The diffraction lines, observed at 64.9, 52.2, 39.2 and 30.6 Å d-spacing values see Figure 3.3 (c), can be indexed to (200), (211), (311) and (420) planes, respectively, and provides a unit cell parameter **a** of 136.6 Å.

The PA-P123-80 is less ordered. However, there are still 2 diffraction lines in the XRD pattern of PA-P123-80 with a d-spacing values of 66.9 and 62.2 Å and can be indexed to (200) and (210) planes, see Figure 3.3 (c) with a unit cell parameter **a** of 139.0 Å.

When the mole ratio of PA reaches to the highest value, which is 90, the cubic structure is still well-ordered and display diffraction lines, originating from the (210), (330) and (332) planes of the cubic phase. The unit cell parameter **a** reaches to a maximum, 141.3 Å. In the cubic system, it seems like the unit cell is gradually increasing from 128 to 141 Å with increasing the PA/P123 mole ratio. There is a gradual increase by almost 2 Å in the unit cell for every 10 PA/P123 in the cubic mesophases. Since the surfactant domains (micelles) are all spherical in the cubic mesophase, this increase is likely due to a change in the number of P123 in the micelle units, otherwise the increase in the unit cell must be much larger if we only consider the density of PA; the space required for such amount of PA will be orders of magnitude larger to pack the extra PA like in its liquid phase in the LLC phase. Therefore, this data shows a decrease in the aggregation number (number of P123 molecule per unit micelle) of P123 in the micelle domains of the LLC mesophases. Increasing PA/P123 mole ratio in the PA-P123 mesophases increases the number of unit hydrophilic domains in the LLC phase to accommodate the extra PA in the expense of P123 packing/aggregation number. If we assume the unit cell dimension change is ignored (it is small), then the aggregation number will drop to half going from 40 to 90 PA/P123 in the LLC phase.

Note also that there is another diffraction line in each XRD pattern below 1°, where the measurement is more difficult. These diffractions are recorded by using a cupper block in front of the detector in order to protect the detector from the direct x-ray beam (Figure 3.3 - left side).

We also employed polarized optical microscopy (POM) technique to distinguish mesophase as anisotropic and isotropic to elucidate the structure of the mesophases. The POM images of PA-P123-10 and PA-P123-20 display focal conic fan texture, characteristic for the 2D hexagonal mesophase (Figure 3.5 - a, b and c). Although it is clearly shown in the XRD pattern that there is an ordered/oriented structure in all ratios, the samples of PA-P123-30 and up to PA-P123-90 between the crossed polarizer are dark. Therefore, the structure is changing from hexagonal (anisotropic) to cubic phase (isotropic) which appears dark under POM.

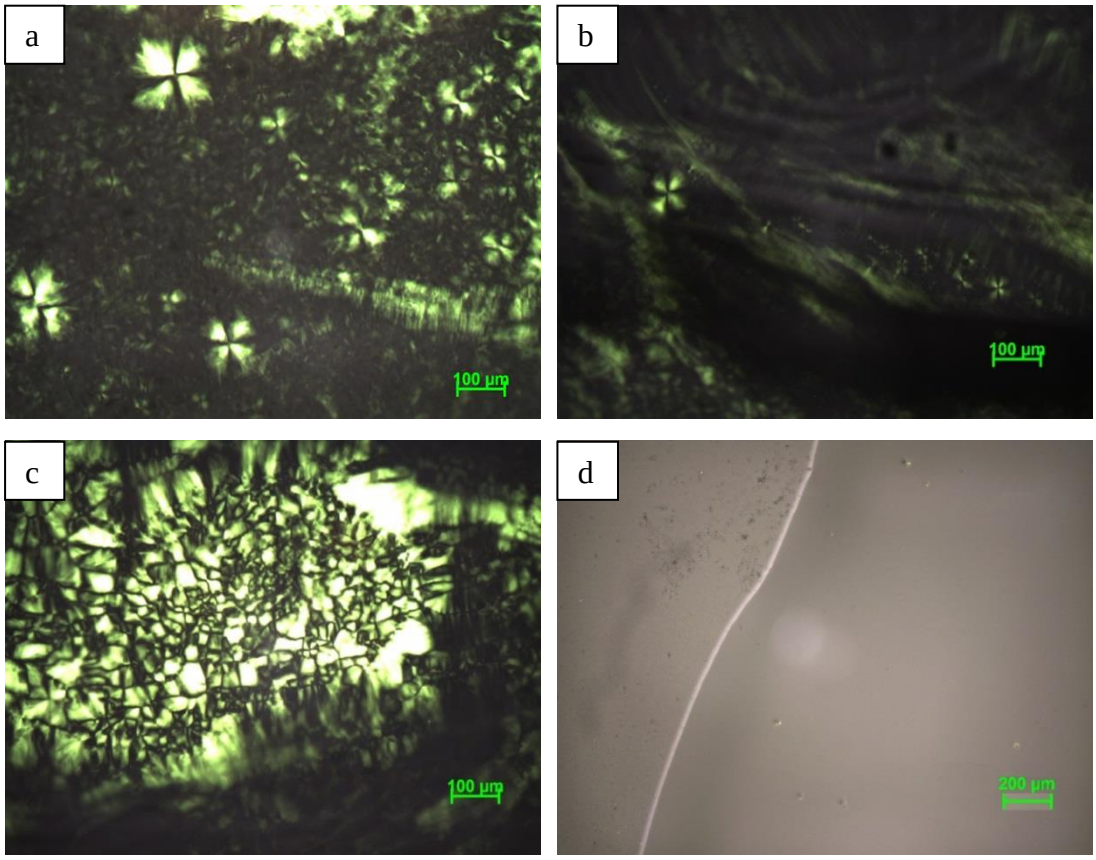

Figure 3.5. The POM images of PA-P123 systems with a PA/P123 mole ratio of a) 10, b) and c) 20, and d) 30.

The PA-P123 LLC phases were further investigated using ATR-FTIR spectroscopy. The ATR-FTIR spectra of the gels (PA-P123) display two main peaks at around 982 and 469 cm^{-1} due to the stretching and bending modes of PA species in the gel phase of PA-P123, respectively. The peaks at 1090 and 1006 cm^{-1}, observed in the PA-P123-10 gradually red-shifted to 1067 and 978 cm^{-1}, respectively, by increasing the mole ratio from 10 to 90. The peak at 934 cm^{-1}, observed in the PA-P123-10, disappears; whereas the peak at 883 cm^{-1} becomes visible while the mole ratio is increasing to 90. The peaks related to the surfactant (stretching modes of C-H bonds at around 2800-3000 cm^{-1}) are broadened when the acid concentration is increased, because the water coming from the PA increases concurrently or due to loosely packing of P123 in the micelle domains of the LLC mesophases. The broad features in the 2200-3500 cm^{-1} region are due to OH stretching of water, protonated water, and hydrogen bonded water-PA species. Broad bending mode of water at around 1600 cm^{-1} also shows the presence of various forms of water in the LLC media, see Figure 3.6.

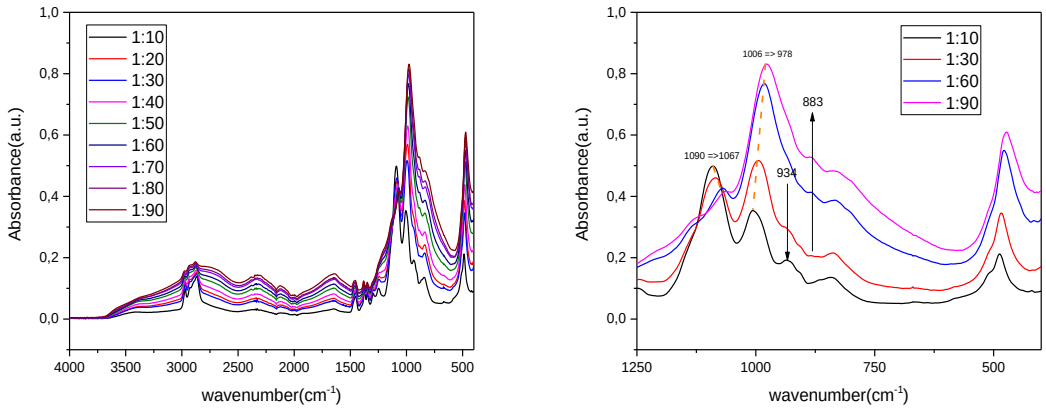

Figure 3.6. ATR-FTIR spectra of PA-P123 systems (from bottom to top, increasing PA/P123 mole ratio, from 10 to 90).

The solutions were also prepared by using extra 10 ml of deionized water and all the gradients of the gel and analyzed in the solution phase and also after gelation by using the same characterization techniques. The solutions were drop-cast coated over microscope slides and aged for sometimes (about 5-10 min) to remove the excess water from the samples so that the mesophases are formed. The samples coated over

the glass substrate were aged up to 10 days to observe the changes on the mesophases.

Time dependent changes were monitored for the mesophases by recording their small angle XRD patterns.

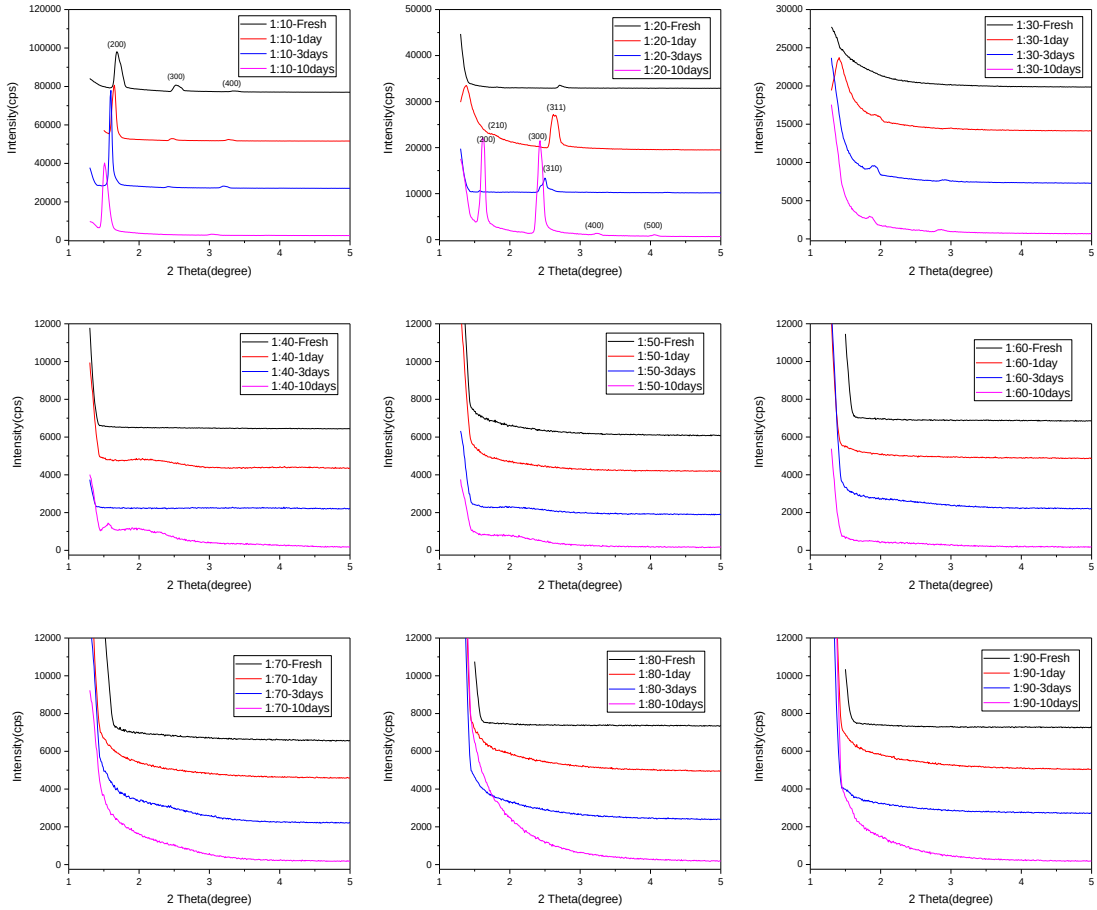

Figure 3.7. Time dependent small angle XRD patterns of the solutions of PA-P123 for all mole ratios.

Figure 3.7 (a) shows the XRD pattern of PA-P123-10 sample over time. The mesophase forms immediately upon coating the PA-P123-10 solution over a glass substrate; it is stable up to 10 days. There is a small shift in the d-spacing within 10 days of aging. Three diffraction lines are observed in the aged samples. The diffraction lines can be indexed to (200), (300) and (400) planes with d-spacing values of 55.1, 36.5 and 27.4 Å, respectively, of the hexagonal phase, where the unit cell parameter, **a**, is 109.5 Å.

In the PA-P123-20 sample, at the beginning of the gelation (due evaporation of excess water), the diffraction lines are very weak, but after 1 day, the diffraction lines start to appear. After 10 days of aging, the diffraction lines become more intense. The diffraction lines due to (200), (210), (300), (310), (311) (400) and (500) planes are observed at d-spacing values of 54.4, 48.8, 36.3, 34.0, 32.6, 27.2 and 21.8 Å, respectively. For this ratio, the hexagonal unit cell parameter, **a**, is 108.9 Å.

However, the diffraction lines become quite weak at higher PA/P123 mole ratios in comparison to the PA-P123-10 and PA-P123-20 samples. Even after 10 days of aging, they do not show any diffraction line in the small angle XRD patterns. There are just broad lines in the patterns of PA-P123-40 and PA-P123-50.

The solutions of PA-P123 coated on the microscope slide were also analyzed under POM and the fan textures are visible up to a 30 PA/P123 mole ratio. The POM images of PA-P123-10, PA-P123-20, and PA-P123-30 samples are similar, see Figure 3.8 (a). Above 30 mole ratio the images become dark, see Figure 3.8 (b). The dark image means that either there is no ordered mesophase in the structure (disordered) or the structure is cubic and disordered. Since no diffraction line is observed in the XRD patterns, we concluded that there is no ordered structure in the higher mole ratios if they are prepared from the solution phase. This is likely due to large amount of excess water that could not be removed by room temperature evaporation.

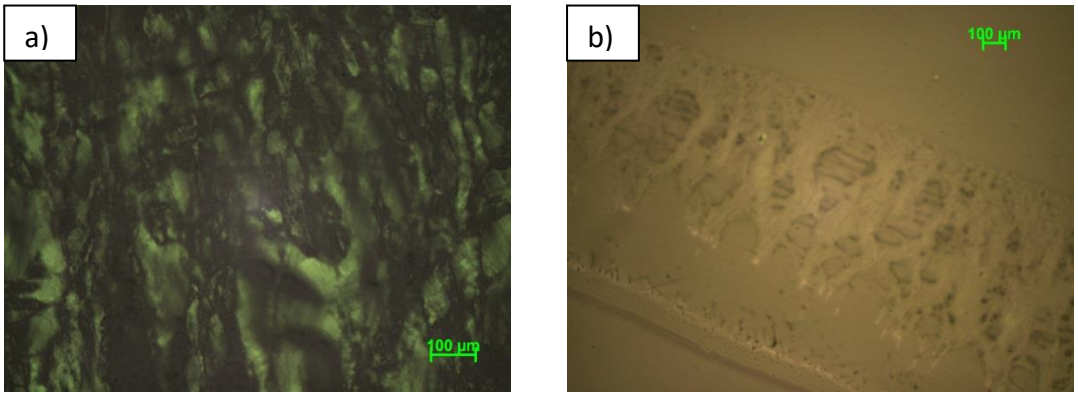

Figure 3.8. The POM images of a) PA-P123-20 and b) PA-P123-40.

Further, the solutions of the PA-P123 systems were examined by the ATR-FTIR spectroscopy. Since these samples hold lots of water, the water related peaks (stretching mode at around 3500-3200 cm^{-1} and bending mode at around 1600 cm^{-1}) dominate in the ATR spectra (Figure 3.9 (a)). The peak at around 3500-3200 cm^{-1} is quite broad, indicates that the water species are highly protonated and they are interacting with the surfactant species. Figure 3.9 (b) shows the ATR-FTIR spectra with increasing the PA/P123 mole ratio in the phosphate stretching region. There is definitely an increase in the peaks of 1173 and 1002 cm^{-1} without any shift with increasing PA/P123 mole ratio. The spectra do not show much of change except an increase of the intensity of the phosphate peaks, as expected. Note also that the spectra are quite different from that of the gel samples of the same PA/P123 ratios. It is clear from the comparison of these two sets of data that the excess water is difficult to remove from the solution phases to form the gels. Therefore, clearly remaining large amount of water in the samples influences the mesostructures as demonstrated by XRD measurements.

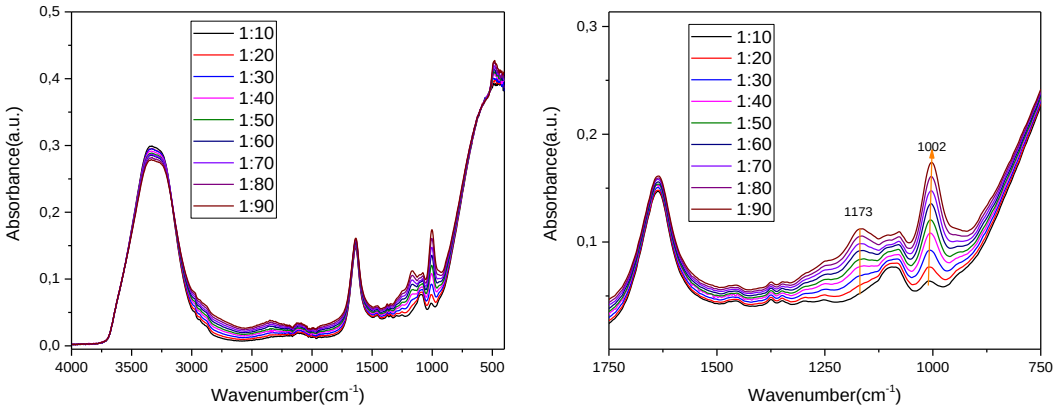

Figure 3.9. ATR-FTIR spectra of the solutions of PA-P123 systems.

3.2. Mesophases of Lithium Salt-Transition Metal Salt-P123

After the mesophases of PA/P123 systems were examined in detailed, the next step was the addition of the metal precursors to the PA-P123 LLC mesophases by keeping the mole ratios of the salts the same as PA (see Table 2.1 for the amounts) to produce stoichiometric $LiMPO_4$s (where M is Mn, Fe, Co, and Ni).

As shown in the solution preparation part in the experimental section, the solutions of Li(I)-Mn(II)-PA-P123 (decoded as S-LMnP) were prepared in two vials, where the acid and salts were initially separated to reduce the effect of high acid concentration. In the first vial (solution A), the salts were dissolved in 5 ml of water and then a half of the melted surfactant was added to this solution. In the second vial, (solution B), to a 5 ml water a required amount of PA was added to dilute the acid. Then, the other portion of the melted surfactant was added. Both solutions, A and B, were separately stirred for one night to obtain homogeneous solutions. After these solutions became clear, they were mixed with each other and stirred for another day. The reason, why the solutions were prepared using two different vials is because when the acid is added directly to the salts, it produces NO_2 gas, which is very toxic and some precipitation in the solution occurs. Therefore, diluted solutions were added to each other to prevent NO_2 release and precipitation of unknown bulk metal phosphate crystals.

After the solutions became clear and homogeneous, they were drop-cast coated on microscope slides (labeled as LMP-XX, where M is the transition metal ion and XX is the mole ratio of all ingredients to surfactant). The solutions, dropped over the glass substrates, were spread over the substrate to remove the excess water as quick as possible. Upon coating the solution, the glass slide was hold for about 1-2 min in a vertical position over a paper towel to decrease the amount of excess solution on the glass substrate to obtain a uniform film thickness.

Without aging the drop-cast coated samples, the small angle XRD patterns were recorded to characterize the LLC mesophase of the LMP mixtures. Figure 3.10 shows the small angle XRD patterns of LMnP, LCoP and LNiP in different mole ratios in the fresh forms.

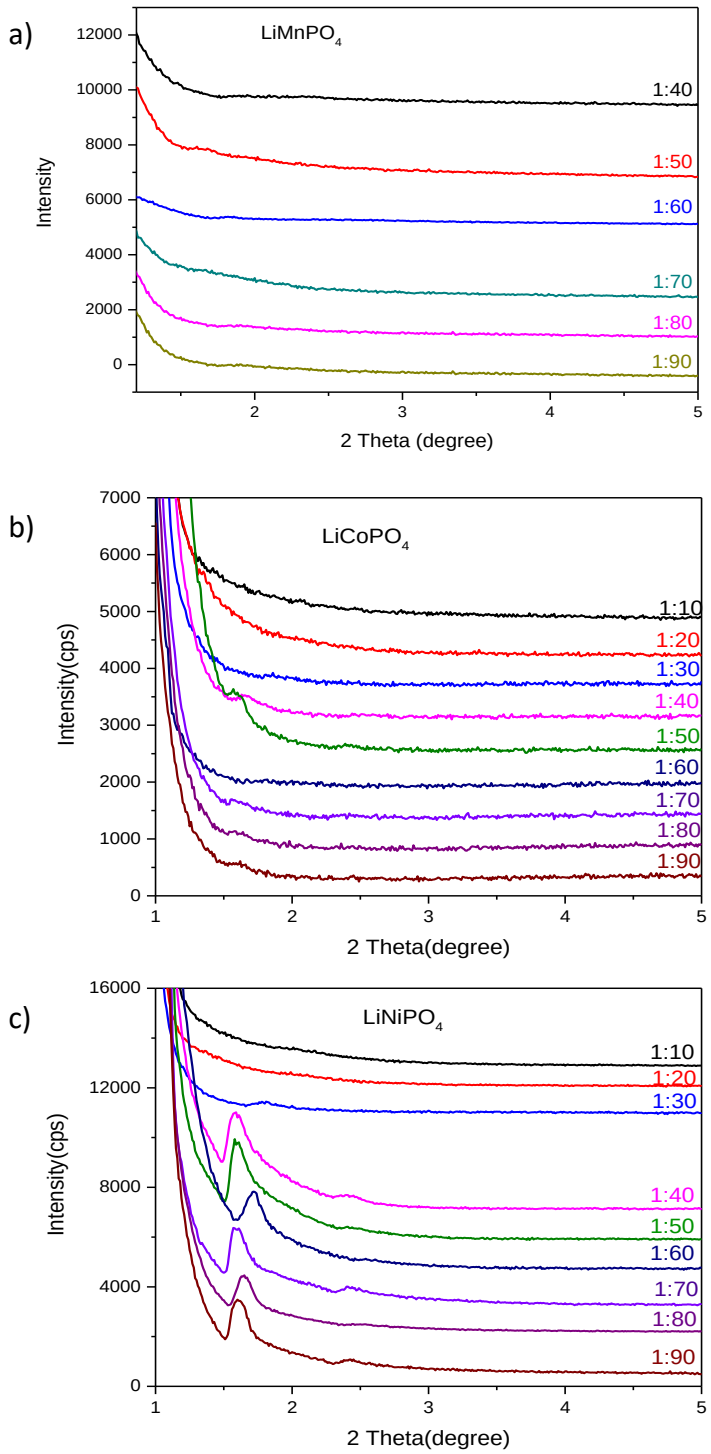

Figure 3.10. Small angle XRD patterns of a) LMnP, b) LCoP, and c) LNiP with different mole ratios.

Figure 3.10 (a) shows the XRD patterns of the LMnP. Notice that the diffraction lines are quite weak in all mole ratios. There is only one diffraction line in each pattern at around 1.60-1.90º, 2θ. The reason why the diffraction lines are very weak

is because the first diffraction (most probably (100) plane) line is below 1^{o} and could not be measured or the mesophase is quite disordered. However, in the LMnP-50, the diffraction line becomes visible, but it is still very broad and weak and difficult to index to any plane of a structure.

The diffraction lines are more obvious in the LCoP samples, compared to the LMnP samples. Up to 40 mole ratio, the diffraction lines are very broad and weak to identify the peaks but in the patterns of LCoP-40 and LCoP-50 samples, the diffraction lines are quite visible and located at 1.66 and 1.59^{o}, 2θ, respectively. In the XRD pattern of the LCoP-70 sample, two diffraction lines are observed at 1.60 and 2.40^{o} with d-spacing of 55.16 and 36.78 Å, respectively. The XRD patterns of the LCoP-80 and 90 samples display a line at 1.60^{o}, 2θ, same as 70 mole ratio, but the second diffraction lines are missing in these two ratios. Moreover, like the XRD lines of LMnP samples, the diffraction lines of the LCoP samples originate from the higher hkl planes, because the 0-1^{o} angle region is difficult to measure in the current set up of the diffractometer.

The diffraction patterns of the LNiP samples have more intense line(s), compared to the LMnP and LCoP samples. Up to 30 mole ratio, the diffraction patterns are similar to other LMPs, but above 30 Ni(II)/P123 mole ratio, all the LNiP samples strongly diffract x-rays in the small angles. There is a diffraction line at 1.80^{o}, 2θ, in the XRD pattern of the LNiP-30 with a d-spacing of 49.03 Å. When the mole ratio in the LNiP is increased to 40, two diffraction lines are observed at 1.60 and 2.40^{o}, 2θ, with d-spacing values of 55.16 and 36.78 Å, respectively. The size of the unit cell is increased from 98 to 110 Å with increasing the inorganic ingredients (salts and PA) from 30 mole ratio to higher mole ratios. The diffraction lines are almost at the same position from LNiP-40 to LNiP-90 compositions with a little shift, also indicating the aggregation number decrease with increasing the inorganic ingredient amounts in the LLC phases.

3.3. Synthesis of Mesoporous Lithium Manganese Phosphate

As mentioned in the experimental section, while preparing the solution of Mn(II) samples, some precipitation occurred upon mixing solutions A and B. Therefore, before further use of these solutions, they were centrifuged at 6000 rpm for 10 min to remove all the precipitates to obtain clear S-LMnPs, see Figure 3.11.

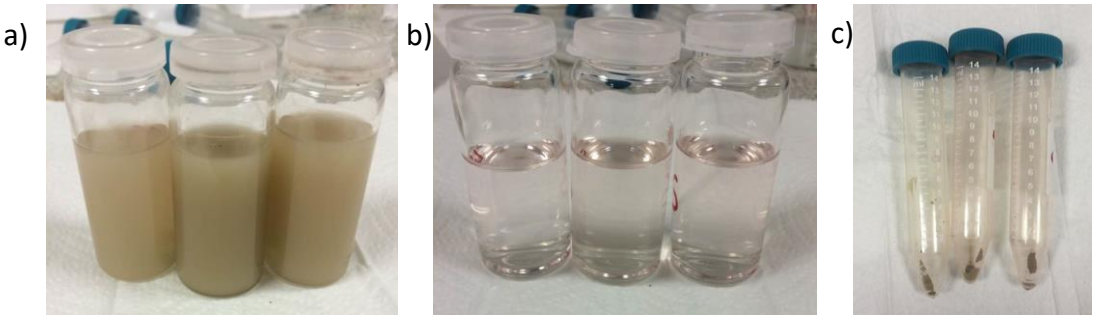

Figure 3.11. Solution forms of LMnP: a) before centrifugation, b) after centrifugation, and c) precipitates of LMnP solutions.

As shown in Figure 3.11 (a), the initial S-LMnPs are quite cloudy. However, after centrifugation (Figure3.11 (b)), they become clear solutions. Notice also that the amount of precipitate is very small, see Figure 3.11 (c); therefore, the clear solutions will still have similar composition of the initial solutions. Further steps were carried using the clear parts of the solutions. The precipitates were further characterized.

As mentioned before, there were some precipitations in the vials in the initial mixing step of preparation of LMnP. These particles were collected by centrifugation at 6000 rpm for 10 min and analyzed by using XRD technique The XRD patterns were collected to identify is the precipitates. However, the pattern of the precipitate does not be matched with any possible product reference data. In Figure 3.12, it is shown that the pattern does not belong to olivine $LiMnPO_4$ phase. They must be some manganese phosphate crystals. Since the precipitation is around 1-2 % regarding to all salts of the initial solution, these particles were just discarded and the remaining clear solutions were used for the synthesis.

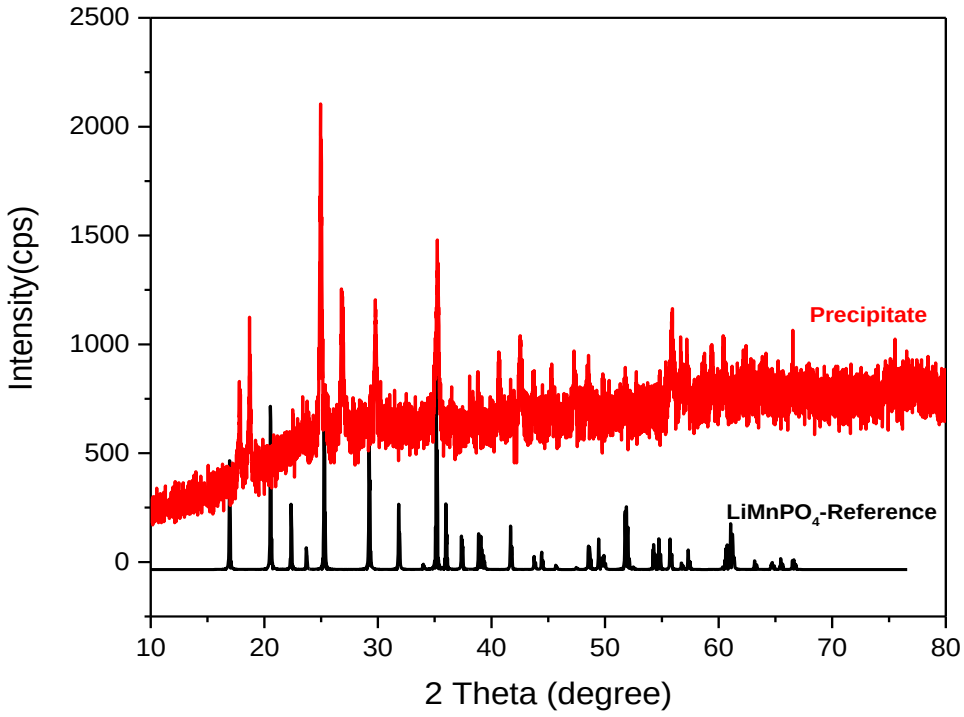

Figure 3.12. High angle XRD pattern of the precipitate from the initial LMnP solution.

The precipitates were also further analyzed by SEM imaging to evaluate the morphological structure of the particles. As shown in Figure 3.13, they are large crystals without having any pores. Therefore, they are not further characterized.

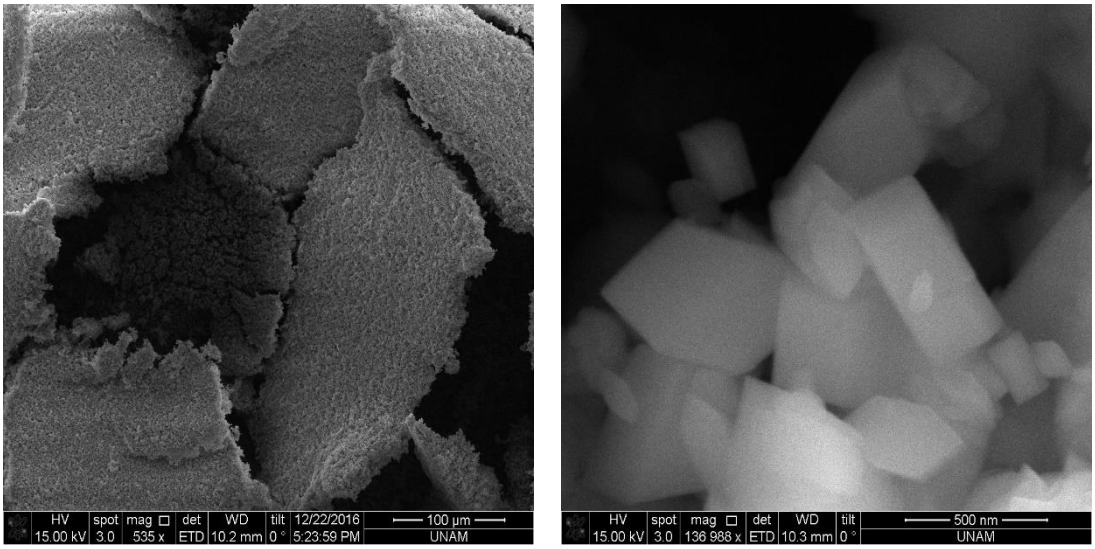

Figure 3.13. SEM images of the precipitate of LMnP solutions.

After the precipitates of S-LMnPs were decanted by centrifugation, the clear S-LMnP was obtained and the further synthesis and characterization of LMnPs were continued by that clear part.

Before the calcination process, the properties of the drop-cast coated S-LMnP were investigated by using FTIR spectroscopy after the gelation. In the spectra (Figure 3.14), not surprisingly, there are broad O-H stretching at the 3500-3400 cm^{-1} region and bending mode at around 1600 cm^{-1} due to presence of water in the samples. The surfactant peaks are observed at around 3000-2800 cm^{-1} region from the C-H stretching modes and the phosphate peaks are located at the 1100 and 551 cm^{-1} for its stretching and bending modes, respectively. Moreover, there is a sharp peak at 1384 cm^{-1}, which is due to asymmetric stretching mode of the NO_3^- ion. Since the spectrum was collected using the KBr pallets of the samples, the Br^- ion of KBr and NO_3^- ion of the mesophase undergo ion exchange reaction to form KNO_3 crystals that has a very sharp peak in the FTIR spectrum at around 1380 cm^{-1} [86].

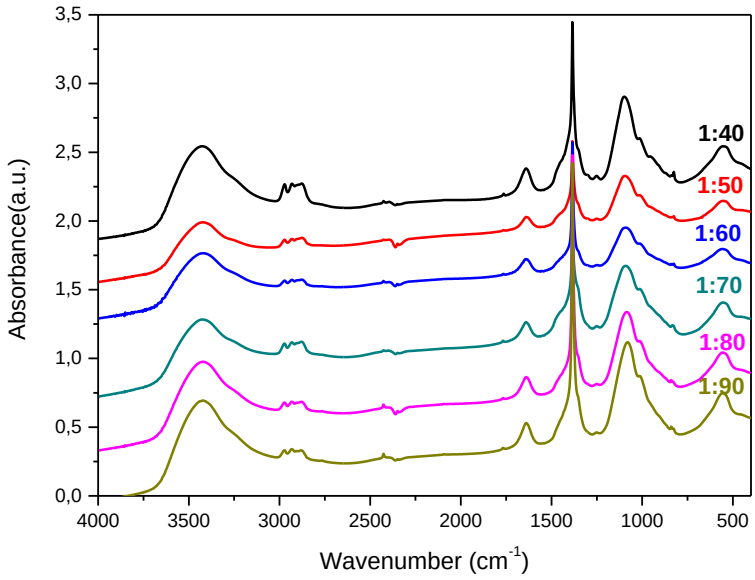

Figure 3.14. FTIR spectra of mesophases of LMnP-XX (XX values are given in the spectra) at room temperature.

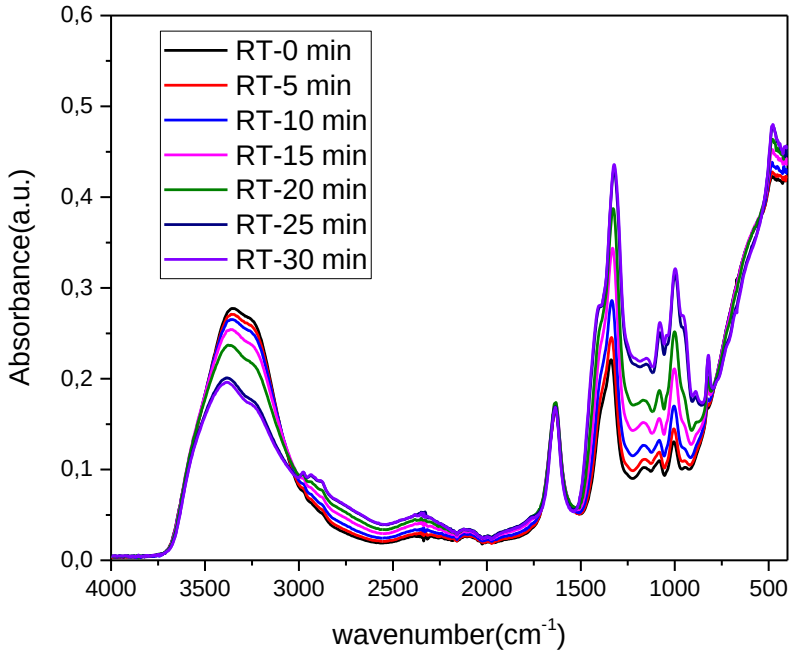

Figure 3.15. Time dependent ATR-FTIR spectra of LMnP-90 at room temperature.

To determine the stability of the LMnP samples, the 90 ratio was monitored using ATR-FTIR spectrometer till the spectrum does not change. One droplet of LMnP-90 solution was placed on the ATR-FTIR diamond and the spectra were collected with 5 min intervals during aging, see Figure 3.15. It is demonstrated that up to 25 minutes, the water in the sample evaporates, after that point there is no change in the O-H stretching region.

SEM images of these samples were collected to have an idea about how the structure of the samples looks like before the calcination step. Figure 3.16 shows the SEM image of the LMnP-90 sample. Surprisingly, the image shows that the samples are already uniform spherical solid particles with a typical particle size of around 300 nm. Figure 3.16 (a) shows the zoomed area of the sample, all particles show porous like features due to contrast difference between the surfactant and LMP solid domains in the SEM images. Figure 3.16 (b) shows a more general image of the sample, which has uniform spherical particles. The SEM images show that the mesophases of LMPs are not stable and they undergo transformation to mesotructured soft solids.

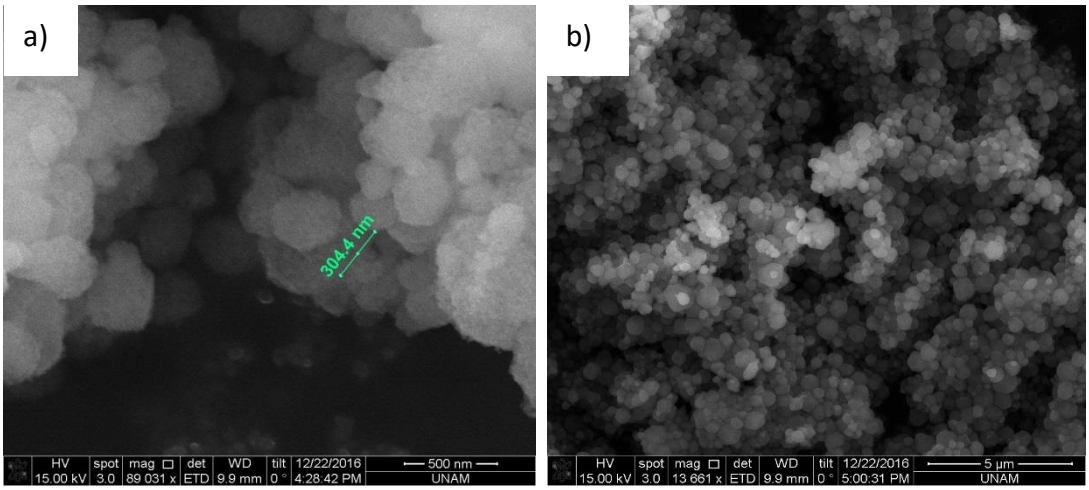

Figure 3.16. SEM images of LMnP-90 at room temperature.

Since there is no detailed information about the LMnP particles in the small angle XRD patterns and FTIR spectra, these samples were further characterized after calcination process. Firstly, the clear parts of solutions were spread on the glass substrate. Then, they were calcined at different temperatures by using pre-heated ovens to obtain our target mesoporous materials. The calcination process was carried at as low as 300 ^{o}C for 1 hour. All the samples calcined at 300 ^{o}C are amorphous; as shown in Figure 3.17, there is no diffraction line in the XRD patterns. There is only one broad feature originated from the glass substrate and amorphous sample.

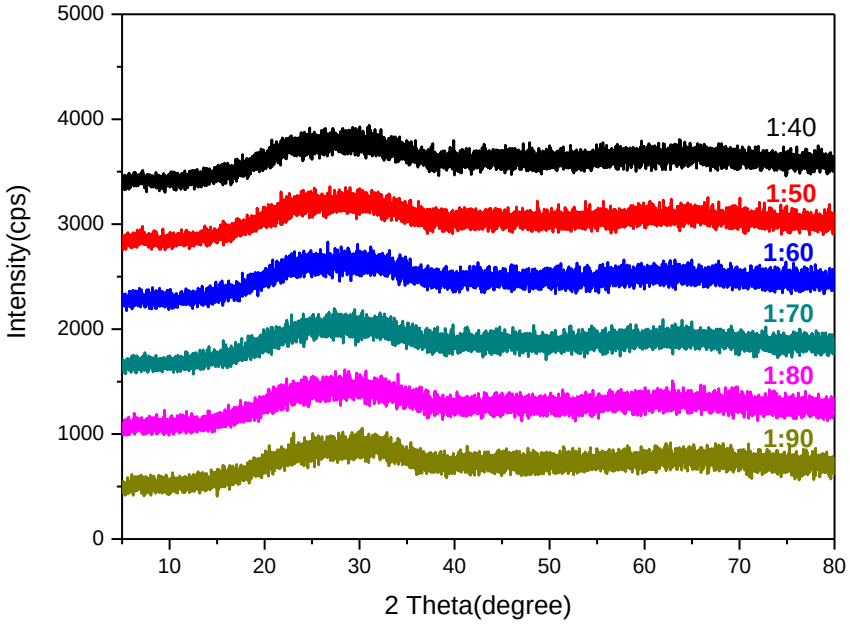

Figure 3.17. High angle XRD patterns of LMnP for different mole ratios at 300 ^{o}C for 1 hour.

Moreover, the FTIR spectra were collected from the calcined LMnP (calcined at 300 ^{o}C) powders, see Figure 3.18. The spectra shows that when the mole ratio is increased from 40 to 90, the O-H stretching peak intensity increases, indicating that the materials are holding more water inside particles due to maybe larger surface area or higher porosity. Even though they are calcined samples, a small peak at around 1350 cm^{-1} due to nitrate stretching remains in the spectra. The major peaks are the stretching and bending modes of phosphate at 1053 and 576 cm^{-1}, respectively. They appear as broad peaks due to amorphous nature of the materials at 300 ^{o}C, so all modes of P-O stretching overlap with each other to give one broad peak.

The phosphate stretching peak red-shifts from 1100 to 1053 cm^{-1} upon transformation from the mesophase (at RT) to mesoporous of LMnP (at 300 ^{o}C) and a blue-shift is observed from 551 to 576 cm^{-1} in the phosphate bending mode (compare Figures 3.14 and 3.18).

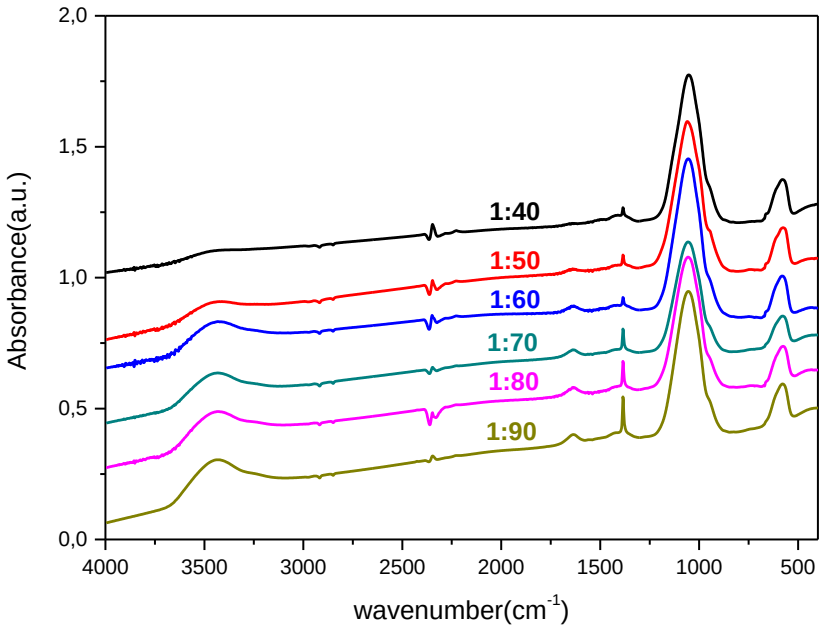

Figure 3.18. FTIR Spectra of the LMnPs with different mole ratios at 300^{o}C.

In order to determine if the samples are the targeted materials, $LiMPO_4$, these samples were further annealing at higher temperatures to obtain their crystalline phases. Therefore, the samples were gradually annealed by increasing the annealing temperature from 300 to 400 ^{o}C (with an increment of 50 ^{o}C) to determine the

crystallization temperatures. Crystallization of LMnP initiates at around 400 °C, at which the crystals diffract x-ray and the diffraction patterns match with the reference olivine phase of $LiMnPO_4$ (reference data is taken from ICDD PDF cards, PDF-card no 00-033-0804 for $LiMnPO_4$, see Figure 3.19).

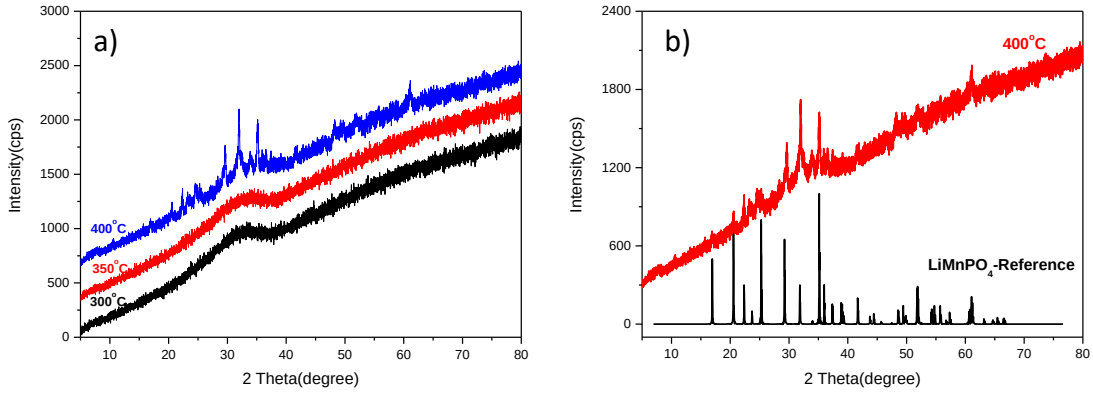

Figure 3.19. High angle XRD patterns of LMnP-90 a) at 300, 350, and 400 °C and b) at 400 °C and $LiMnPO_4$ reference PDF-card no 00-033-0804.

The TEM images of the samples calcined at different temperature were also collected for further characterization. As shown in Figure 3.20, at 300 °C the LMnP-90 has perfect spherical shape and good mesoporous network. When the temperature is increased to 400 °C, the pores start collapsing and enlarging. Moreover, at 400 °C, since it is a crystalline material, as evidenced from the XRD data; the crystalline lattice fringes are observed at the pore-walls of the material (see Figure 3.20 (right)).

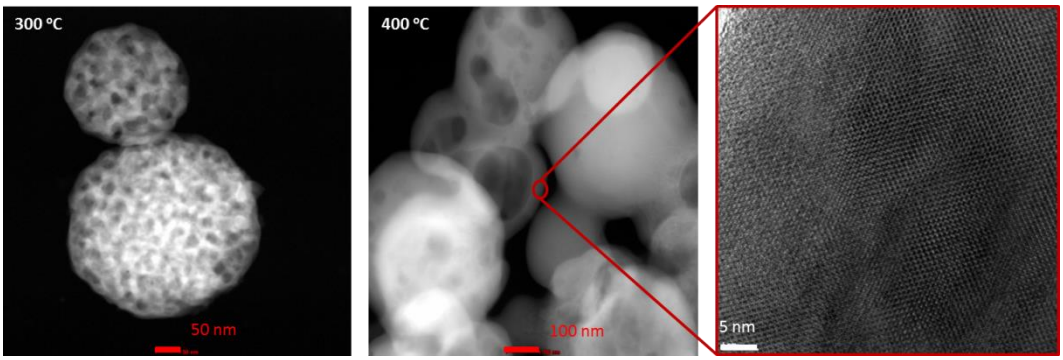

Figure 3.20. TEM images of LMnP-90 at 300°C (left), 400°C (middle) and zoomed 400°C (right).

N_2 adsorption-desorption isotherms were also collected to evaluate the surface area, pore size, and pore volume to show how they change with increasing calcination temperature. The results correlate with the TEM observation; the surface area is significantly reduced with increasing the annealing temperature. The Brunauer–Emmett–Teller (BET) surface area is 40 m^2/g at 300 ^oC, t, it decreases to 30 m^2/g at 350^oC and when it becomes crystalline (400 ^oC) it drops drastically to 9 m^2/g (see Table 3.1). This data also show that the pores merge into each other and become larger, resulting in diminishing the surface area of the material with increasing temperature.

Sample	BET Surface Area (m^2/g)
300 °C	40
350 °C	30
400 °C	9

Table 3.1. The BET surface areas of LMnP-90 at different temperatures.

The temperature effect on the LMnP-90 was further examined using FTIR spectroscopy. FTIR spectra display some changes with increasing annealing temperature. The most drastic change occurs in the phosphate region. Since the high temperatures cause crystallization, the peaks of P-O stretching and bending modes become sharper and well resolved. As shown in Figure 3.21, up to 400 ^oC the peaks are broad and there are only two broad peaks due to the phosphate stretching and bending modes. At 400 ^oC, 3 different peaks appear from the broad peak at around 1052 cm^{-1} and become well resolves at 500 ^oC; the peak at 1052 cm^{-1} splits into 3 different peaks, located at 1065, 995, and 942 cm^{-1} for the stretching modes, whereas the peak at 576 cm^{-1} also splits into 4 different peaks, observed at 618, 590, 575, and 561 cm^{-1}. These characteristic features are also observed in the crystalline olivine phase of LMnP. [87] Therefore, the FTIR spectra are showing the amorphous to crystalline transformation of the olivine phase of LMnP.

Also, the NO_3^- peak at 1384 cm^{-1} disappears, when the temperature reaches to 350 ^oC which means after that temperature, nitrates completely decompose and are removed from the samples, as likely nitric oxides.

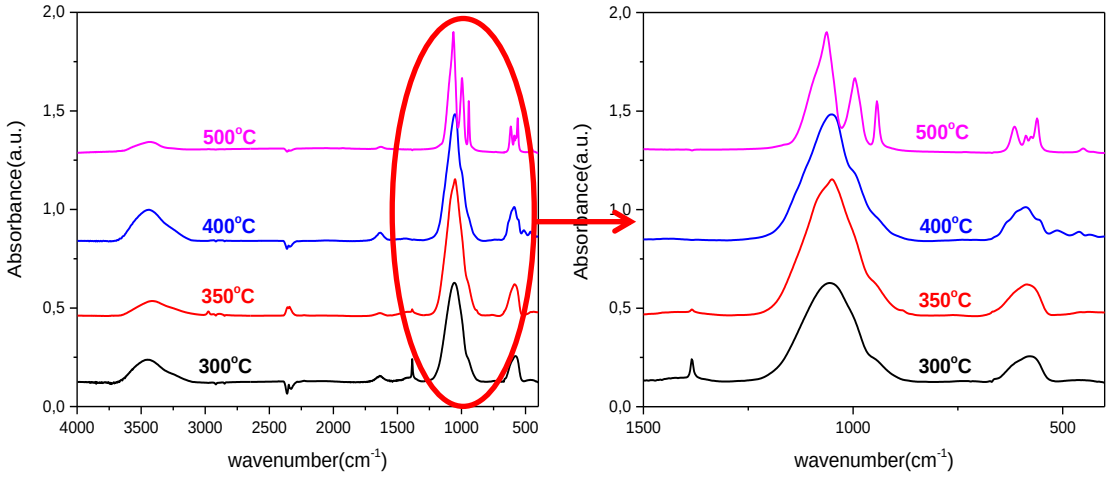

Figure 3.21. FTIR spectra of LMnP-90 at various temperatures.

The morphologies of LMnP samples (calcined at 300 ^oC), obtained from different mole ratios, were also investigated by collecting their SEM images. Figure 3.22 (a) demonstrates that the particles of LMnP-10 are quite small and about 30-50 nm spherical particles. When the mole ratio is increased to 40, the particles are in100-200 nm range. Moreover, the morphology also changes from spherical to shapeless particles. With further increasing the ingredient concentration in the mesophase the spherical particles reform. Nevertheless, the uniformity of the particle sizes cannot be preserved. Size of the particles is in the range of 50-500 nm.

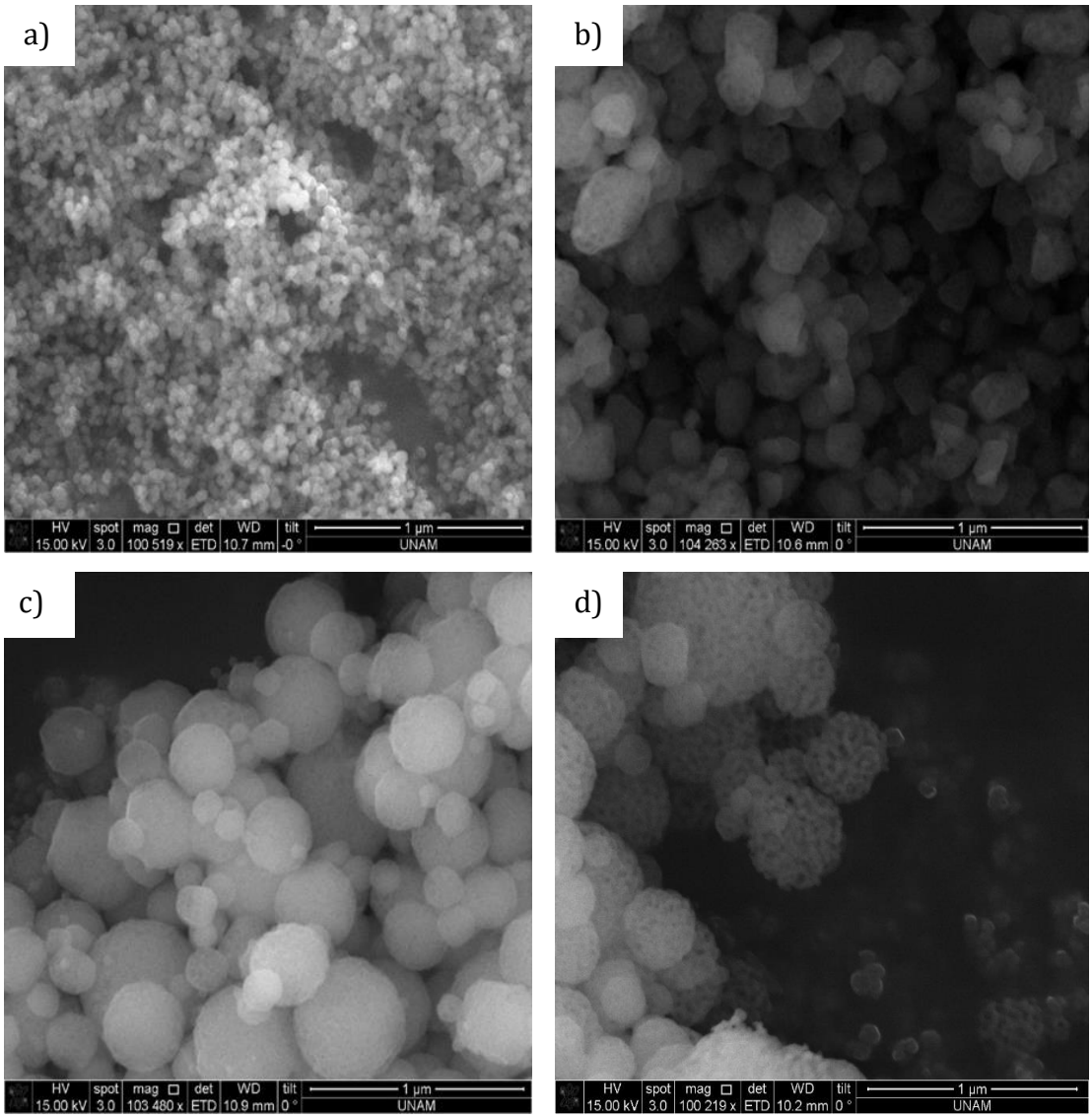

Figure 3.22. SEM images of a) LMnP-10, b) LMnP-40, c) LMnP-70, and d) LMnP-90 at 300 ºC.

The 60 mole ratio was chosen for further characterization of the LMnPs. The high angle XRD patterns of the samples, calcined at 300 and 500 ºC, were recorded using a more powerful diffractrometer. As expected, at 300 ºC the material is amorphous and at 500ºC the material completely crystalline. The diffraction lines of LMnP-60 perfectly match with the olivine phase of $LiMnPO_4$ reference data, see Figure 3.23.

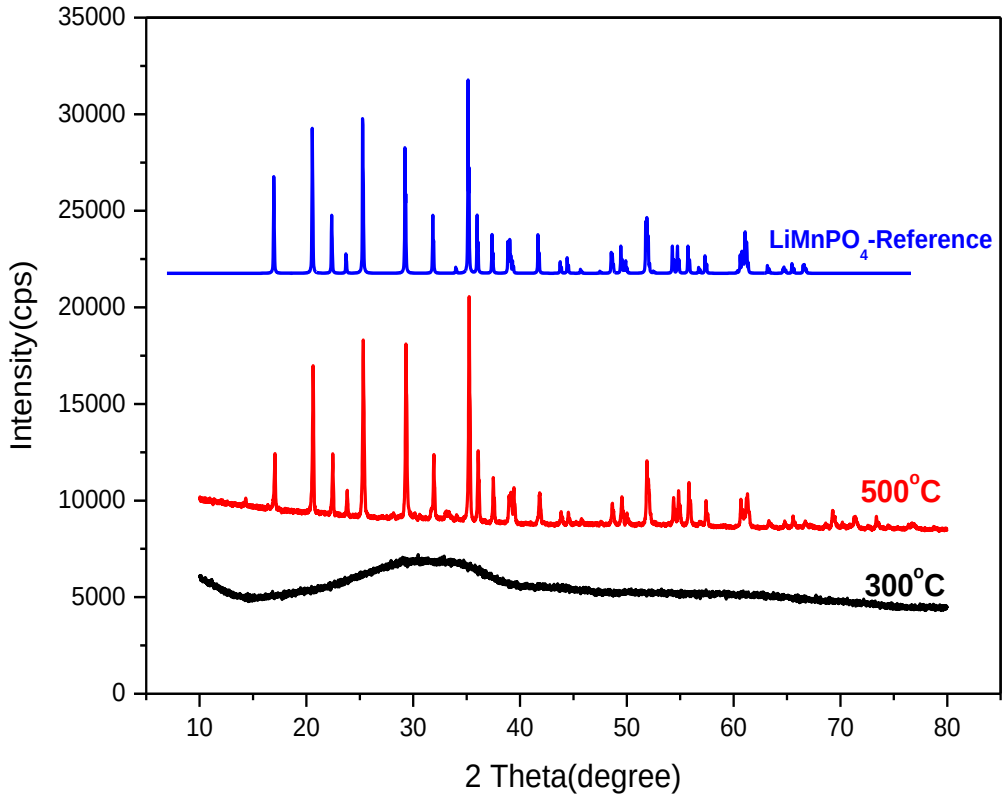

Figure 3.23. High angle XRD patterns of LMnP-60 at 300 and 500 °C with the reference data (PDF-card no 00-033-0804).

The mesoporosity in the LMnP-60 sample has been investigated by using SEM imaging for both amorphous and crystalline forms. Figure 3.24 shows porous features of the particles, calcined at 300 °C and aggregation in the samples, calcined at 500 °C. The particles are truncated spherical at 300 °C. As the calcination temperature is increased to 500 °C, the pores expand and the particles agglomerate to each other.

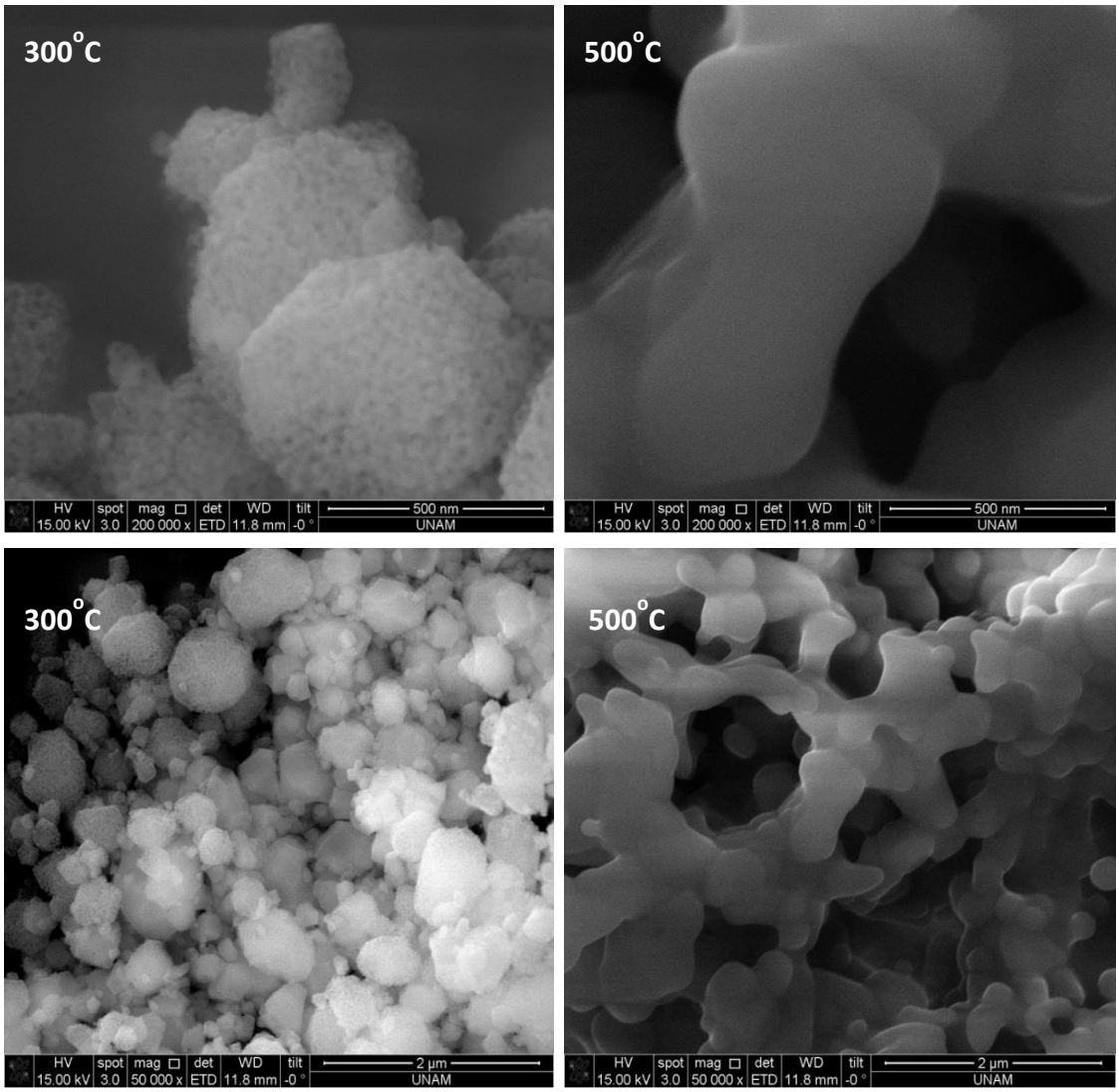

Figure 3.24. SEM images of the LMnP-60 sample calcined at 300 and 500 ºC (scale bars are 2 µm).

TEM images were also recorded to examine the pores more elaborately in the LMnP-60 samples, calcined at 300 ºC. From the images (Figure 3.25), it is clearly observed that the pores are well-structured and quite small. The image with 0.1 µm scales bar shows a few particles coming together and they all are mesoporous particles. The right image with the scale bar 20 nm focuses only one particle showing the pores more clearly. However, we observed that the particles are very sensitive to the electron beam (used in TEM imaging, 200 kV) and further focusing damages the pores of the particles, see Figure 3.25 (right).

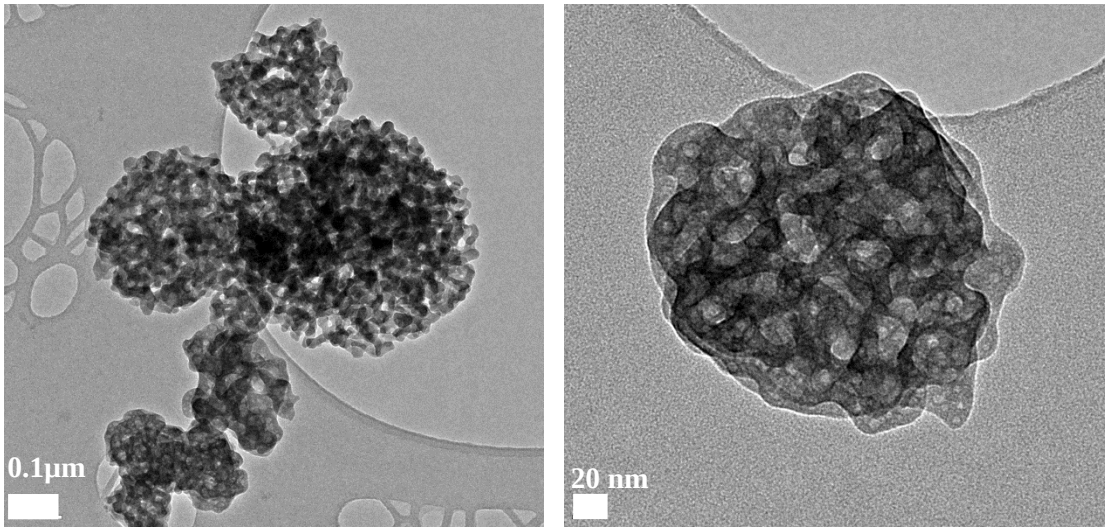

Figure 3.25. TEM images of the LMnP-60 at 300 ^{o}C at different magnifications.

The N_2 adsorption-desorption isotherms were collected. They display hysteresis due to channeled porous structure in the LMnP-60. In the linear isotherm plot, the adsorption-desorption of the N_2 gas on the surface of the sample is measured in terms of relative pressure of N_2 gas. The type of isotherm is H1 loop, which corresponds to a narrow range of uniform mesopores in the sample, calcined at 300 ^{o}C. [88] When the calcination temperature increases to 500 ^{o}C, the hysteresis of the type H1 is lost because the surface of the sample is reduced and the pores are two large to observe the hysteresis, see Figure 3.26 (a). Moreover, the pore size distribution plot of the LMnP-60 was calculated using Barrett-Joyner-Halenda (BJH) method. According to the BJH method (the pore volume versus pore width graph) the pore size is in the range of 20-30 nm for the samples calcined at 300 ^{o}C and it is in the mesoporous material category (IUPAC definition 2-50 nm). However, at a high temperature (such as 500 ^{o}C), the surface area diminishes and the pore size expands and become a flat surface, see Figure 3.26 (b).

The BET surface areas, BJH average pore sizes, and pore volumes values are depicted in Table 3.2. However, some small pores form during high temperature annealing, see Figure 3.26. This may be indicating the formation of larger pores by growing pore-wall; some new smaller pores are forming due to reorganization of the crystalline pore-walls. But in general majority of the pores disappear, indicating a collapse of the mesoporous structure at 500 ^{o}C.

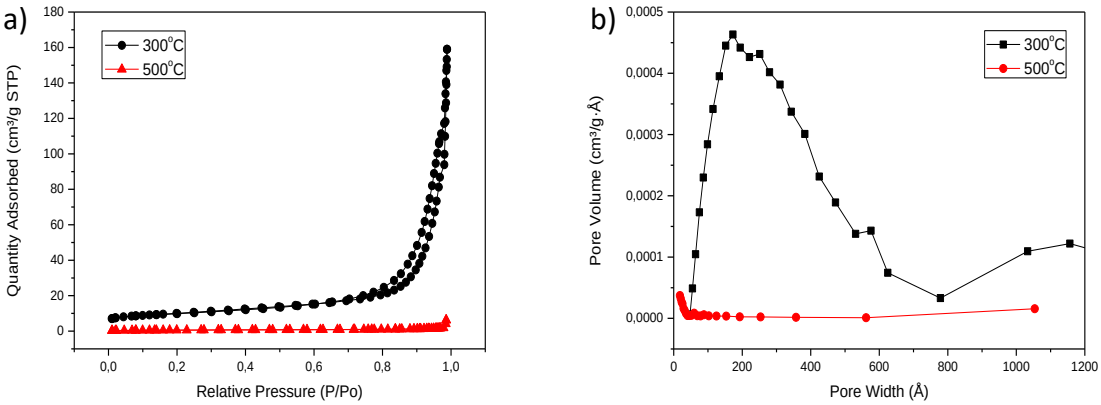

Figure 3.26. a) Linear isotherm plot and b) BJH pore size distribution plots of LMnP-60, calcined at 300 and 500 °C.

Sample (LMnP-60)	BET Surface Area (m^2/g)	BJH Pore Size (Å)	BJH Pore Volume (cm^3/g)
300°C	35	304	0.243
500°C	2	265	0.009

Table 3.2. The BET surface areas, BJH pore sizes, and pore volumes of LMnP-60 at 300 and 500 °C.

3.4. Synthesis of Mesoporous Lithium Cobalt Phosphate

The LMP synthesis system was further expanded to synthesize mesoporous lithium cobalt phosphate (LCoP). Cobalt nitrate salt was used in place of manganese to synthesize mesoporous LCoP. Differently from the LMnP solutions, there was no precipitation while preparing the solutions of LCoP. The solutions became clear after combining solutions A and B and remain stable for a long time. The synthesis part was also the same as the manganese system; the solutions were spread on the glass slides and characterized as it is or after calcination.

Firstly, the preformed mesophases from the LCoP-60 solutions were examined as addressed on section 3.2. Afterwards, the stability of the mesophase was pursued by ATR-FTIR spectroscopy measurements. One droplet of the LCoP-60 solution was put over the diamond of the spectrometer and the spectra was recorded every 5 min

to monitor the changes during aging. The aging process was aimed to determine the time required for the evaporation of water. Figure 3.27 shows the ATR-FTIR spectra of the LCoP-60 solutions over time. No further changes are observed after 20 min of aging by checking the 3500-3200 cm^{-1} range, which belongs to water, O-H stretching modes of various water and PA species.

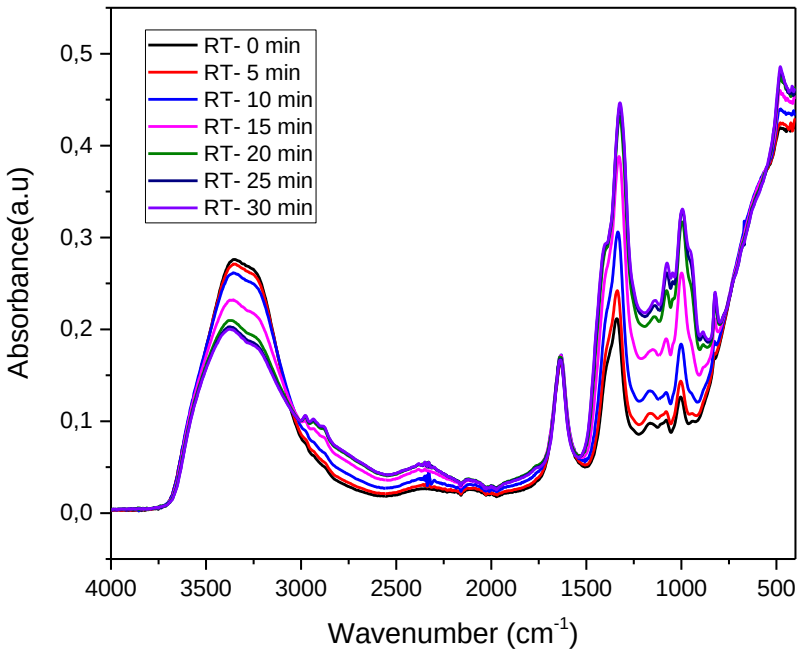

Figure 3.27. ATR-FTIR spectra of aging of the S-LCoP at room temperature.

SEM images of the aged samples (at RT) were collected to identify the shapes of the particles, see Figure 3.28. At low magnifications, the particles of the LCoP look like a film. However, when it is magnified, the films are made up of smaller particles. Moreover, with further magnification, they appear like they are mesoporous particles. However, these particles still have surfactant molecules in their structure; therefore, this contrast difference is resulting from the surfactant and LCoP species.

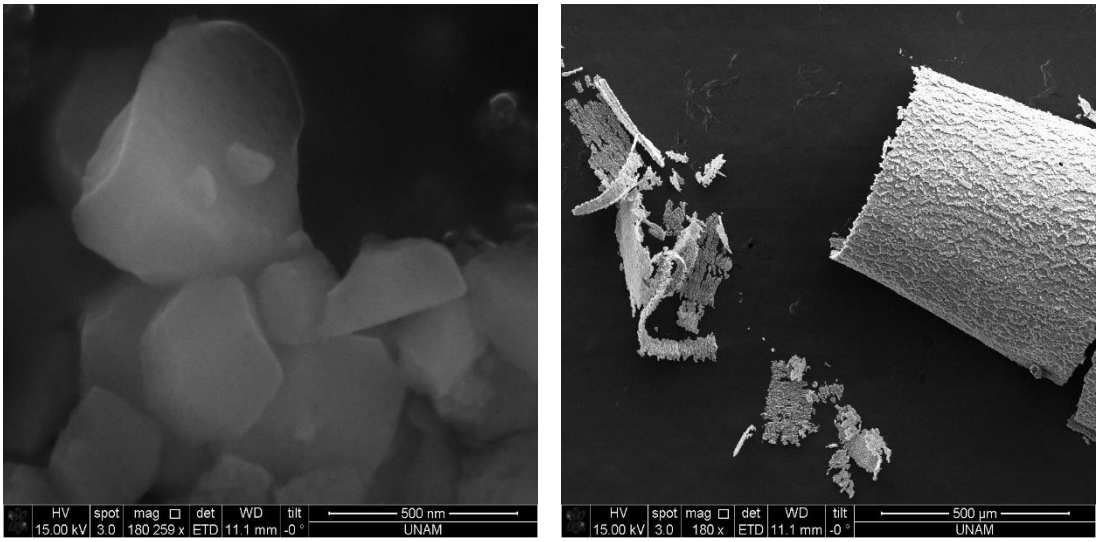

Figure 3.28. SEM images of LCoP-90 at room temperature.

These samples were also calcined at various temperatures to evacuate their pores. Since there was no precipitation in the solution phase, they were directly spread on the microscope slides and without aging they were put to pre-heated ovens for 1 hour for calcination. At 300 ^{o}C, the structure is mesoporous and amorphous. When the calcination temperature reaches to 500 ^{o}C, the structure becomes crystalline and pores are collapsed. Same as the manganese case, the crystallization starts at 400 ^{o}C but fully crystallize at 500 ^{o}C. Moreover, 60 mole ratio is also chosen as the best mole ratio for the LCoP sample. In Figure 3.29, a high angle XRD pattern of the LCoP-60 is shown with a $LiCoPO_4$ reference pattern and all the diffraction lines perfectly match with the reference data with a slightly different intensity patterns.

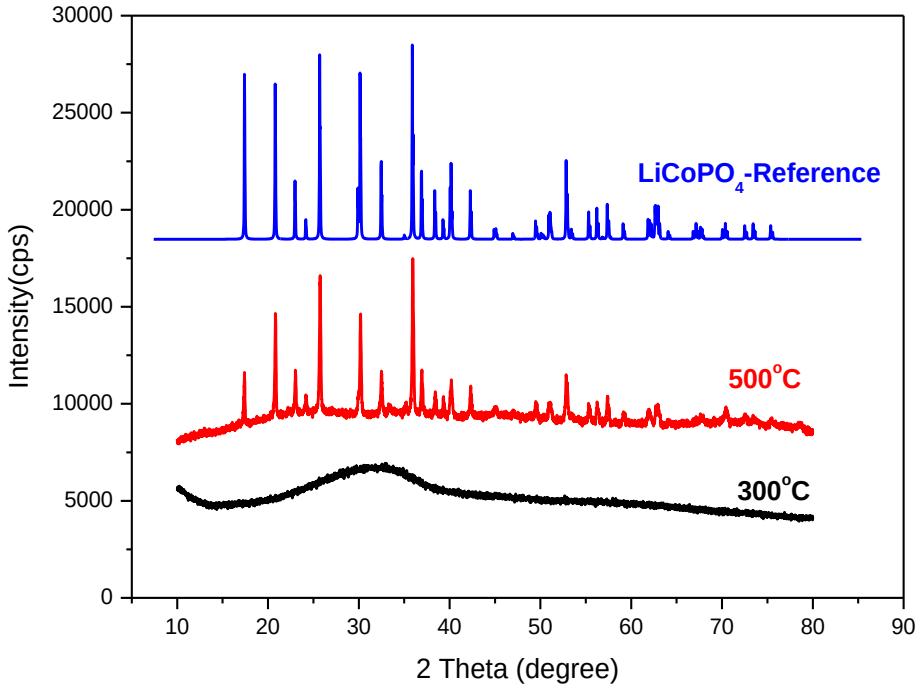

Figure 3.29. High angle XRD patterns of LCoP-60 and reference data of $LiCoPO_4$, the PDF-card no 00-032-0552.

Although the 60 mole ratio was chosen as the best composition, the SEM images of all mole ratios calcined at 300 ^oC were also recorded to identify if there is any morphological changes with the ingredient composition. Figure 3.30 shows the SEM images of all mole ratios from 10 to 90 and showing the formation of different size and shape particles. The LCoP-10 particles (see Figure 3.30 (a)) are very small and their shape is not perfect spherical. With increasing mole ratio, the size of the particles also increase and the shape is becoming perfect spherical. Up to LCoP-50 (Figure 3.30 (e)), the shape is not perfect spherical but in the LCoP-50 sample the shape of the material has both perfect spheres and some shapeless particles. The shape of the particles becomes perfect spheres in the LCoP-60, which is chosen as the best mole ratio, since the particle shape is uniform. However, with increasing mole ratio, the size of particles loses size uniformity. In the high mole ratios, the particle size varies from 100 nm to 1 µm.

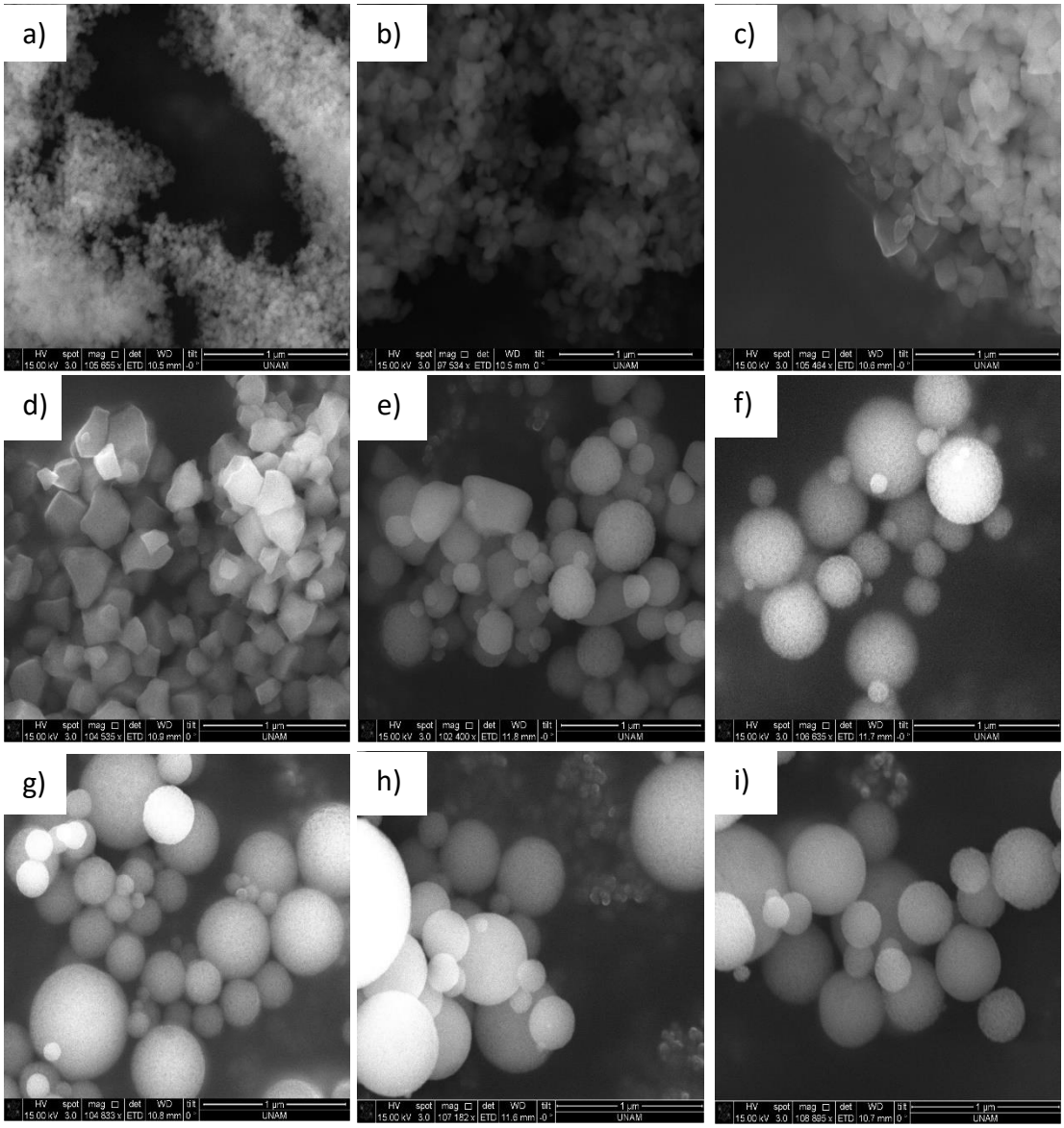

Figure 3.30. SEM images of LCoP- a) 10, b) 20, c) 30, d) 40, e) 50, f) 60, g) 70, h) 80, and i) 90 mole ratios at 300 ºC.

TEM images were collected to show the details of the structure in nanoscale, like porosity and crystallinity in the LCoP samples. All the images in Figure 3.31 were collected from the samples calcined at 300 ºC. Even in the low mole ratios, the material is porous with a pore size of 5-10 nm. The mesoporosity and shapes of the LCoP particles become more visible with increasing mole ratio in the initial solutions.

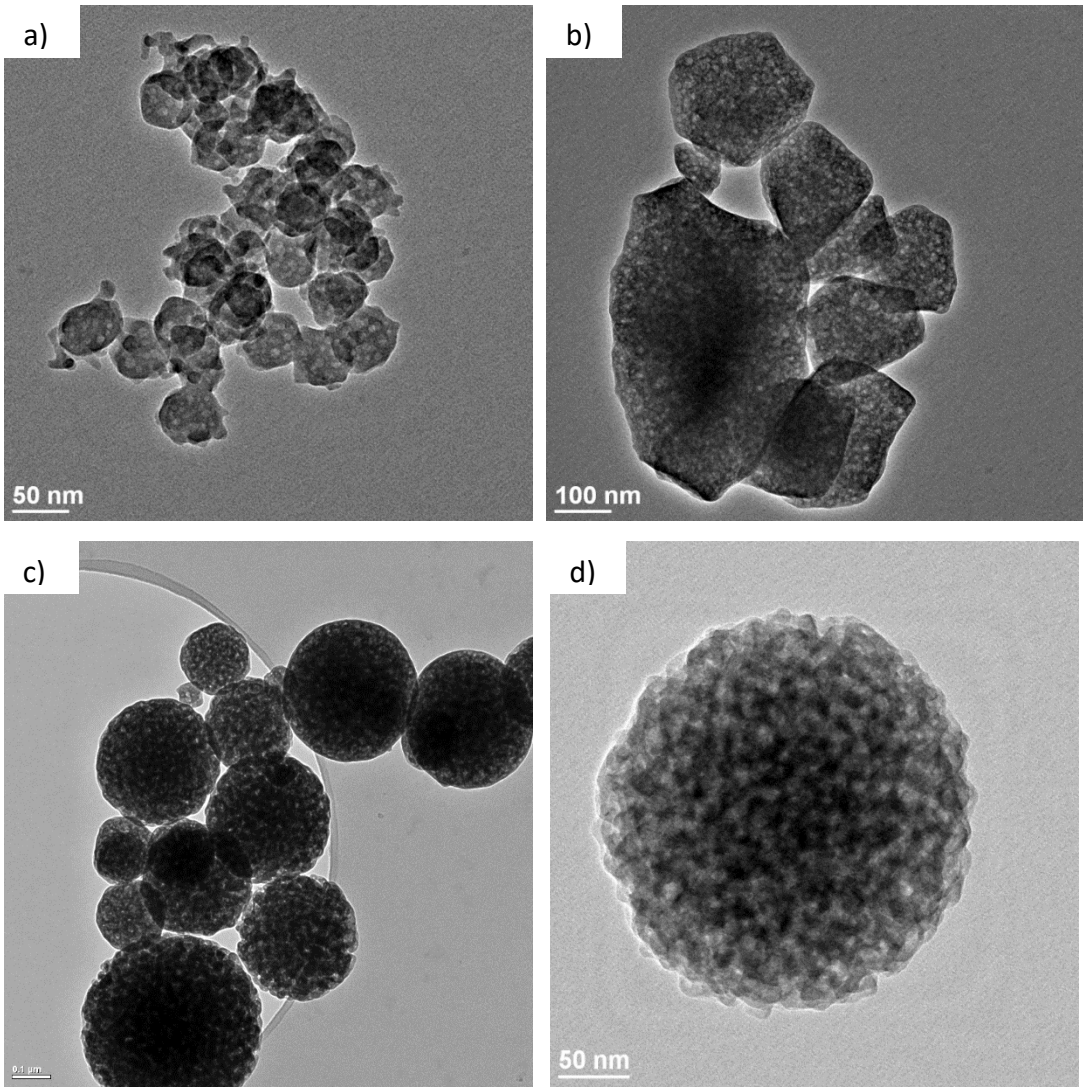

Figure 3.31. TEM images of LCoP- a) 10, b) 40, c) 60 and d) 90 mole ratios at 300 ºC.

The N_2 adsorption-desorption isotherms were recorded in order to evaluate the pore structure and surface related data in the LCoP-60 samples. At 300 ºC, similar to LMnP samples, the type of isotherm (H1 loop) displays a narrow range of uniform mesopores, which is lost when the annealing temperature reached to 500 ºC (see Figure 3.32 (a)). Moreover, the BJH method was used for the calculation of pore size distribution in the LCoP-60 particles. By inspecting the pore volume versus pore width graph (see Figure 3.32 (b)), it is clear that the pore size is in the range of 5-10 nm and more uniform at 300 ºC and it is also in the range of mesoporous material category (IUPAC definition 2-50 nm). Nevertheless, at 500 ºC, the surface area

reduces and the pores become almost flat, no hysteresis or obvious pore size distribution, indicating the collapsing of the pores.

The BET surface area, BJH average pore size, and pore volume data of the LCoP-60 sample are depicted in Table 3.3. The surface area and the average pore volume of LCoP-60 decrease with the increasing temperature whereas the average pore size increases as expected because the pores are getting larger with temperature treatment.

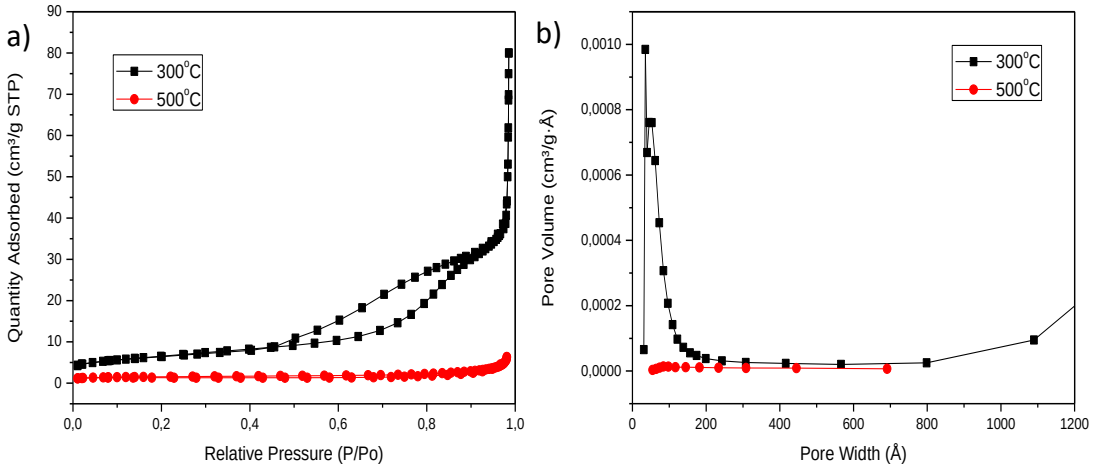

Figure 3.32. a) Linear isotherm plot and b) BJH pore size distribution of LCoP-60 for 300 and 500 °C.

Sample (LCoP)	BET Surface Area (m^2/g)	BJH Pore Size (Å)	BJH Pore Volume (cm^3/g)
300°C	23	148	0.124
500°C	5	281	0.008

Table 3.3. The BET surface areas, the BJH pore sizes and pore volumes of LCoP-60 at 300 and 500 °C.

The effect of calcination temperature (at 300 and 500 °C) was investigated using FTIR spectroscopy. Figure 3.33 shows the main change is in the phosphate region (1250-500 cm^{-1}). The peaks of P-O stretching and bending are broad at 300 °C

because the sample is amorphous whereas at 500 ºC these peaks are well-resolved and characteristic for the crystalline olivine phase of LCoP. Notice that the broad peak at around 1051 cm^{-1} splits into 3 different peaks, located at 1068, 1002 and 945 cm^{-1} in the P-O stretching region and the other broad peak at around at 593 cm^{-1} splits into 4 different peaks at 636, 596, 582 and 561 cm^{-1} in the bending region of the phosphate units.

Moreover, there is a small difference between the LMnP and LCoP samples. The nitrate peak (around 1384 cm^{-1} at 300 ºC) shown in the LMnP case disappear in the LCoP samples even at 300 ºC; it means that 300 ºC is sufficiently high to decompose nitrate in the LCoP samples.

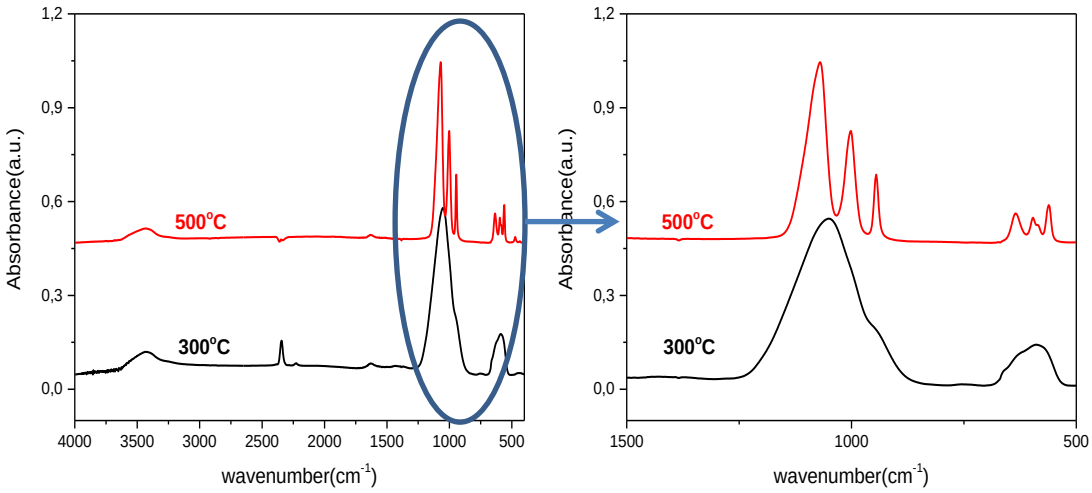

Figure 3.33. FTIR spectra of LCoP-60 at 300 and 500 ºC

3.5. Synthesis of Mesoporous Lithium Nickel Phosphate

After the manganese (II) and cobalt (II) systems, synthesis of mesoporous lithium nickel (II) phosphates were also optimized by applying the same produce. Similar to LCoP samples, there was no precipitation while preparing the S-LNiP solutions. The solutions were clear after combining the solution A and B as mentioned in the experimental section and they remained stable for a long time. For the synthesis of LNiP, the solutions were spread on glass substrate and used for the mesophase characterization and mesoporous forms after calcination process.

Firstly, the mesophases of the all mole ratios of LNiP samples were analyzed using small angle XRD, see Figure 3.10 (c). The LNiP-90 mole ratio was chosen for the further characterization. The solutions of LNiP-90 were spread on the microscope slides and calcined at different temperatures starting from 50 to 300 ^{o}C with an increment of 50 ^{o}C in a pre-heated oven for 1 hour at each temperature. In order to analyze the temperature dependent trend, one sample of LNiP-90 was aged at room temperature as well. The difference among the samples calcined at different temperatures could be observed even by the naked-eye, see Figure 3.34. The color of the samples was quite different from each other. When the calcination temperature increases, the color of the sample differentiate from greenish to yellow. Moreover, the external appearance of the samples varied from gel form to opaque form.

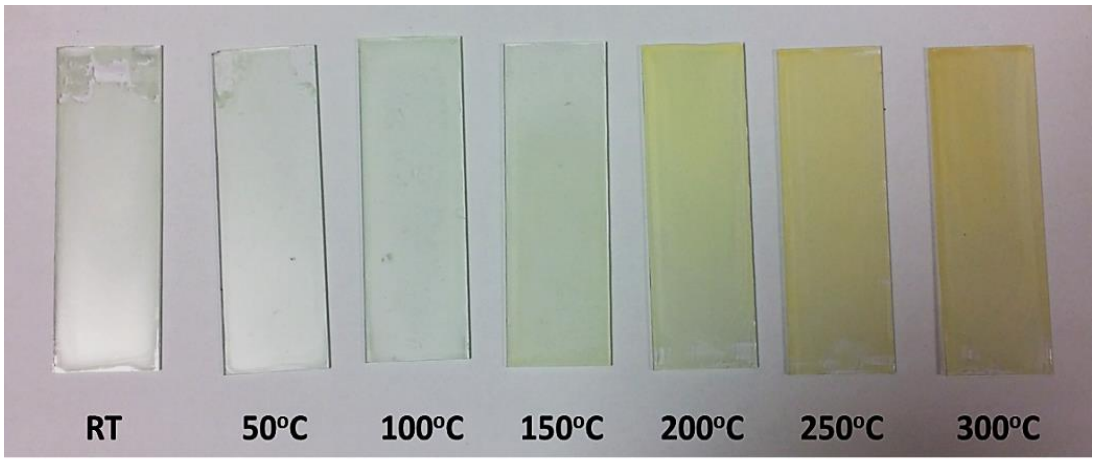

Figure 3.34. Photos of calcined LNiP-90 samples at different temperatures.

The small angle XRD patterns of the LNiP-90 sample were recorded at different calcination temperatures. The mesophases of the LNiP-90 are not stable to a mild heat treatment. Meso-order is completely lost when the calcination temperature reached to 200 ^{o}C, see Figure 3.35. The diffraction lines at RT lose their intensity with heating even at low temperatures.

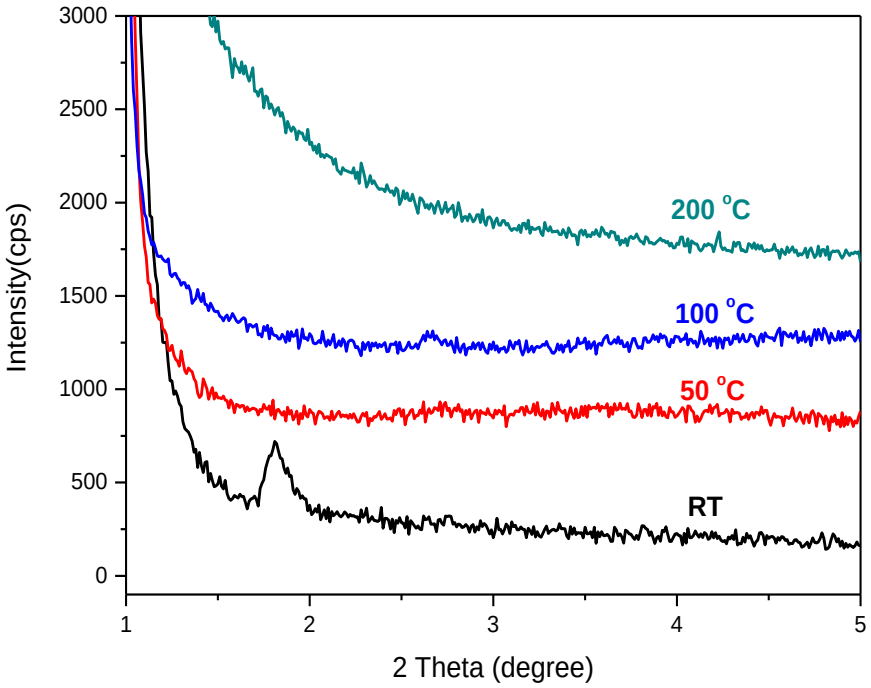

Figure 3.35. Small angle XRD pattern of LNiP-90 mole ratio at different temperatures.

The LNiP-90 samples (from 50 to 300 ^{o}C) were further analyzed using FTIR spectroscopy. The spectra were collected by pressing KBr pallets (around 0.01 g sample in 0.19 g KBr), see Figure 3.36. Since up to 200 ^{o}C the sample of LNiP-90 is like gel, it was hard to grind the sample with KBr; it was sticky and preparing pellets required careful effort. According to the spectra, the samples contain water as shown in the O-H stretching (at around 3500 cm^{-1}) and bending (at around 1600 cm^{-1}) regions. With increasing calcination temperature, the intensity of these peaks diminishes. Moreover, there is a sharp peak at around 1386 cm^{-1} due to KNO_3, indicating the presence of nitrate in the samples. The surfactant related peaks, at around 3000-2800 cm^{-1}, decreases with increasing calcination temperature, because the surfactant and temperature dependent decomposition products burn out. The phosphate related peaks are almost the same and quite broad for both stretching and bending regions in all samples, calcined at different temperatures at which the materials are still amorphous.

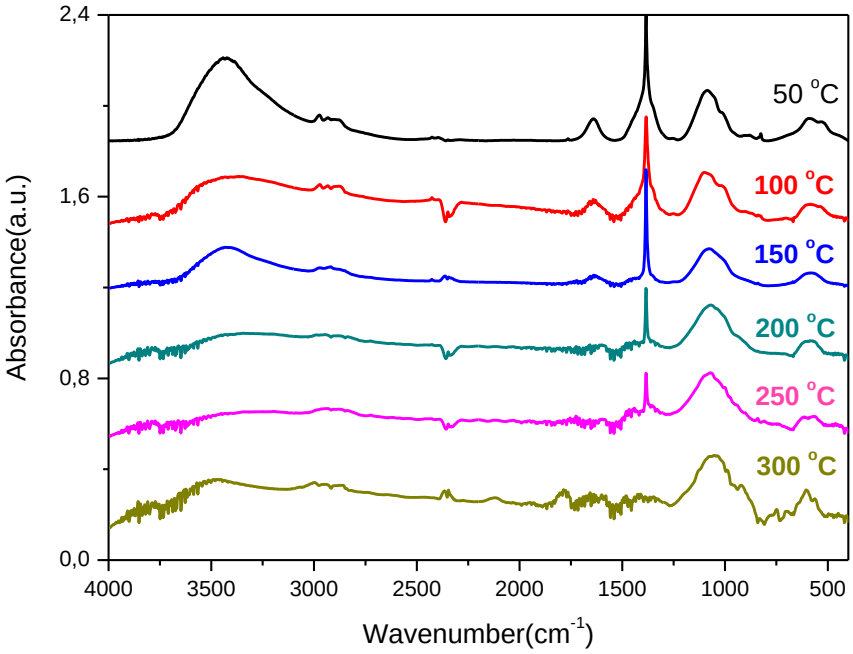

Figure 3.36. FTIR spectra of LNiP-90 at different temperatures.

Even at RT, the particles started to form. The shapes of the particles at RT are not spherical but at as low as 50 °C the particles become spherical, compare the SEM images in Figure 3.37. Actually, they are mesoporous after 250 °C at which the surfactant species burn out and create porous structure in the samples. However, it is difficult to observe the mesoporosity in the SEM images due to low resolution and relatively smaller pores; see Figures 3.37-38.

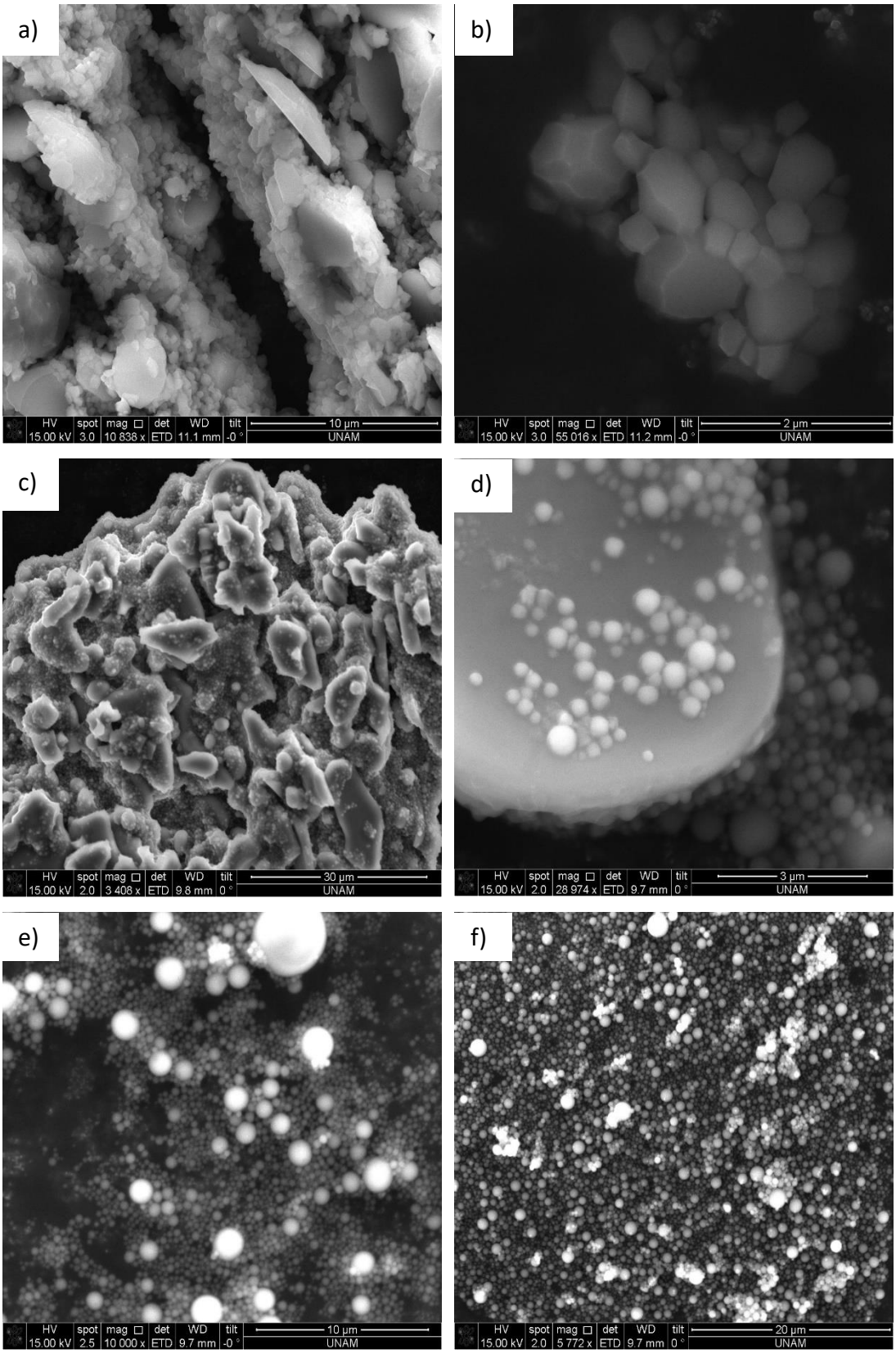

Figure 3.37. SEM images of LNiP-90 at a) and b) RT, c) and d) 50 ^{o}C, e) 100 ^{o}C, and f) 150 ^{o}C.

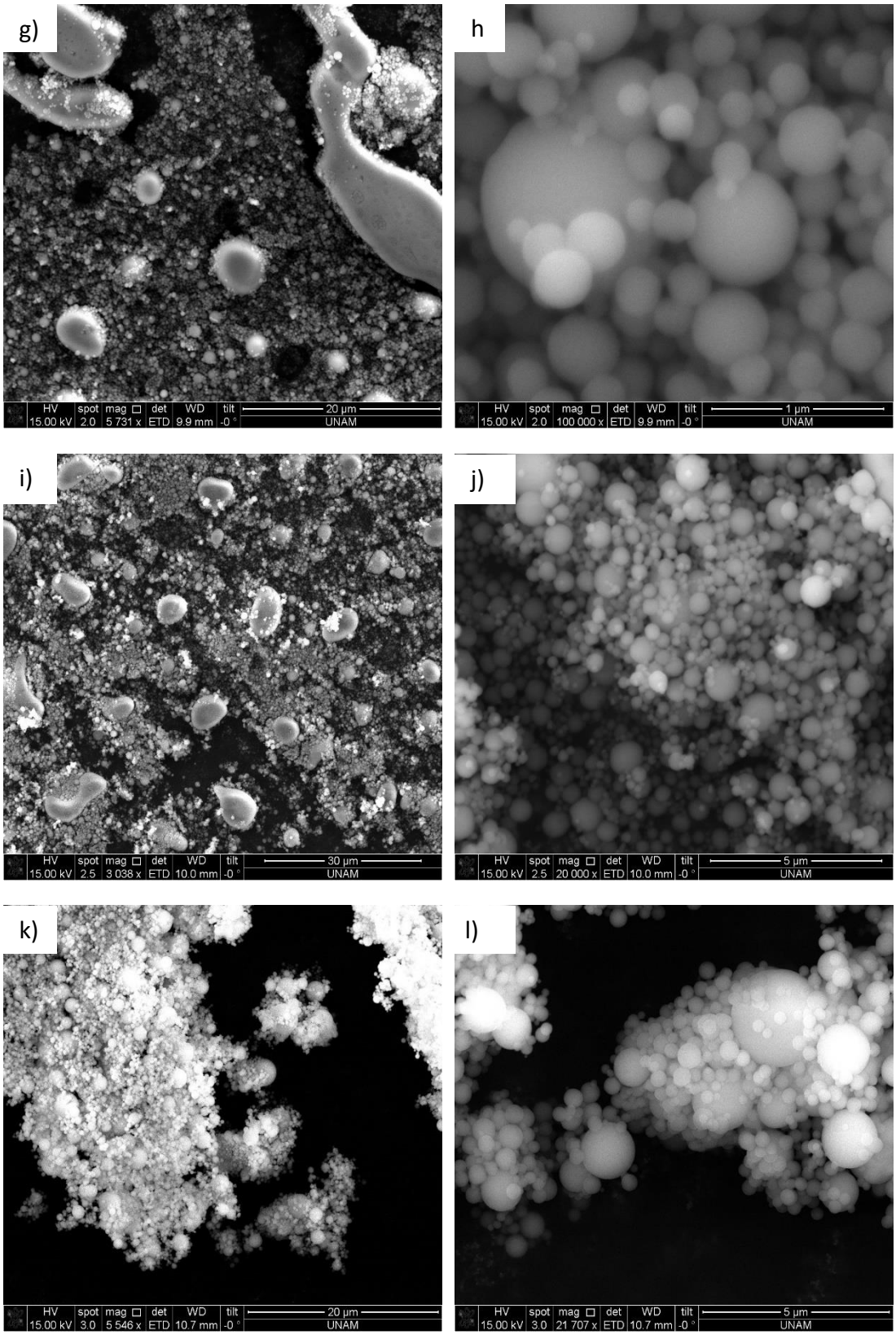

Figure 3.38. SEM images of LNiP-90 at g) and h) 200 ºC, i) and j) 250 ºC, and k) and l) 300 ºC.

The samples were further investigated at higher temperatures in order to determine the crystallization temperature and the structure of LNiP-90. For this purpose, the samples were calcined at 400 ºC and annealed at higher temperatures. Up to 500 ºC, there is no crystallization in the LNiP, opposed to LMnP and LCoP samples, which were crystalline at 400 ºC. As shown in Figure 3.39 (a), the LNiP-90 sample is completely crystalline at 500 ºC. However, the diffraction pattern of the crystalline sample at 500 ºC is very different from that of olivine phase of $LiNiPO_4$, see Figure 3.39 (b).

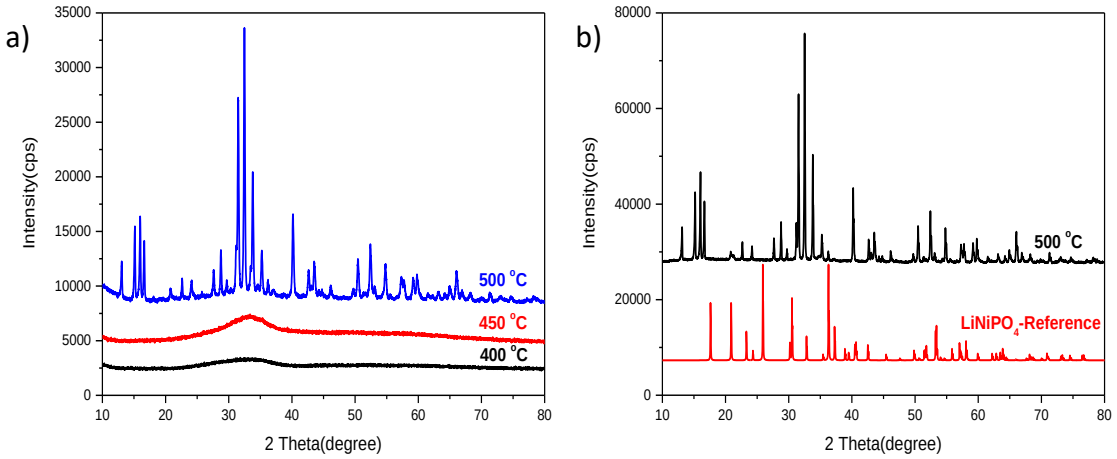

Figure 3.39. High angle XRD patterns of LNiP-90 a) at 400, 450, and 500 ºC and b) 500 ºC and $LiNiPO_4$ reference with PDF-card no 00-032-0578.

In order to synthesize the target material (olivine phase of $LiNiPO_4$), firstly we tried to increase the amount of lithium salt in the initial solutions. The new solutions were prepared by adding excess 10 and 20% $LiNO_3$ salt keeping the other ingredients and the methodology of the sample preparation same. Then, the new solutions were spread on glass slide and calcined and annealed as before.

As shown in Figure 3.40, with the increasing the amount of lithium salt by 10 and 20 %, the crystals of olivine phase of $LiNiPO_4$ are obtained with some of the unknown phase.

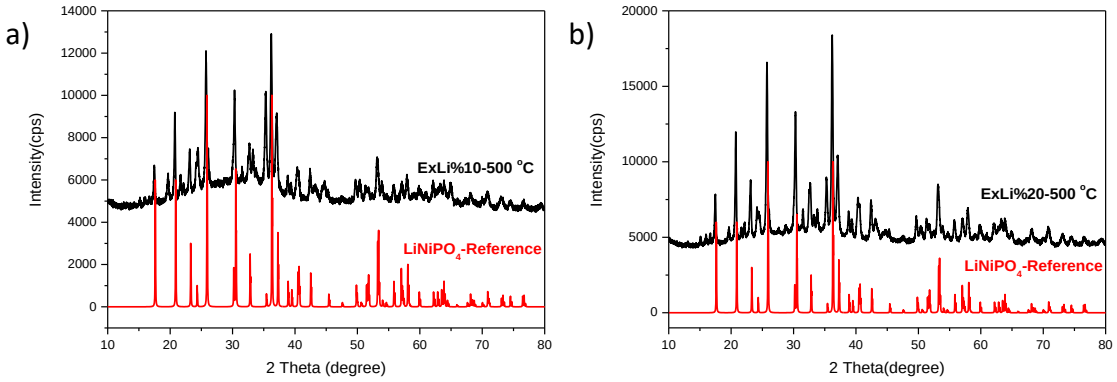

Figure 3.40. High angle XRD patterns of LNiP-90 a) with 10% and b) with 20% excess lithium at 500 °C and $LiNiPO_4$ reference with PDF-card no 00-032-0578.

The samples were obtained by calcination at low temperature and annealing at higher temperatures. We also prepared samples by directly calcining the gels at 500 °C to determine the effect of calcination temperature. As shown in Figure 3.41, if the sample is calcined directly at 500 °C, the XRD patterns could not be indexed to the olivine phase, it is rather an unknown phase. However, calcination at 300 °C and annealing at 500 °C produced the olivine phase of $LiNiPO_4$ with a small amount of the unknown phase. Further increasing the lithium into the solution increased the amount of olivine phase with a smaller amount of the unknown phase as impurity. The aim of excess lithium was to obtain a pure olivine phase. Therefore, increasing the amount of lithium salt is not a successful attempt for the synthesis of olivine phase of $LiNiPO_4$.

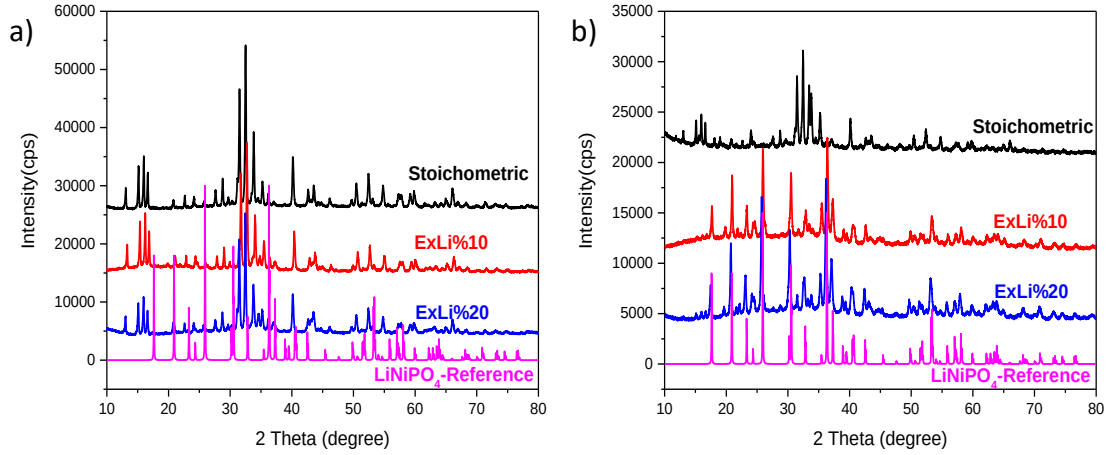

Figure 3.41. High angle XRD patterns of LNiP-90, exLi%10, exLi%20 and $LiNiPO_4$ reference with PDF-card no 00-032-0578 a) at direct 500 °C and b) at annealed 500 °C.

The samples, obtained from direct calcination and calcination at low and annealing at 500 ^{o}C, were also analyzed using ATR-FTIR spectroscopy. Because the unknown and olivine phases have quite different spectra, see Figure 3.42. The calcined/annealed samples have much broader peaks, whereas the peaks of the direct calcined samples are quite sharp in the phosphate stretching and bending regions. The directly calcined samples, prepared from both 10 and 20% excess lithium, have almost the same spectra in phosphate regions. However, the samples that are calcined in two steps (calcination at low and annealing at high temperature) have different peak shapes in the 10 and 20% excess lithium samples. The peaks are much sharper in the 20% excess sample compared to that of the 10% excess lithium sample, compare spectra in Figure 3.42. It is showing that the sample, prepared using 20% excess lithium, has more unknown phase(s) than the 10% sample.

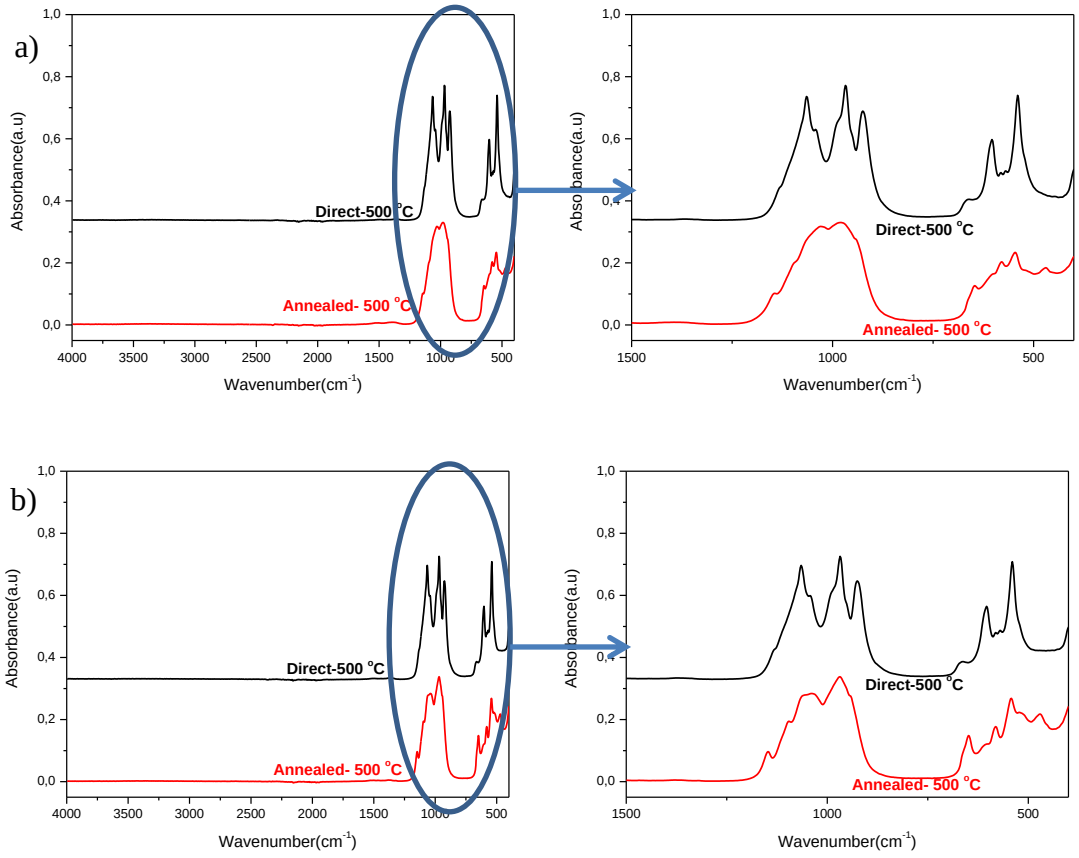

Figure 3.42. ATR-FTIR spectra of LNiP-90 with a) 10% excess lithium and b) 20% excess lithium for both annealed and direct calcination at 500 ^{o}C.

Since the addition of an excess amount of lithium salt did not solve the problem of synthesis of pure olivine phase, another method was employed. This time, we played with the pH of the solution by using LiH_2PO_4 in different mole ratios in place of $LiNO_3$ and H_3PO_4 as the lithium and phosphate source. Replacing the lithium salt and PA with LiH_2PO_4 has an advantage of reducing the nitrate concentration and reduces the number of ingredients in the solution media. Moreover, it changes the pH of the solution from around 1 to around 2-3 that may also be useful to obtain different morphologies, like films. However, it has also disadvantage; the solutions of LNiP-90 with the LiH_2PO_4 are not stable compared to normal S-LNiP-90 solutions, prepared from $LiNO_3$ and PA. Some precipitations occur in the solution phase. Additionally, dissolving LiH_2PO_4 is much harder and it takes longer time to obtain clear solutions. To decrease the amount of precipitation and the solvation problem, diluter solutions were prepared. The total amounts of the solutions are given in Table 3.4. The LNiP-90-x:y is the abbreviation, where x:y is referring to percentage of LiH_2PO_4 to $LiNO_3$ and H_3PO_4. Solutions of the LNiP-90-x:y were also prepared by using two different vials, solutions A and B. Moreover, similar to the other solutions, the water amount was kept 10 ml. As mentioned, the dissolving of the salts is harder; therefore longer stirring time is required (around 2 days).

LNiP-90-**x:y**	P123	$[Ni(H_2O)_6](NO_3)_2$	LiH_2PO_4	$LiNO_3$	H_3PO_4
0:100	0.5 g	2.276 g	0 g	0.540 g	0.900 g
25:75	0.5 g	2.276 g	0.203 g	0.404 g	0.625 g
50:50	0.5 g	2.276 g	0.407 g	0.270 g	0.450 g
75:25	0.5 g	2.276 g	0.610 g	0.135 g	0.225 g
100:0	0.5 g	2.276 g	0.814 g	0 g	0 g

Table 3.4. Amounts of ingredients used in the solutions of LNiP-90 using LiH_2PO_4.

Upon preparation of the clear and homogeneous solutions, they were coated on glass substrate and calcined at higher temperature to obtain olivine phase of LNiP. In the calcination process, two steps process was employed, where the direct calcination did not work for this system. Upon calcination at 300 ^oC and annealing at 500 ^oC, the

XRD patterns were recorded, see Figure 3.43. As shown in the figure, the pattern of the sample without LiH_2PO_4 displayed the unknown phase, the sample with increasing LiH_2PO_4 amount produced the olivine phase. Increasing the pH of the solution worked better; but still there is unknown phase inside our materials. Notice that the LNiP-90 25:75 and LNiP-90-100:0 samples do not look fully crystalline; there is a little bit amorphous phase in the samples. The reason could be the calcination duration and temperature that may not be long and high enough, respectively, to obtain fully crystalline phase.

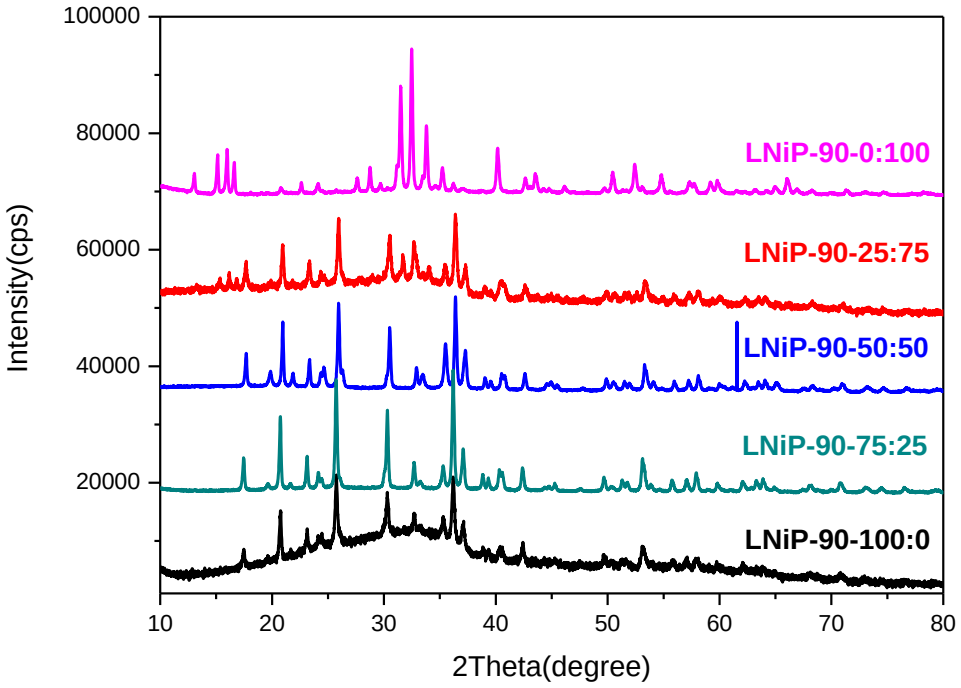

Figure 3.43. High angle XRD patterns of LNiP-90-x:y samples at annealed 500 ^oC.

These samples were also investigated using an ATR-FTIR spectroscopy. The only peaks in the spectra originate from the phosphate units in the samples annealed at 500 ^oC. As shown in Figure 3.44, there is significant difference between the samples, prepared with and without LiH_2PO_4. In the LNiP-90-0:100 sample, there is a shoulder at 1135 cm^{-1} and other peaks located at 1064, 1041, 990, 967, and 926 cm^{-1} in the stretching region of phosphate. The peaks from bending modes are located at 672, 605, and 537 cm^{-1}. In the spectra of LNiP-90-50:50 and 75:25 samples, the stretching modes are observed at 1148, 1101, 1066, and 963 cm^{-1}, whereas the peaks at 664, 650, 580, 545, 514 and 473 cm^{-1} belong to the bending modes of phosphate.

Notice that the LNiP-90-25:75 and 100:0 samples have very broad peaks in both stretching and bending regions due to amorphous parts of the samples, as mentioned in the XRD discussion section.

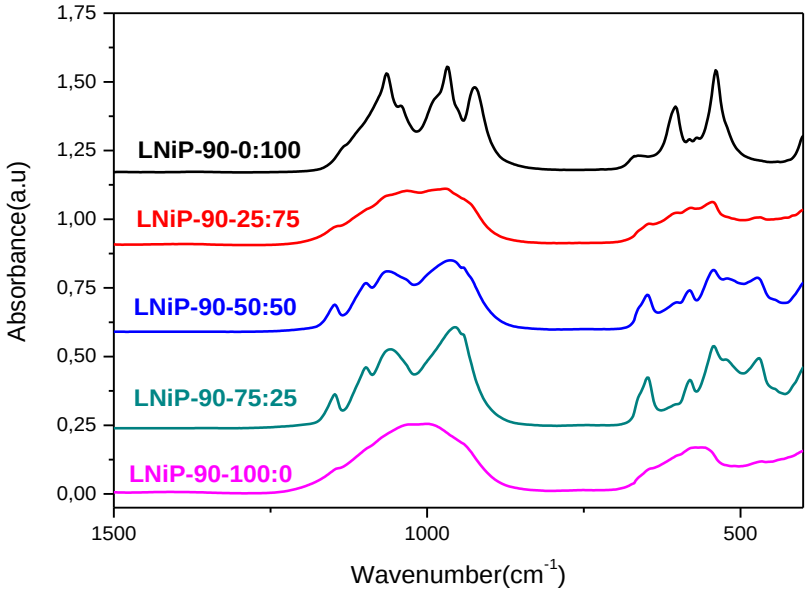

Figure 3.44. FTIR-ATR spectra of LNiP-90-x:y samples at annealed 500 ^{o}C .

The SEM images of the LNiP-90-x:y samples were collected in order to show the morphologies of the materials at 300 ^{o}C. The samples, calcined at 300 ^{o}C, were preferred because the porosity is more obvious in those samples. When the samples are annealed at 500 ^{o}C, all the pores are collapsed and the shapes of the materials are damaged. As shown in Figures 3.45 and 46, the morphology of the samples is changing with increasing the percentage of LiH_2PO_4 in the solutions. The particles are perfect spheres without LiH_2PO_4. However, with increasing the amount of LiH_2PO_4, the spherical particles come together and form film like structures. Over the LNiP-90-%-50:50 samples, the spherical particles disappear and the film morphology dominates, see Figure 3.45.

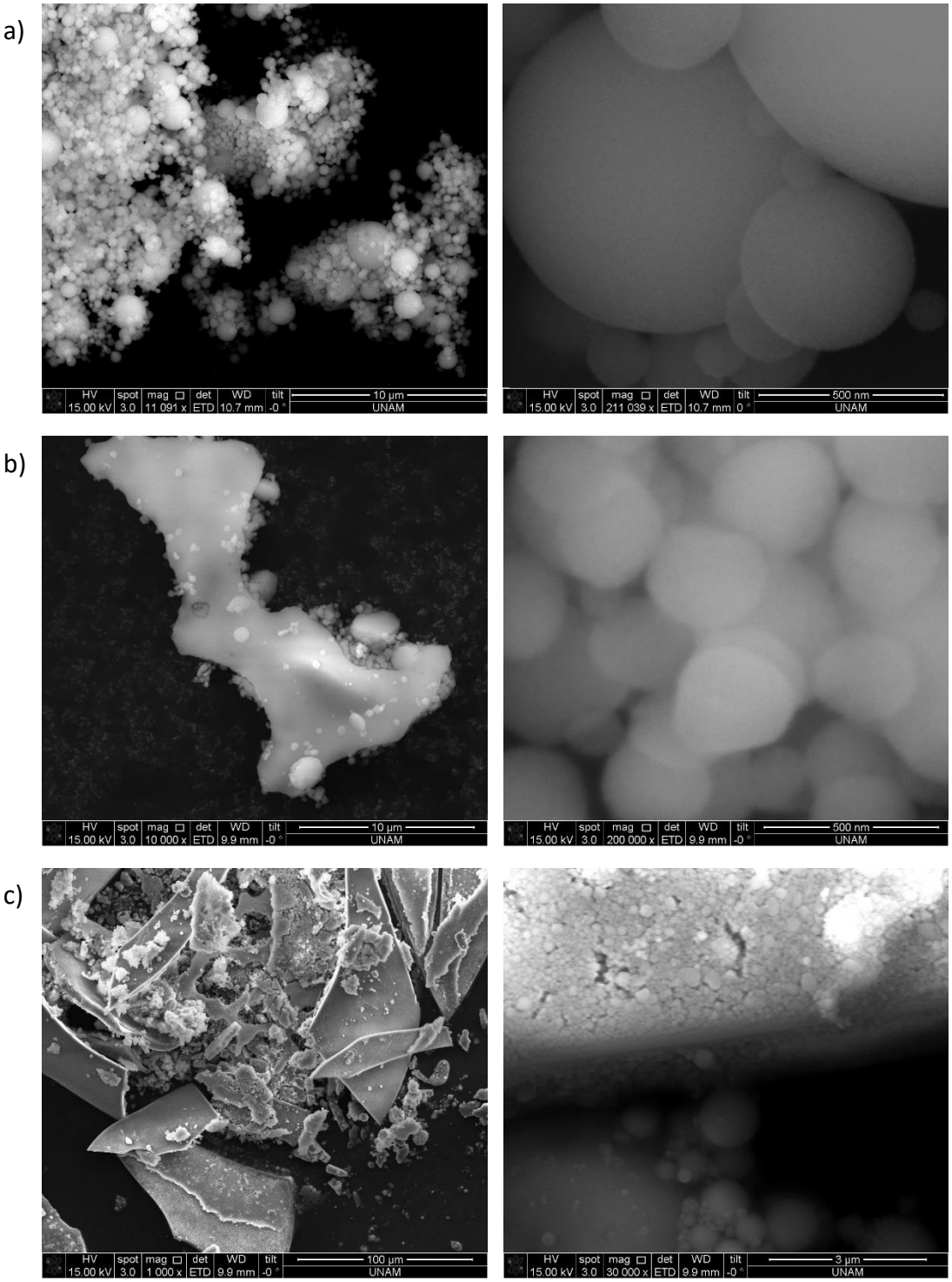

Figure 3.45. SEM images of a) LNiP-90-0:100, b) LNiP-90-25:75, and c) LNiP-90-50:50 at 300 ºC (all right one zoomed of the left images).

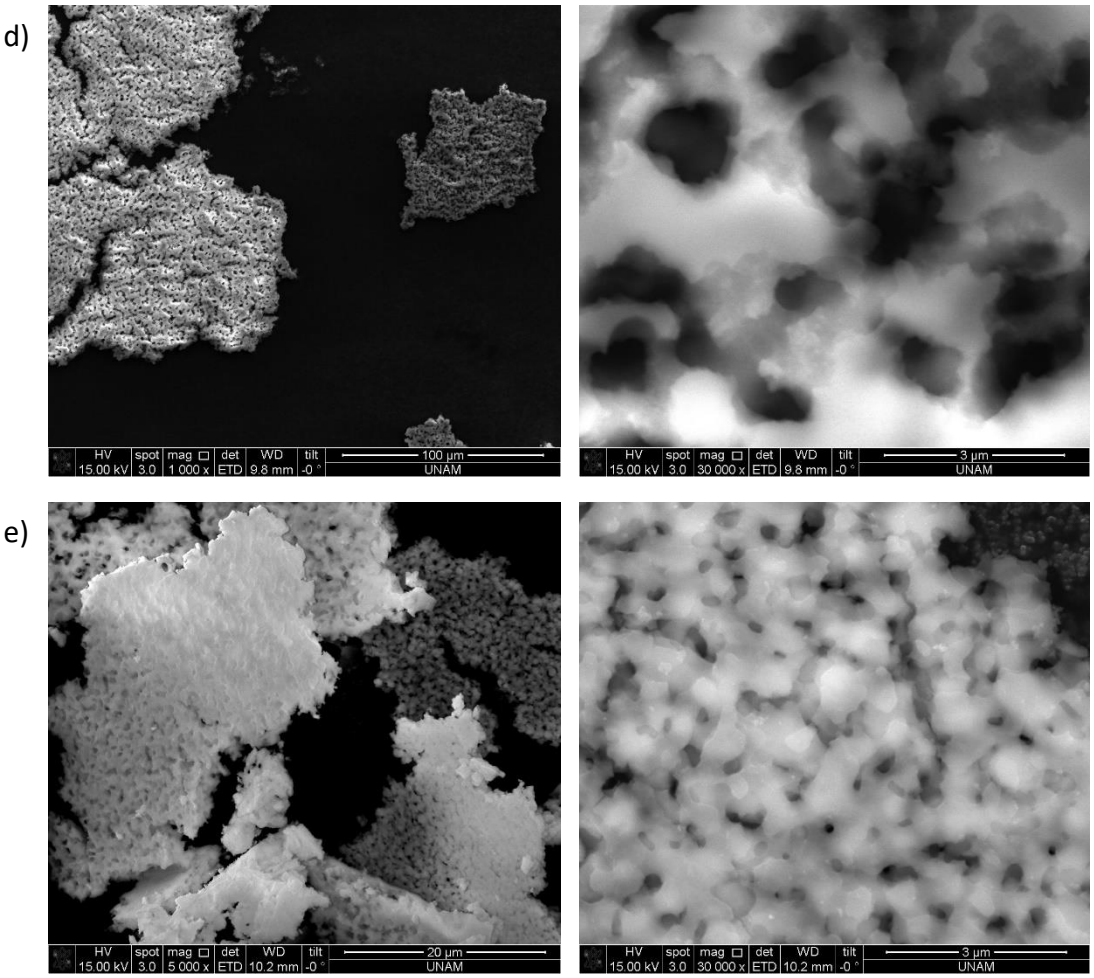

Figure 3.46. SEM images of d) LNiP-90-75:25 and e) LNiP-90-100:0 at 300 ºC (all right one zoomed of the left images).

For further characterization of the LNiP-90 samples, a washing method was also employed to determine if washing could remove surfactants from the pores in place of calcination. Fist, the samples that were aged at RT on microscope slide for 1 day were analyzed to determine the gelation time. The aged samples were collected by washing the slides one by one and then centrifuged at 6000 rpm for 10 sec so that the supernatant including surfactant was disposed. The centrifugation was repeated 3 times to make sure all the surfactant species and unreacted inorganics were washed out from the samples. Finally, the samples were washed using pure ethanol and dried.

The washed samples were characterized by ATR-FTIR spectroscopy to check whether the surfactants are removed from the samples. As shown in Figure 3.46, the surfactant peaks at around 3000-2800 cm^{-1} disappeared in the spectrum of the washed sample, see Figure 3.47. Therefore, it is possible to obtain mesoporous samples without calcination process. Moreover, the nitrate peak at 1336 cm^{-1} is also disappeared by the washing process, as expected. The only peaks remain in the spectrum are due to some water and phosphate units.

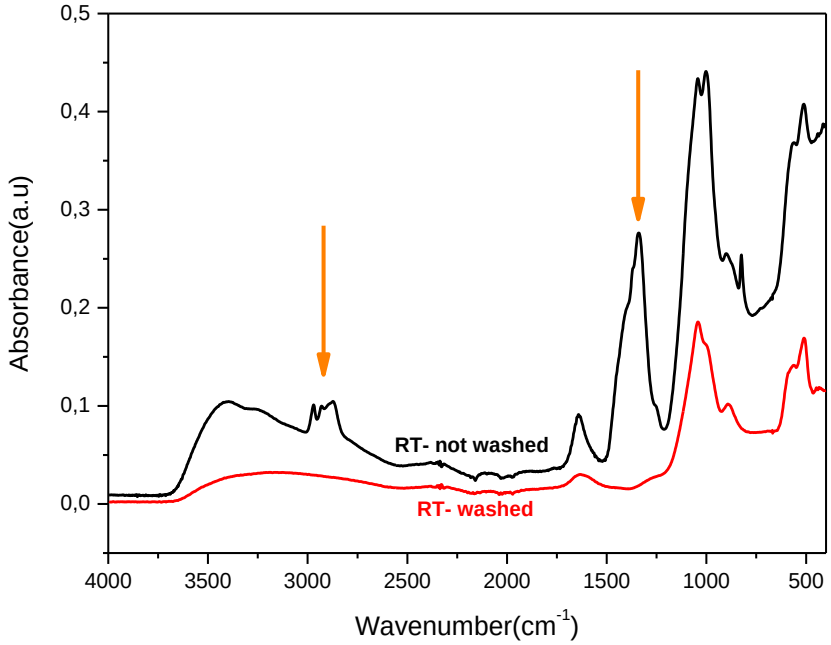

Figure 3.47. ATR-FTIR spectra of LNiP-90 at RT both washed and unwashed forms.

The washed samples were also investigated by SEM to show the porosity after washing process. As expected, the washed samples show mesoporosity as shown in the SEM images in Figure 3.48.

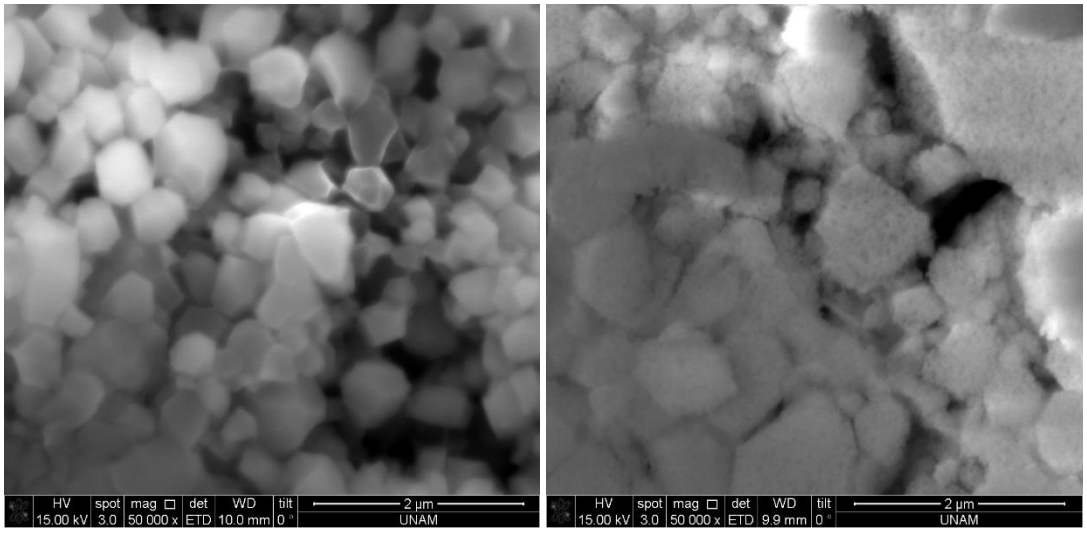

Figure 3.48. SEM images of LNiP-90 at RT before (left) and after washing (right).

The unknown phase in the LNiP-90 sample is obtained when the samples are calcined directly at 500 ºC over glass substrates. However, if the samples is calcined at 300 ºC over glass slides and annealed in an alumina ash tray, the product is predominantly the olivine phase of LNiP.

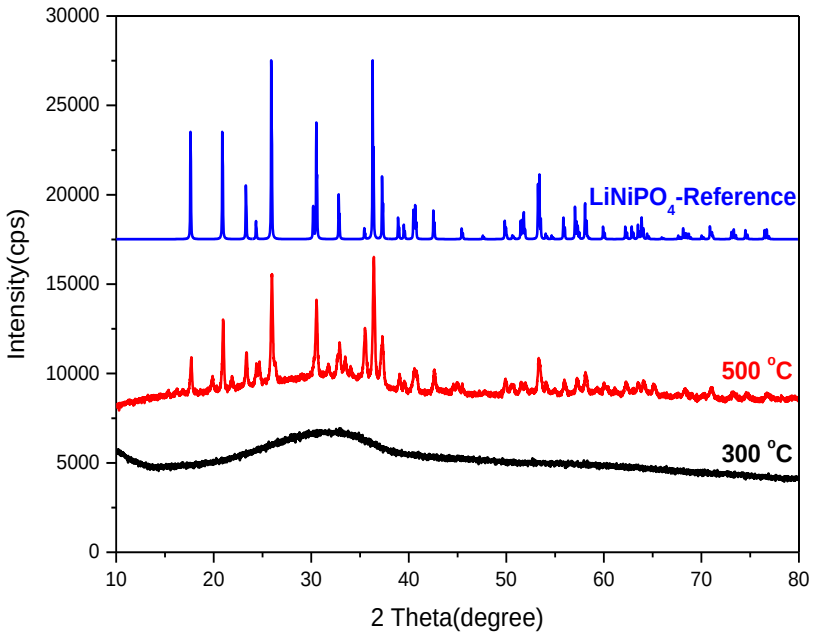

Figure 3.49. High angle XRD patterns of LNiP-60 at 300, 500 ºC and olivine $LiNiPO_4$ reference, PDF-card no 00-032-0578.

The LNiP-60 sample, calcined in two steps, was also analyzed using ATR-FTIR spectroscopy. Since at 300 ºC, the material is amorphous the peaks are quite broad. However, it is crystalline at 500 ºC and the broad peaks splits into 4 peaks at 1147, 1097, 1047, and 974 cm^{-1} in phosphate stretching and 648, 605, 581, 548, and 475 cm^{-1} in the bending region, see Figure 3.50. These peaks are not sharp; maybe due to presence of the amorphous phase.

The SEM images were also collected at both temperatures. The particles are perfect spherical at both temperatures (300 and 500 ºC). The pores of the particles are visible, see Figures 3.51 and 52. The pores are better resolved in the samples, annealed at 500 ºC because the pores are much larger (Figure 3.52). Even though the pores collapse at 500 ºC, the morphology of the LNiP-60 sample is still preserved as in the samples just calcined at 300 ºC (see Figure 3.51).

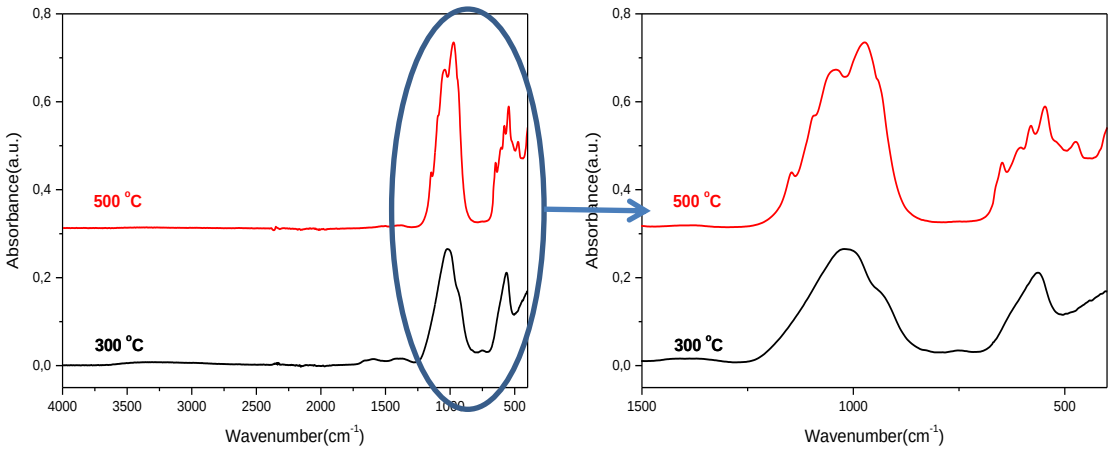

Figure 3.50. ATR-FTIR spectra of LNiP-60 at 300 and 500 ºC.

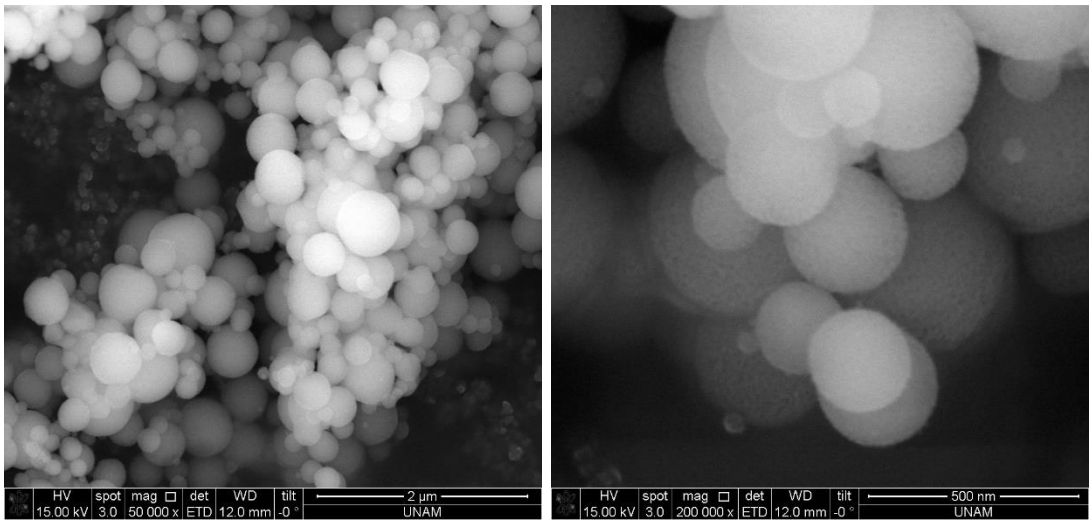

Figure 3.51. SEM images of LNiP-60 at 300 ºC at different magnifications

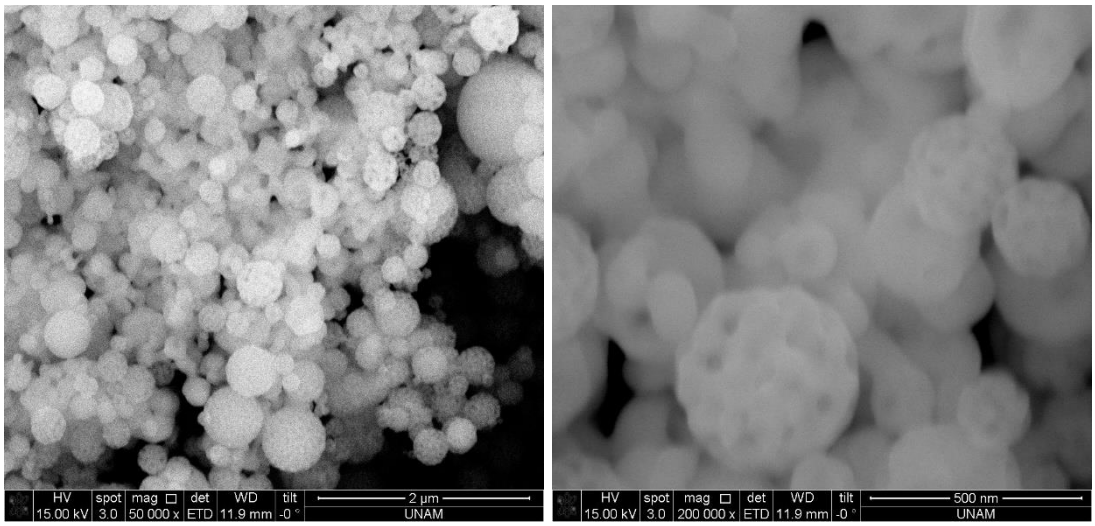

Figure 3.52. SEM images of LNiP-60 at 500 ºC at different magnifications

The TEM images were also collected from the LNiP-60 samples, calcined at 300 ºC. Figure 3.53 shows the uniform mesopores with a pore size of 5-8 nm. Notice that the TEM images are also showing the perfect spherical shapes.

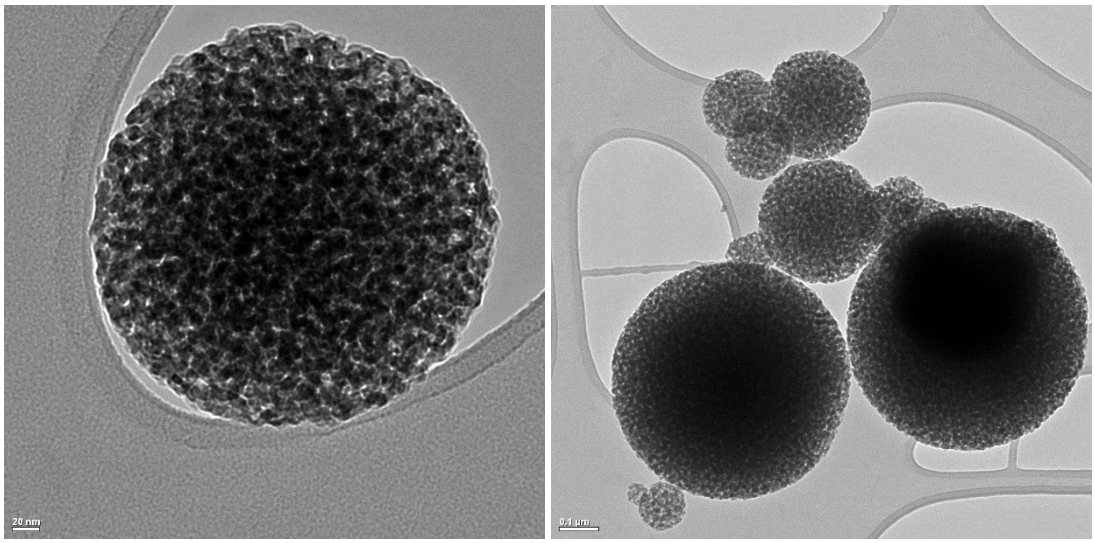

Figure 3.53. TEM images of LNiP-60 at 300 ^{o}C at different magnifications.

The N_2 adsorption-desorption isotherms were measured to determine details of the surface and pore parameters from the LNiP-60 samples. Similar to other transition metal LMPs, the LNiPs also have a H1 hysteresis in their isotherms, indicating a narrow range of uniform mesopores. [88] Moreover, if the calcination temperature reaches to 500 ^{o}C, the hysteresis in the isotherm remains (see Figure 3.54 (a)). Even at 500 ^{o}C, the LNiP has characteristics of mesoporous materials. As depicted in the pore volume versus pore width graph (see Figure 3.54 (b)), the pore size of LNiP-60, calcined at 300 ^{o}C, is in the range of 5-8 nm and it further expands at 500 ^{o}C. As an expense for a large pore size, the surface area diminishes at 500 ^{o}C.

BET surface areas, BJH average pore sizes and pore volumes values of LNiP-60 are tabulated in Table 3.5. The surface area and average pore volume of the sample decrease whereas the average pore size increases with increasing temperature.

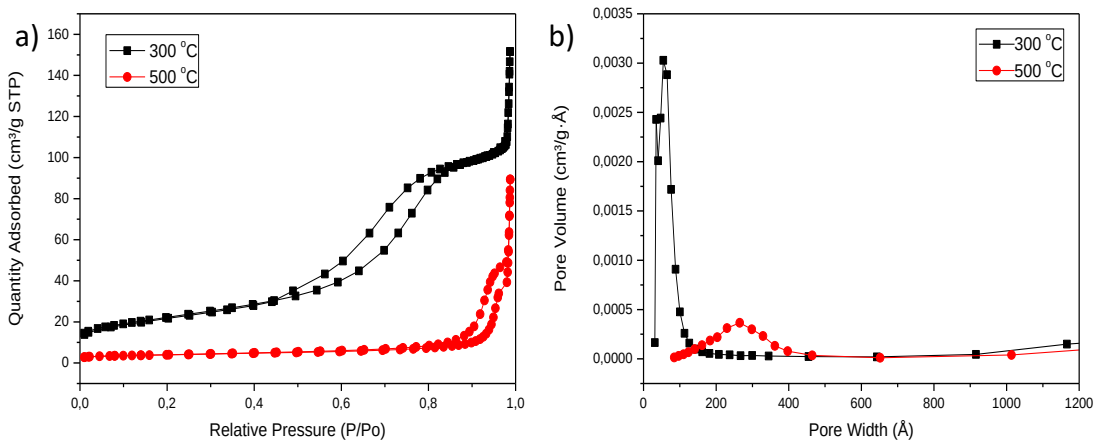

Figure 3.54. a) Linear isotherm plot and b) BJH pore size distribution of LNiP-60 for 300 and 500 °C.

Sample (LNiP)	BET Surface Area (m^2/g)	BJH Pore Size (Å)	BJH Pore Volume (cm^3/g)
300 °C	79	89	0.236
500 °C	14	426	0.137

Table 3.5. The BET surface areas, the BJH pore sizes and pore volumes of LNiP-60 at 300 and 500 °C.

3.6. Synthesis of Mesoporous Lithium Iron Phosphate

After manganese, cobalt and nickel systems were worked in detail; the synthesis of mesoporous LFeP systems was also tried. For this purpose, firstly the chemicals mentioned in the experimental section in Table 2.2 were used to prepare the solutions of S-LFeP. Since in the other systems 90 and then 60 mole ratios were chosen as a more optimized ratios, in the iron case these ratios were also utilized. The synthesis part was started by using Li(I) nitrate and Fe(III) nitrate with fixed amounts of PA and P123. The mesophases of LFeP systems was not analyzed too much since the small angle XRD patterns of the other metals could not give too much information. The mesostructure analysis was skipped so that the final product of mesoporous LFeP would be analyzed more. First, as an iron source, $Fe(NO_3)_3$ was used by assuming the formation of LFeP will force the Fe(III) to go to Fe(II). Moreover, the

other reason to start with Fe(III) is because as a salt of iron we wanted to use nitrate salts which is easy to remove at higher annealing temperatures. Then, the solutions were prepared with the same procedure, spread on glass slides, and calcined at different temperatures.

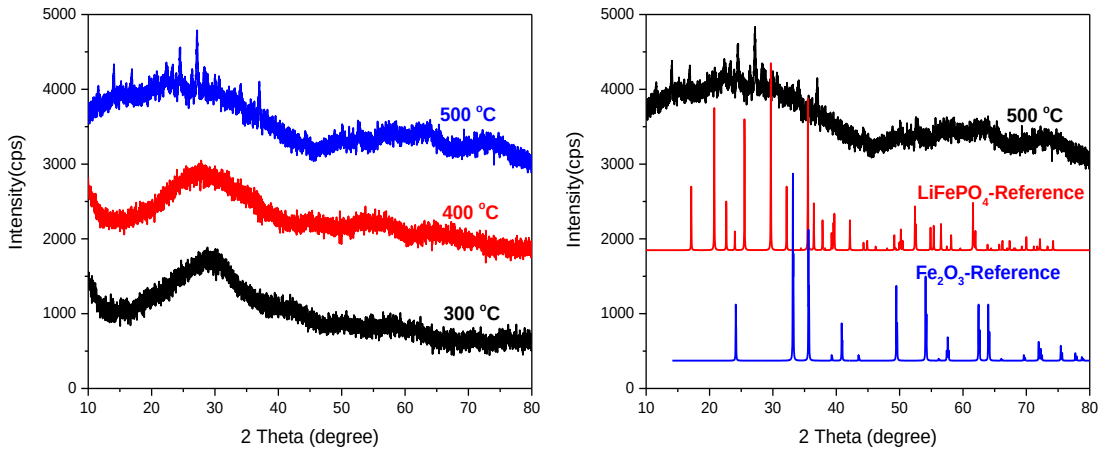

Figure 3.55. XRD patterns of LFeP-90 with NO_3^- salts (left) at different temperature, (right) at 500 °C and $LiFePO_4$ reference with PDF-card no 00-040-1499, and Fe_2O_3 reference with PDF-card no 00-033-0664.

As shown in Figure 3.55, the sample is amorphous at 300 and 400 °C whereas at 500 °C, the sample starts to crystalize. However, the crystals are not the olivine phase of LFeP, see right Figure 3.55. Notice that, there are some Fe_2O_3 formations even in the preparation of solutions and while calcination process.

Then, the precursor of iron was changed to $FeCl_2$ where the iron ion is already 2+ oxidation state. Accordingly, the lithium source was replaced to LiCl to prevent oxidation of Fe(II) by nitrate ion. However, it is impossible to obtain clear solutions using these two salts; there was a huge precipitation immediately. Therefore LiCl and $FeCl_2$ were used as sources of salts.

Moreover, the solution preparation was also switched from two vial preparation to one vial. In the general preparation method, the salts were dissolved first in the solution A, in the iron system when the water was added to the iron salt, it directly produced iron oxyhydroxide precipitates which can be recognized by naked eye, because the solution turns into a is red-orange color.

Therefore, for iron case first PA and P123 was put to 10 g of water in a 20 ml vial to dissolve completely. Then the salts were added to that solution and stirred for 1 day to obtain homogeneous solution, see Figure 3.56.

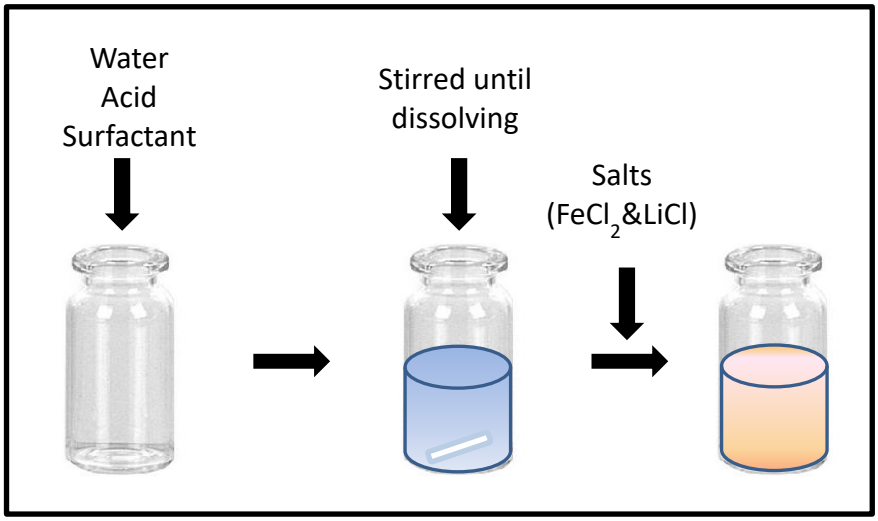

Figure 3.56. Schematic representation of solution preparation of LFeP with chloride salts.

However, the S-LFeP-60 with chloride salts was also not stable; some precipitates were formed at the bottom and walls of the vial, see Figure 3.57 (left). These precipitates were characterized as $FePO_4.2H_2O$ crystals from XRD data, shown in Figure 3.57 (right).

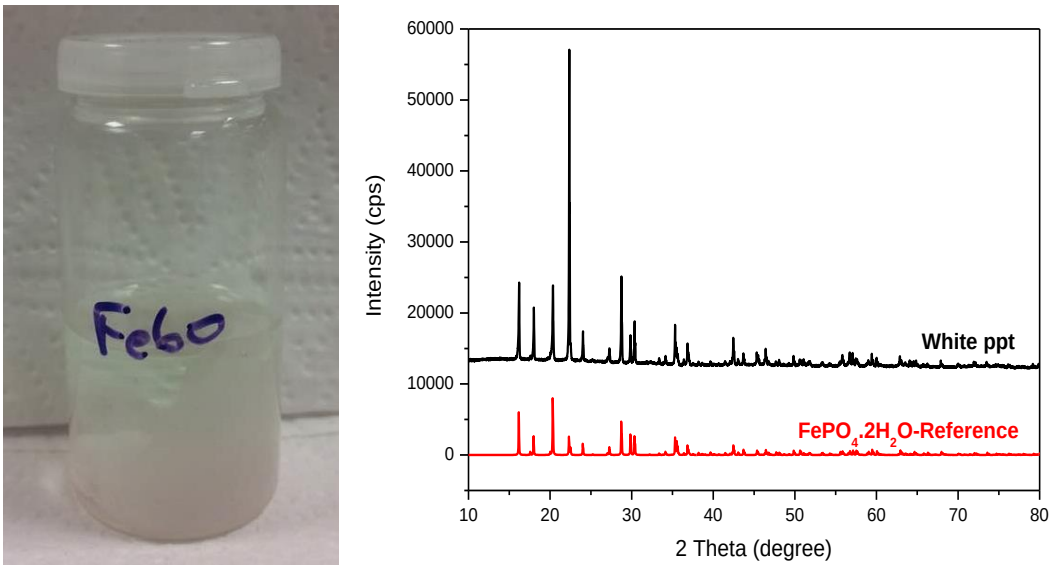

Figure 3.57. (Left) Picture of LFeP-60 solution with precipitates, (Right) high angle XRD patterns of precipitate and $FePO_4.2H_2O$ reference with PDF-card no 01-070-9911.

After centrifugation, the precipitate was removed and the clear part was used for the further process. However, since the solution is not stable, even the precipitate is removed from the solution; a new precipitation of the $FePO_4.2H_2O$ crystals occurs in a smaller quantity. Therefore, before calcination process, the precipitates were removed by centrifuge or the solutions were prepared freshly for further process.

The clear solutions were spread on glass substrate for calcination at 300 and 500 ^oC. The XRD patterns were collected to characterize the material of LFeP-60. As illustrated in Figure 3.58, the sample started to crystalline at 500 ^oC. However, indexing of the diffraction lines is difficult because the sample has many different crystalline phases. While some diffraction lines match with the monoclinic phase of $Li_2Fe_3(PO_4)_3$; there is also diffraction lines due to Fe_2O_3 that is difficult to prevent its formation and more importantly the most major composition is $Na_3Fe_2(PO_4)_3$ crystals. The formation of this sodium compound will be discussed in the later parts of the thesis.

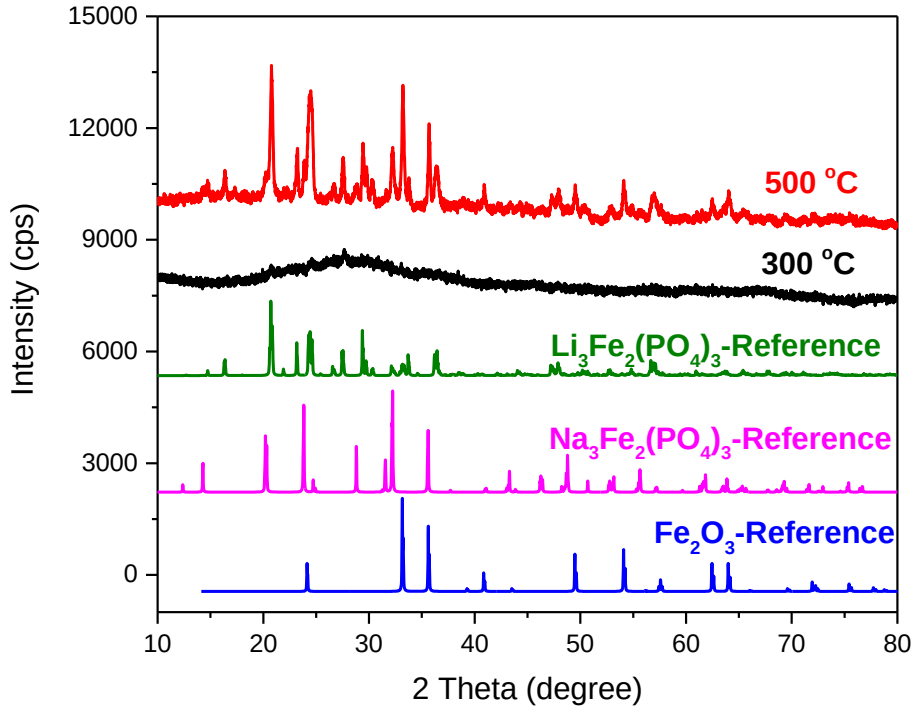

Figure 3.58. High angle XRD patterns of LFeP-60 synthesized by chloride salts and $Li_2Fe_3(PO_4)_3$ reference with PDF-card no 04-016-1665, Fe_2O_3 with PDF-card no 00-033-0664, $Na_3Fe_2(PO_4)_3$ with PDF-card no 00-045-0319

After XRD analysis, the morphologies of the LFeP-60 sample calcined at 300 and 500 ^{o}C were observed by utilizing SEM imaging. The morphology of the LFeP-60 at 300 ^{o}C differentiate from part to part of the sample and it is consistent with the XRD data that sample contains various species. There are some spherical particles and also there is film like structures, which are aggregated to each other, see Figure 3.59 (a) and (b). Moreover, there is a contrast difference in the film like particles which can be considered as mesopores. The morphology of the particles, calcined at 500 ^{o}C, see Figure 3.59 (c), is also quite different from the other cases. The general morphology of the sample is a film but there are also some rods and spherical particles. These different structures are likely due to presence of 3 different crystalline materials in the sample.

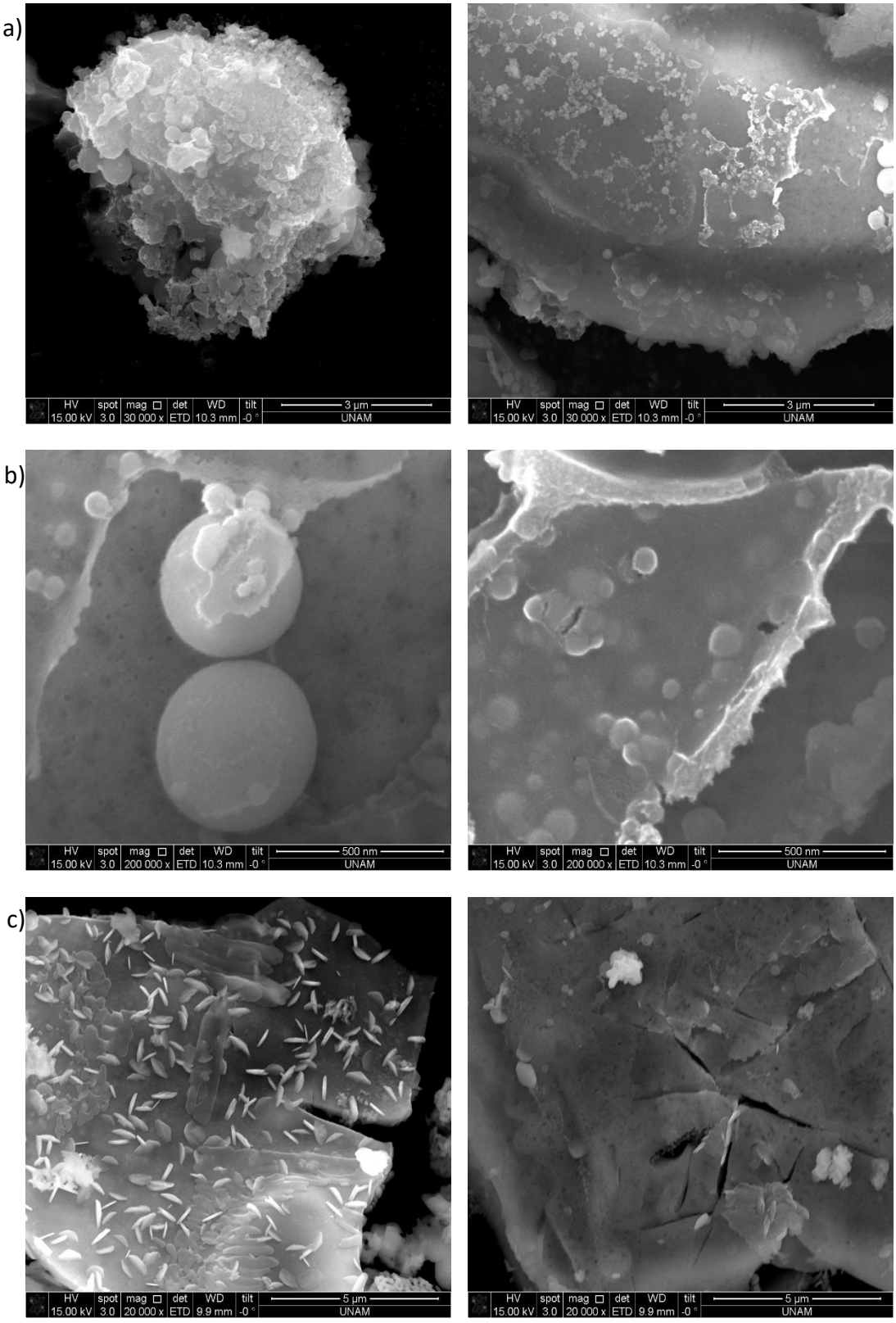

Figure 3.59. SEM images of LFeP-60 a) and b) at 300 ºC and c) at 500 ºC.

The N_2 adsorption-desorption isotherms were collected to investigate the porosity in the LFeP-60 samples, see Figure 3.60. The sample calcined at 300 ^oC has a hysteresis of H1 loop. Nevertheless, with increasing of calcination temperature, the hysteresis is mostly lost where the pore size expands. Moreover, the pore size of the sample, calcined at low temperature, is narrow but quite broad at higher calcination temperatures, indicating collapse of the pores in LFePs.

BET surface area, BJH average pore size, and pore volume values of the LFeP-60 are shown in Table 3.6. The surface area and the average pore volume of the sample decrease with the increasing temperature, whereas the average pore size increases.

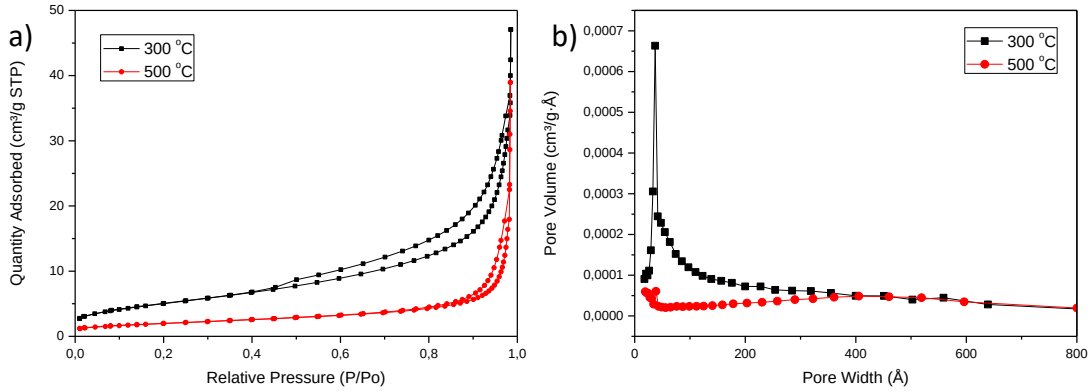

Figure 3.60. a) Linear isotherm plot and b) BJH pore size distribution of LFeP-60 for 300 and 500 ^oC.

Sample (LFeP)	BET Surface Area (m^2/g)	BJH Pore Size (Å)	BJH Pore Volume (cm^3/g)
300 ^oC	19	142	0.072
500 ^oC	7	367	0.060

Table 3.6. The BET surface area, the BJH pore size, and pore volume of LFeP-60 at 300 and 500 ^oC.

In order not to have any precipitation in the LFeP samples, we tried to add excess amount of acids, such as HCl or H_2SO_4 (around 1 g) while preparing the solutions.

Addition of excess acids prevented the precipitation in the solution. However, after calcination treatment, again we observed the formation of $Na_3Fe_2(PO_4)_3$ and $Li_3Fe_2(PO_4)_3$ crystals in the XRD patterns. In both crystal structures, iron is in 3+ oxidation state, which means that the Fe(II) does not stay stable while preparing the samples.

Note also that addition of an excess acid to the solution and then keeping the solutions in sealed (by parafilm) vials also decreases the amount of precipitation. Since the precipitates are $FePO_4.(H_2O)_2$ crystals, where the iron has 3+ oxidation state, the oxygen in the air oxidize the Fe(II) to Fe(III). Doing the whole experiments under an inert atmosphere may keep the solutions and the spread gels stable and prevent the precipitation, but this is not practice in this synthesis.

Since we did not have a set up for an inert conditions in the laboratory, the we have synthesized $Li_3Fe_2(PO_4)_3$ by using iron nitrate as the iron source. This material can also be used as an anode material for the lithium ion materials. [89] For the synthesis of $Li_3Fe_2(PO_4)_3$ sample, the Li:PA:Fe 60:60:40 mole ratio was used to keep the stoichiometry, see Table 3.7, and abbreviated as LFeP-60:40:60.

$Li_3Fe_2(PO_4)_3$	P123	H_3PO_4	$LiNO_3$	$[Fe(H_2O)_6](NO_3)_2.3H_2O$
60:40:60	1 g	1.200 g	0.719 g	2.810 g

Table 3.7. The amounts of ingredients for the LFeP-60:40:60.

The solution of S-LFeP-60:40:60 was prepared by using the method used for iron in the previous section, see Figure 3.56. While stirring the solution to dissolve all the chemicals, a small amount of precipitation is observed. The precipitate must be removed by centrifugation for the further process. Aging the solution does not produce any other precipitation; the clear solution remains stable for a long time and could be used in later use.

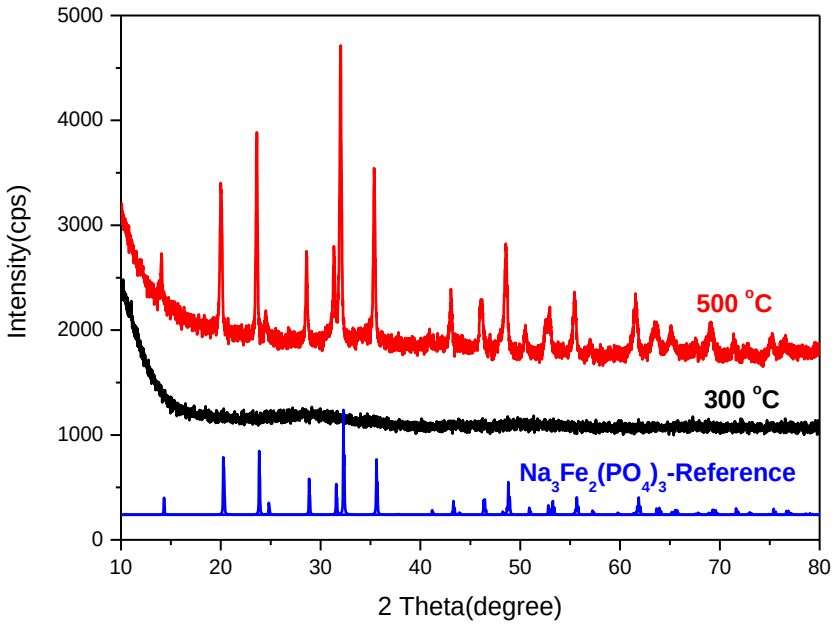

Figure 3.61. High angle XRD patterns of LFeP-60:40:60 sample at 300 and 500 ºC and $Na_3Fe_2(PO_4)_3$ with PDF-card no 00-045-0319.

The clear solutions were spread over the glass slides and calcined at 300 ºC to obtain mesoporous LFeP-60:40:60. XRD patterns were recorded to identify the crystal structure of the samples, annealed at higher temperatures. As shown in Figure 3.61, the LFeP-60:40:60 sample is amorphous at 300 ºC and it becomes crystalline at 500 ºC. The XRD pattern is indexed to $Na_3Fe_2(PO_4)_3$ compound. The detail of the analysis will be provided in later sections.

Using Fe^{3+} source, we also synthesize mesoporous $FePO_4$, which is also an important anode material for lithium ion batteries. In preparing the solutions of $FePO_4$ (abbreviated as S-FeP), again single vial solution preparation was employed; first the surfactant was dissolved in a water and PA solution. Then, the iron nitrate was added to this solution and stirred to obtain homogeneous clear solution. S-FeP is stay stable for a long time and could be used in later use. 60:60 Fe(III):P123 mole ratio is chosen as the optimum mole ratio in the preparation of the solution.

The clear S-FeP-60 was drop-cast coated on glass substrate and calcined to produce $FePO_4$. The samples, calcined at different temperatures, were investigated using XRD technique. Figure 3.62 displays a set XRD patterns of FeP-60 sample, which is

amorphous at 300 ºC, crystalline at 500 ºC and the pattern can be indexed to $FePO_4$ (PDF-card no 00-029-0715).

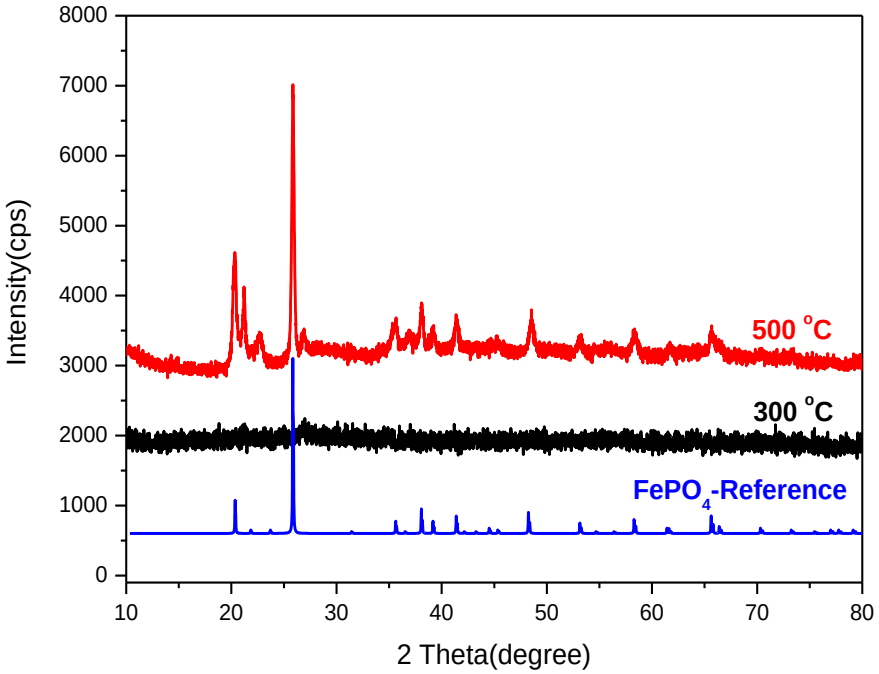

Figure 3.62. High angle XRD patterns of FeP-60 at 300 and 500 ºC, and $FePO_4$ reference, PDF-card no 00-029-0715.

Further, the FeP samples, calcined at both 300 and 500 ºC, were analyzed by ATR-FTIR spectrometer in order to examine the effect of temperature treatment. Figure 3.63 shows the ATR-FTIR spectra that display changes mainly in the phosphate region (1250-500 cm^{-1}). The peaks due to P-O stretching and bending modes are quite broad at 300 ºC, because the sample is amorphous. Moreover, there is an extra small broad peak at around 773 cm^{-1} between the 2 main broad peaks that originates from the $P_2O_7^{4-}$ species, but this peak disappears at 500 ºC. [90] At 500 ºC, the broad peak of the stretching modes of phosphate at around 985 cm^{-1} becomes sharper instead of splitting into many peaks compared to the one calcined at 300 ºC. The other broad peak at around 620 cm^{-1} which corresponds to the bending mode of phosphate splits into 2 peaks, located at 635, and 590 cm^{-1}. Notice also that there is another peak formation at 500 ºC at around 430 cm^{-1}. This peak has been assigned to Fe-O stretching mode. [91]

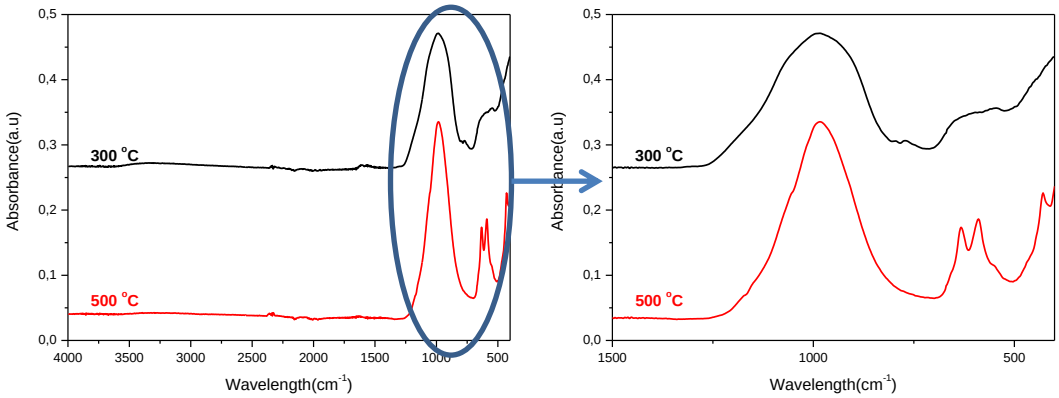

Figure 3.63. ATR-FTIR spectra of LNiP-60 at 300 and 500 ºC.

The SEM images of the FeP-60 samples were collected in order to show the morphology at 300, and 500 ºC. The samples, calcined at 300 ºC have multiple morphologies in various parts of the same sample, see Figure 3.64. In some areas, there are spherical particles, whereas in some part the particles have film like structures. Moreover, with a higher magnification, it is possible to observe the porosity in the samples.

The SEM images of the sample, annealed at 500 ºC (see Figure 3.65) show a mixture of spherical particles and film like structures. There is an extra morphology on the spherical particles which is resulted from higher temperature calcination treatment, where the particles merge into each other and form aggregates.

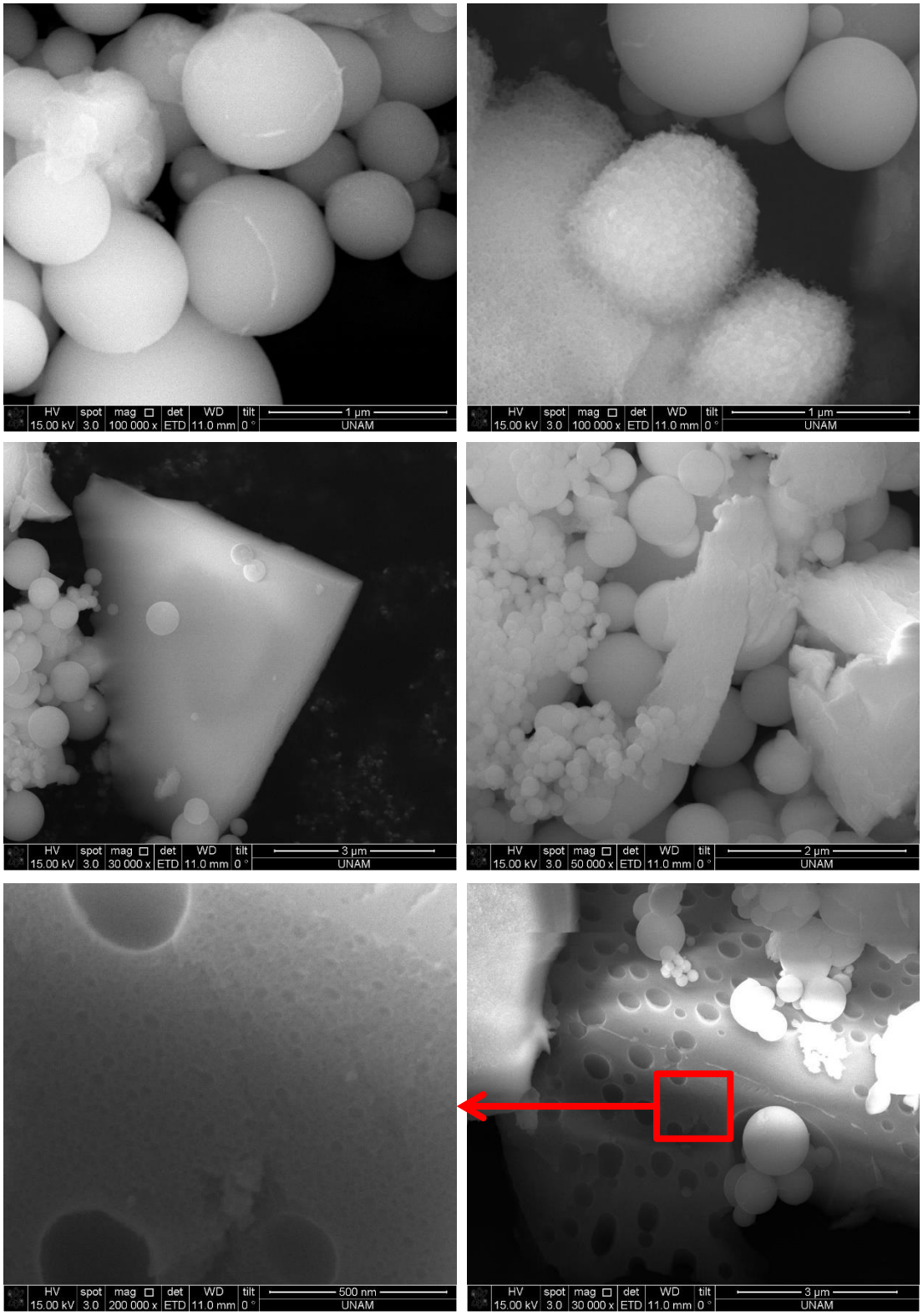

Figure 3.64. SEM images of FeP-60 at 300 ºC with different magnifications.

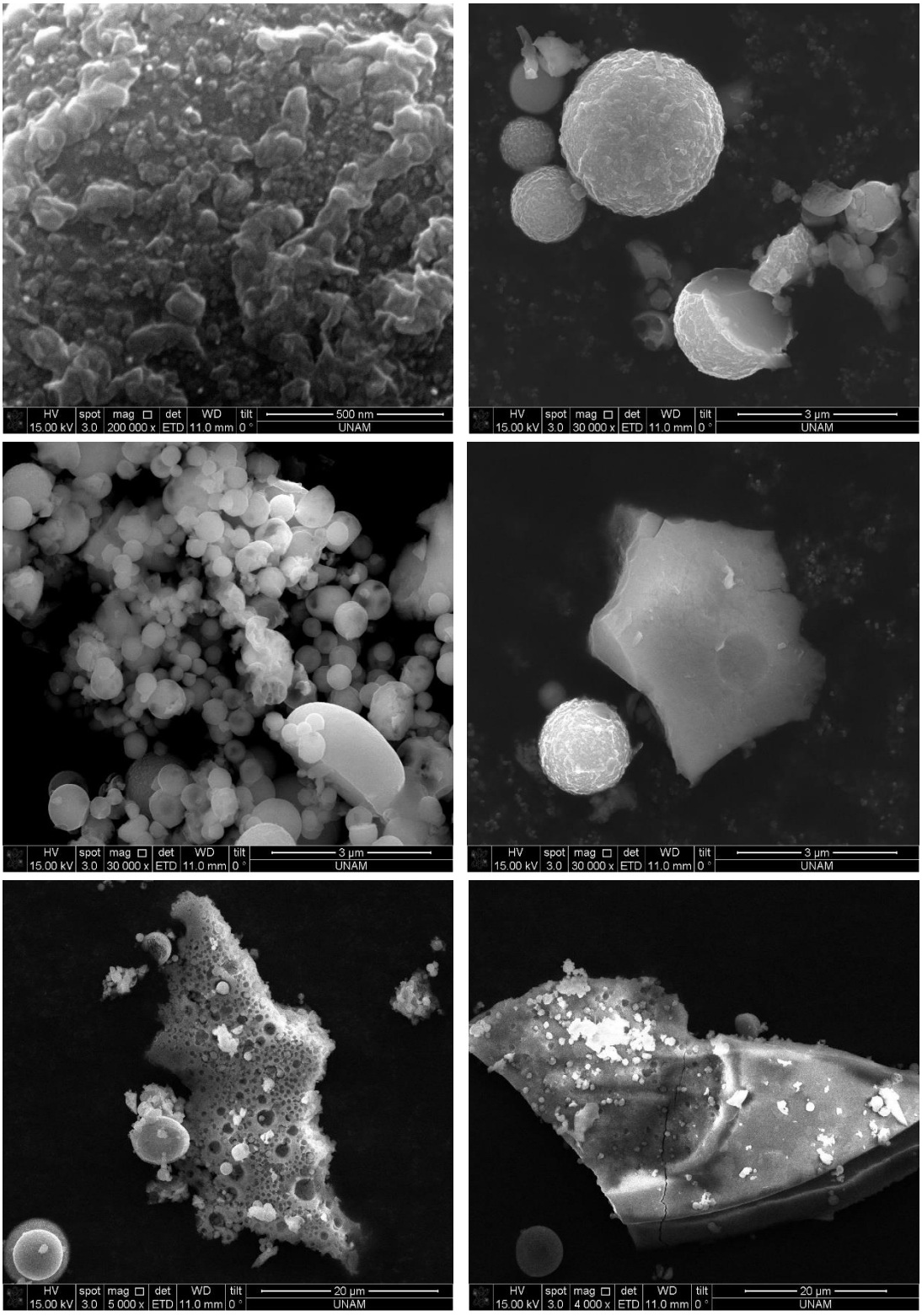

Figure 3.65. SEM images of FeP-60 at 500 ºC with different magnifications.

3.7. Comparison of Lithium Transition Metal Phosphates, LMPs

As discussed in previous sections, for all transition metals, we synthesized the LMP in olivine structure. Here, we will show the comparison of those 4 metals together to see the differences more clearly.

Firstly, the clear solutions of all 4 metal salts and the powders of these samples after calcination are shown in Figure 3.66. The colors of the solution for different metal salts are quite different and also the color of the powders varies from each other and even their own solutions.

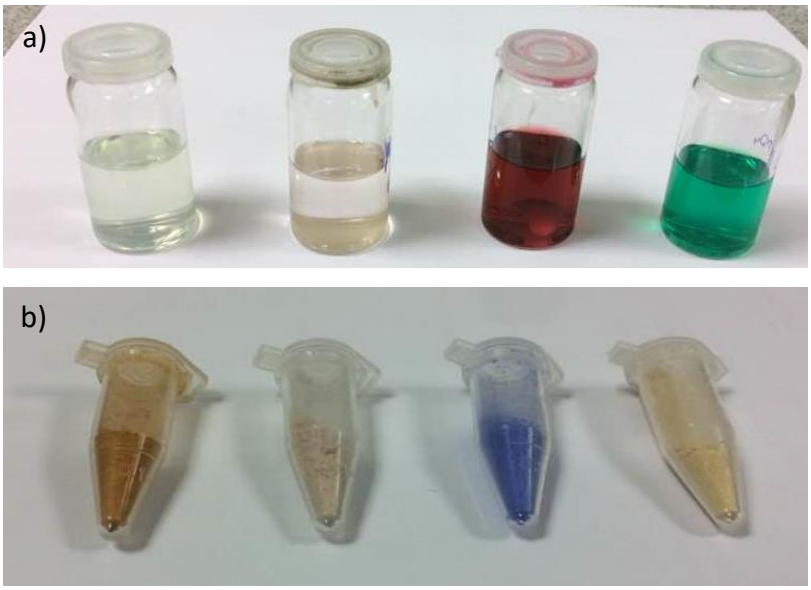

Figure 3.66. Photos of a) solutions, and b) powders of LFeP, LMnP, LCoP, and LNiP from left to right respectively.

The XRD patterns were also compared after calcination treatment at both 300 and 500 ^{o}C. Figure 3.67 shows that at 300 ^{o}C they are all amorphous whereas with increasing temperature to 500 ^{o}C the olivine structure of the samples forms. For the comparison, 60 mole ratio was used as the optimized mole ratio.

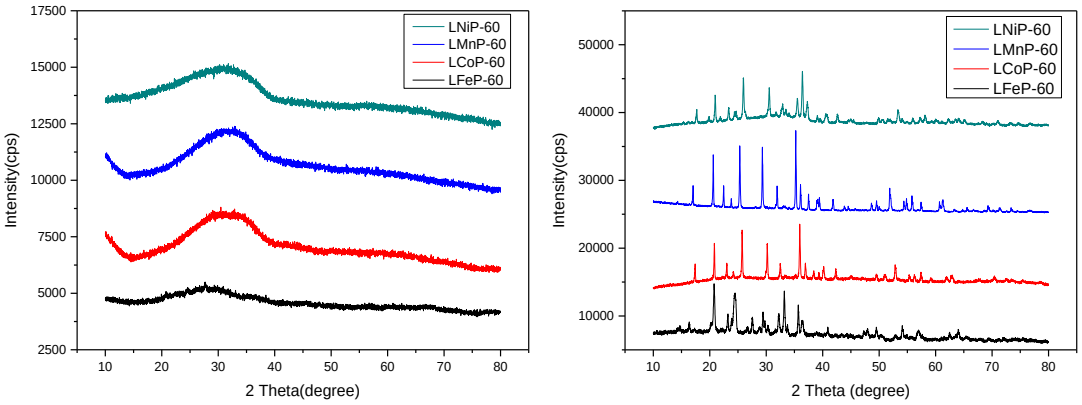

Figure 3.67. High angle XRD patterns of LMPs at (left) 300 ºC, and (right) 500 ºC.

In order to observe the morphological similarity and differences, TEM (for the samples calcined at 300 ºC) and SEM (for the samples calcined at 500 ºC) images were collected. TEM images (see Figures 3.68-69) show that the morphologies of LMPs are quite similar to each other with spherical shape. The size of the particles is the smallest in the iron case whereas the others have a non-uniform size distribution.

SEM images (see Figure 3.70) show how the morphology changes with increasing temperature in all LMPs.

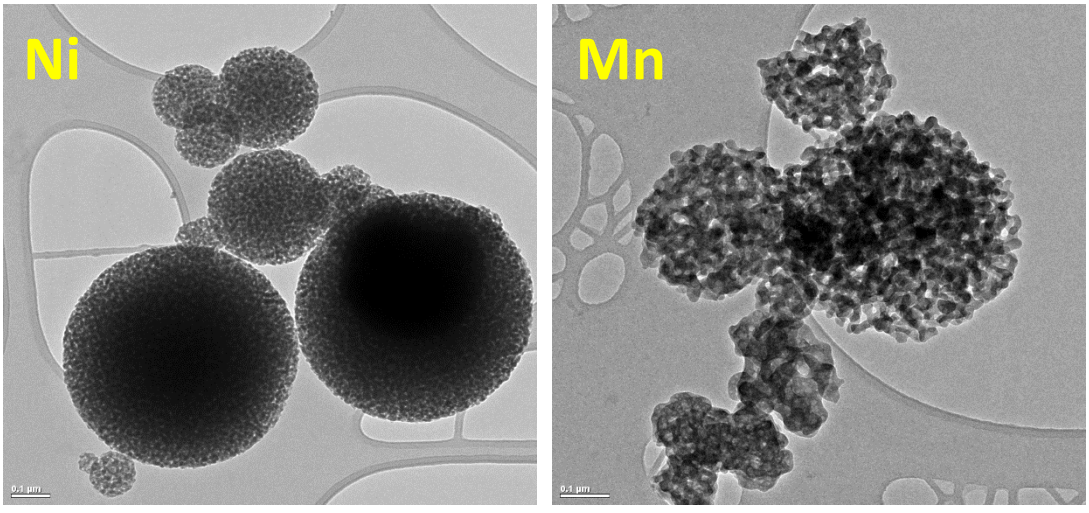

Figure 3.68. TEM images of LMP at 300 ºC with scale bar 0.1 µm

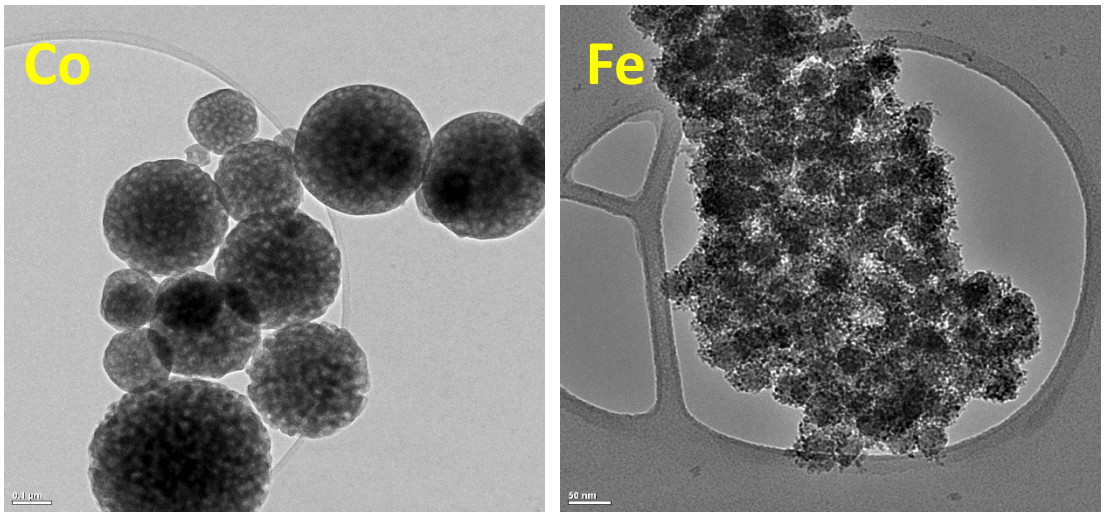

Figure 3.69. TEM images of LMP at 300 ºC with scale bar 0.1 µm and 50 nm respectively.

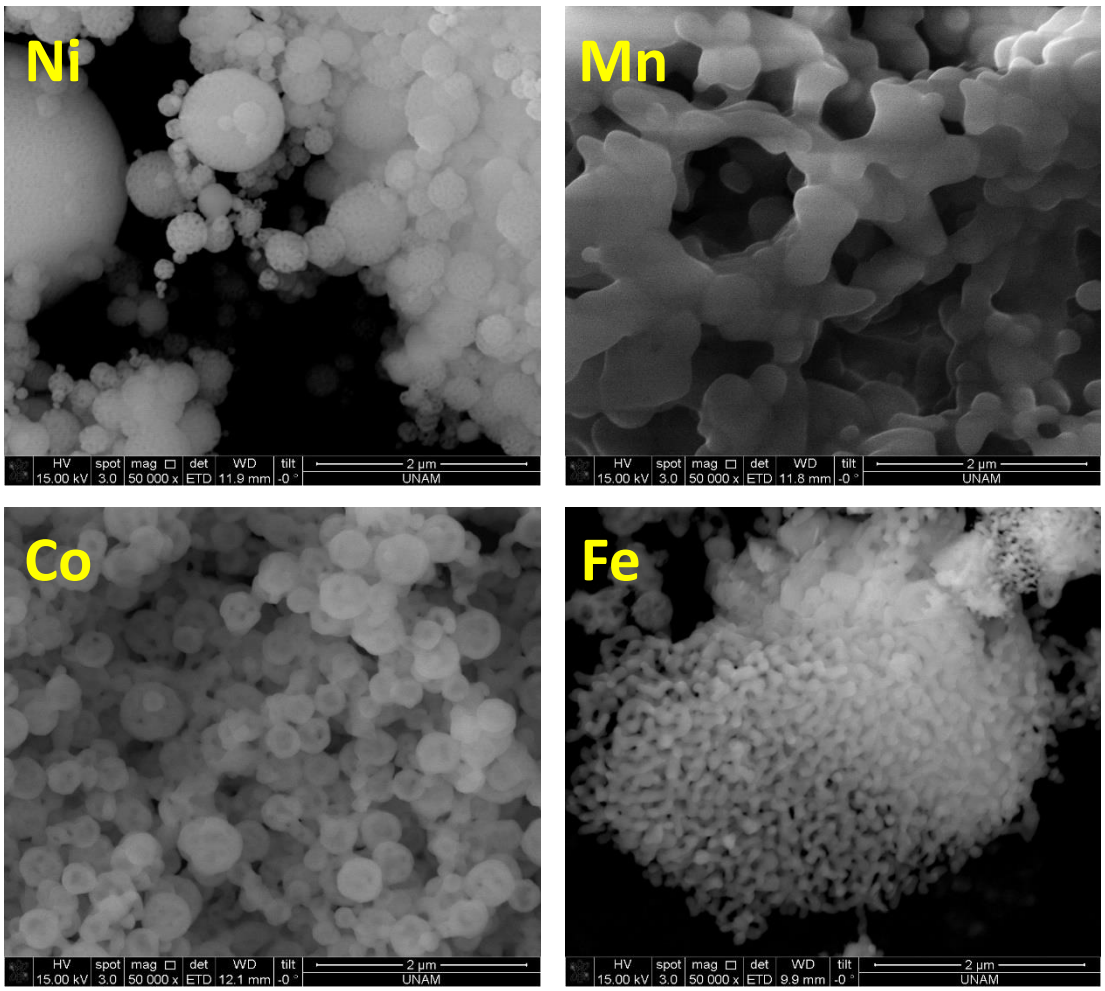

Figure 3.70. SEM images of LMP at 500 ºC with scale bar 2 µm

The N_2 adsorption-desorption isotherms were collected to determine details of the surface and pore parameters in all samples. To compare the transition metal, the isotherms and pore size distributions that are measured from the samples calcined at 300 ^oC were used. As shown in Figure 3.71 (a), the LNiP sample is the best, illustrating a H1hysteresis loop, which means that it has the narrowest and uniform mesopores. Moreover, Figure 3.71 (b) proves that the smallest pores also belong to the LNiP samples. The LCoP has the next narrowest pore width with a H1 hysteresis loop. The other two metals have much larger pore size and their hysteresis is not as structured as the LNiP and LCoP cases.

BET surface areas and average BJH pore sizes of LMPs are compared in Table 3.8 for both 300 and 500 ^oC.

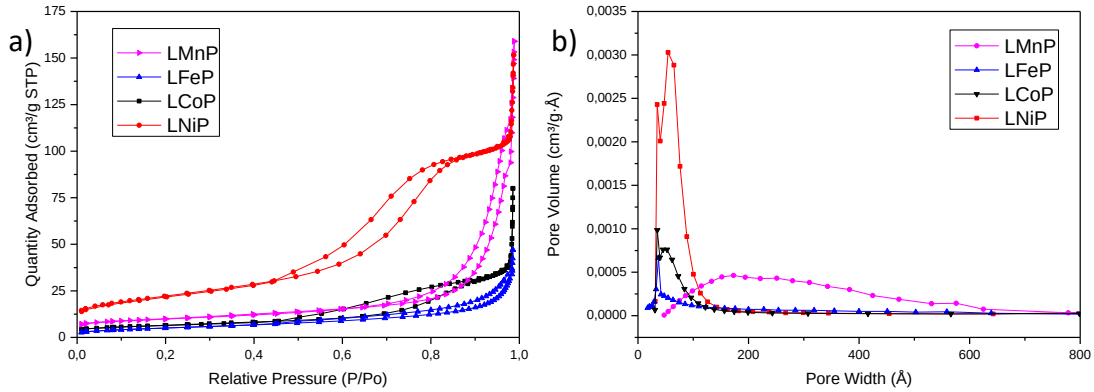

Figure 3.71. a) Linear isotherm plot and b) BJH pore size distribution of LMP for 300 ^oC.

Sample	BET Surface Area (at 300°C) (m^2/g)	BJH Pore Size (at 300°C) (nm)	BET Surface Area (at 500°C) (m^2/g)	BJH Pore Size (at 500°C) (nm)
LNiP	79	8.9	14	42.6
LMnP	40	30.4	2	26.5
LCoP	23	14.8	5	28.1
LFeP	19	14.2	7	36.7

Table 3.8. The BET surface area and the BJH pore size of LMP-60 at 300 and 500 ^oC.

In order to analyze further, K-edge x-ray absorption near edge structure (XANES) analysis for LMP were performed in SESAME (Synchrotron-light for Experimental Science and Applications in the Middle East) facility in Allan, Jordan. Figure 3.72 shows the K-edge XANES spectra of the LMPs. To collect the spectra, pre-edge, and K-edge were measured where the pre-edge shows a 1s→3d transition, K-edge demonstrate a strong 1s→4p transition. [92] The XANES spectra of LCoP (see Figure 3.72 (a)) represent a weak signal for pre-edge at around 7710 eV, a strong signal for the K-edge at around 7718 eV and the strong peak at around 7724 eV, originating from a 1s→continuum transition and the all signals are characteristic for the Co^{2+} oxidation state. [93] Notice that the spectrum of Co_3O_4 is also measured for the purpose of reference data, where the cobalt has 2+ and 3+ oxidation states in Co_3O_4. The 1s→continuum transition of Co_3O_4 is displayed at 7729 eV where the shift is arising from Co^{3+} oxidation state.

Figure 3.72 (b) depicts the K-edge XANES spectra of LNiP and NiO as a reference data. Two spectra of Ni K-edge data are almost the same with each other which indicate that nickel in LNiP is in Ni^{2+} oxidation state. The pre-edge signal is not appeared in the spectra for the nickel case due to the lack of 1s→3d transition.

Figure 3.72 (c) shows the Fe K-edge XANES spectra of LFeP and FeP samples. The pre-edge line is displayed at around 7114 eV due to 1s→3d transition which is stronger for the FeP sample. The 1s→continium transition is observed at around 7140 eV for FeP and at 7132 eV for the LFeP. This similarity expresses that even though the synthesis of LFeP is started from $FeCl_2$ source where the oxidation state of iron is 2+, it is hard to keep iron in the Fe^{2+} oxidation state while preparing the samples.

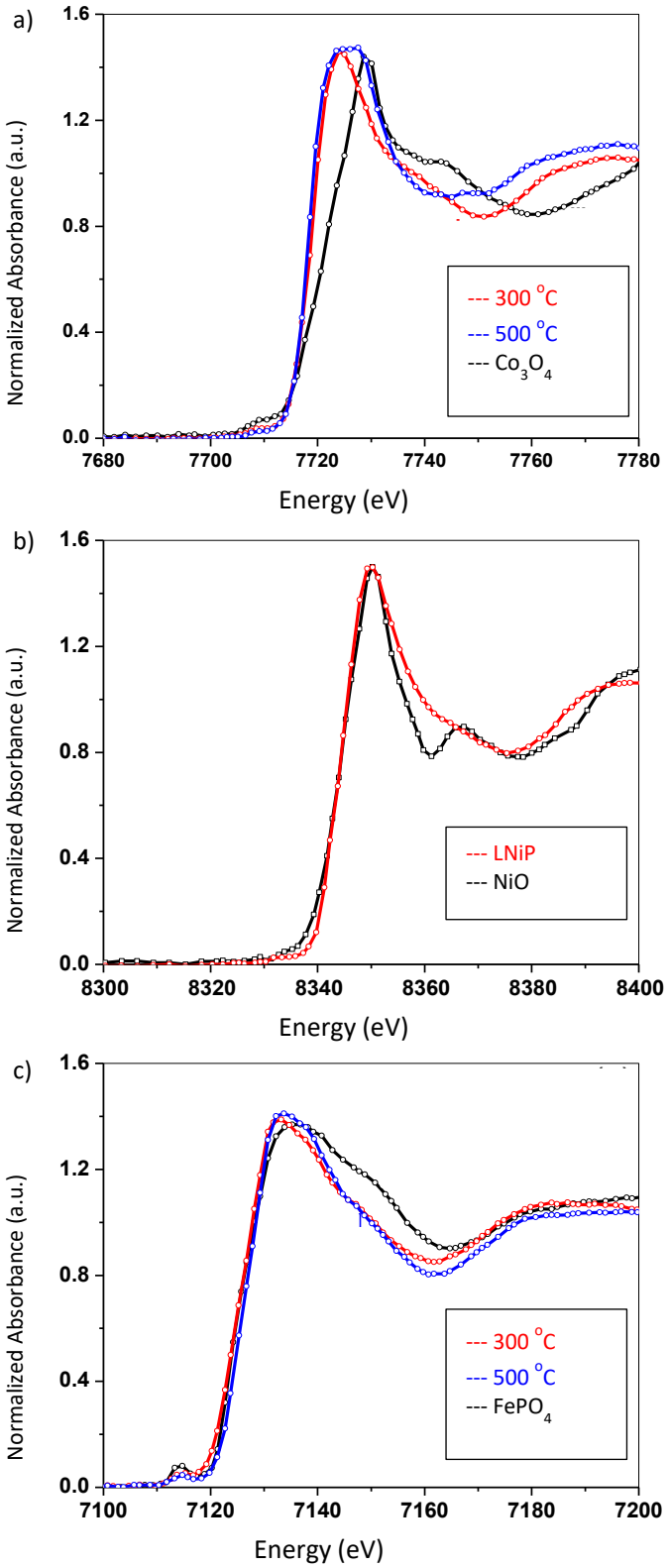

Figure 3.72. K-edge XANES spectra of LMPs: a) 300 and 500 ºC of LCoP and Co_3O_4, b) LNiP and NiO, and c)300 and 500 ºC LFeP and $FePO_4$.

3.8. Lithium to Sodium Exchange in the LMPs

As mentioned before, while preparing the samples, there is an unknown phase formation. For the calcination process, we tried direct calcination and calcination/annealing (2 step process) treatments. Moreover, we also played with the pH of the S-LMPs to overcome those unknown phases. Then, we changed the substrates, where the glass microscope slides were used in calcination process.

The calcination over glass microscope slide at 300 ^{o}C then annealing the same samples at 500 ^{o}C did not work; we could not obtain olivine phases. However, the sample is collected from the glass slides after 300 ^{o}C calcination and then annealed at 500 ^{o}C in an alumina boat, the olivine structure is produced. Notice that calcining the sample directly at 500 ^{o}C on the glass microscope slide did also not form olivine phase whereas changing the glass substrate with Pyrex, FTO, or quartz substrates and calcining the sample both at 300 or 500 ^{o}C by direct calcination or calcination/annealing produces the olivine structures.

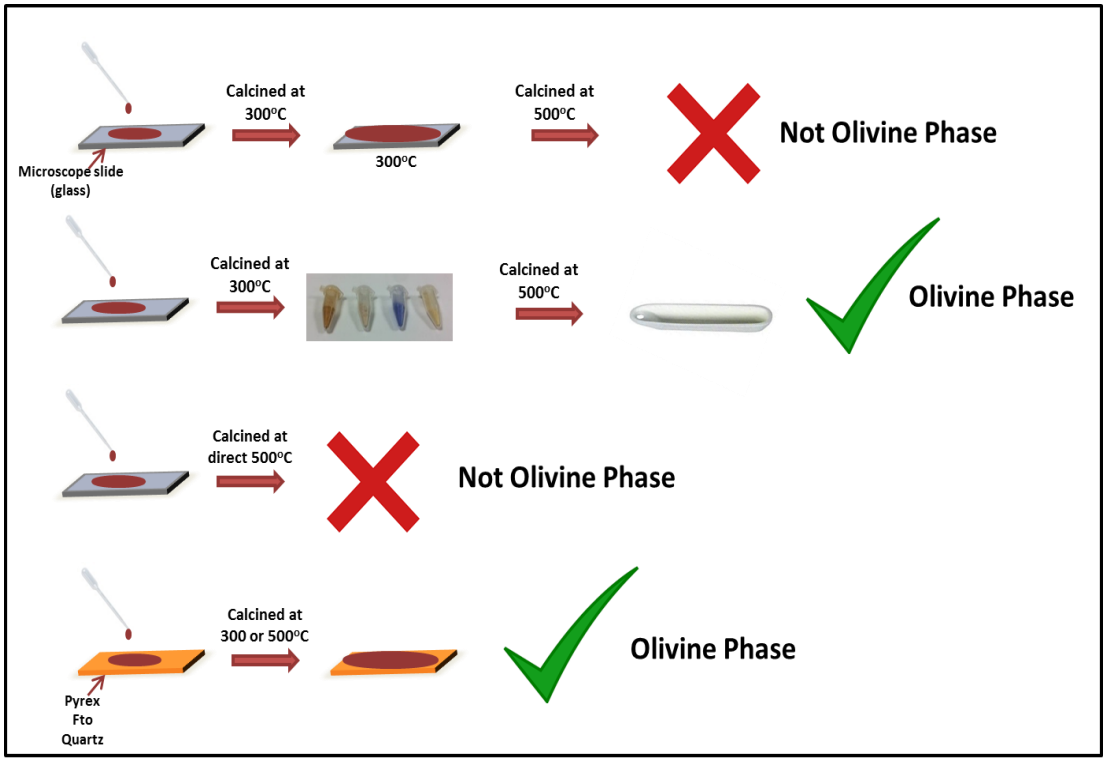

Figure 3.73. Schematic representation of new methodology for calcination steps.

The reason, why at the high temperatures over the microscope slide we could not produce the olivine structures, is that there is a large amount of sodium in the microscope slide and the sodium in the glass and the lithium ion in our materials undergoes an en exchange reaction at high temperatures to form $NaMPO_4$. The percentage of the sodium in the glass is around 16%, which is large enough for a complete exchange reaction.

The reason, why lithium to sodium exchange is not happening on the other substrates which are Pyrex, quartz and FTO is because the sodium amount is very less, even zero in those substrates. Indeed, over the FTO coated glass, there is already high amount of sodium in the glass but since there is a fluorine-doped tin oxide layer on the surface, it prevents the exchange between the sodium ion in glass part of FTO and lithium in our sample, see Figure 3.73.

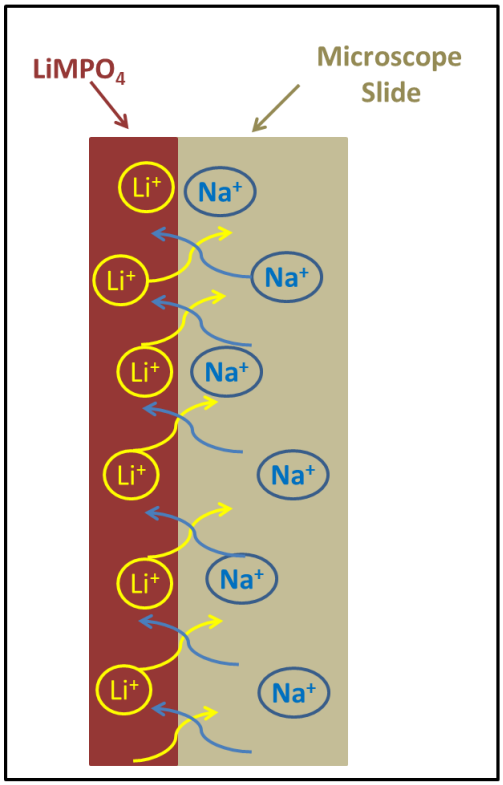

Glass Substrate	Na^+ Percentage
Microscope Slide	16 %
Pyrex	4%
Quartz	0%
FTO	0%

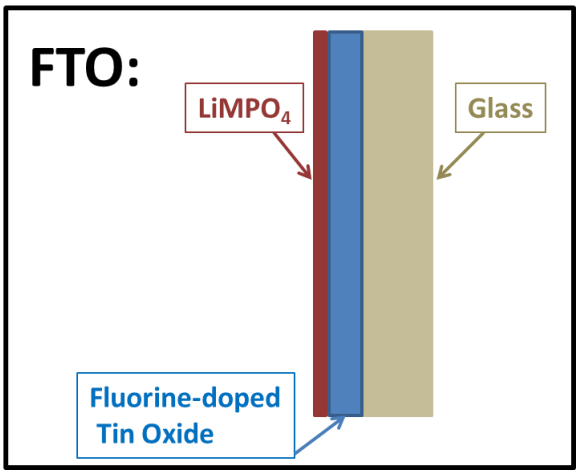

Figure 3.74. (Left) Schematic representation of Li^+-Na^+ exchange, (Right up) the table of sodium percentages in substrates, and (Right down) schematic representation of the FTO.

The exchange reaction is occurring in all cases of LMPs but the exchange reaction was mostly carried in the LCoP samples. Since the colors of the LCoP change with temperatures on different substrates, it is much more helpful to follow the ion exchange process by naked eye. The color of LCoP calcined at 300 ^{o}C on glass is blue-purple, calcined at 500 ^{o}C on glass is grey and calcined at 500 ^{o}C on Pyrex is pink, see Figure 3.75.

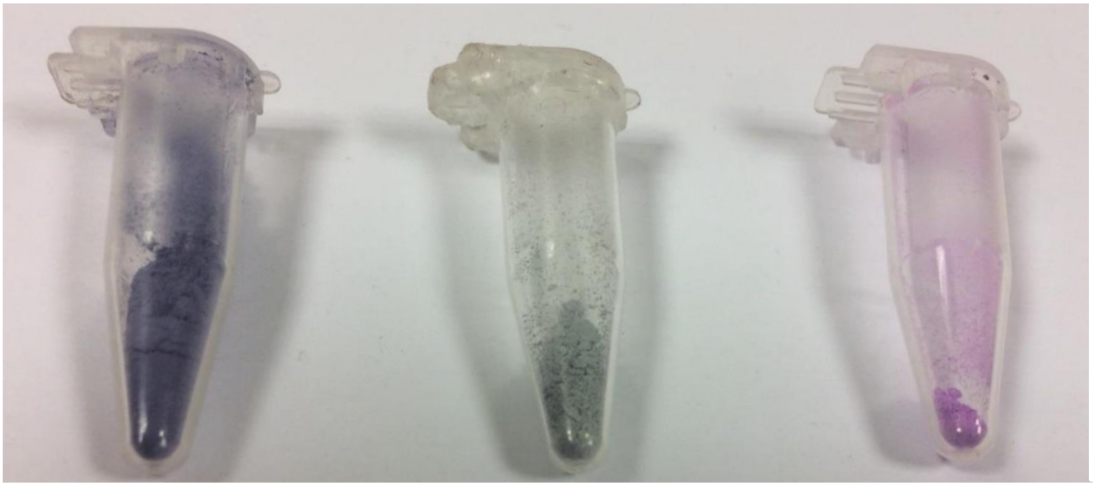

Figure 3.75. Photos of the samples calcined at 300 ^{o}C on glass, at 500 ^{o}C on glass and at 500 ^{o}C on Pyrex respectively.

Furthermore, high angle XRD patterns of the LCoP coated on glass substrates and calcined at different temperatures were recorded. As mentioned before, the sample is amorphous at 300 ^{o}C and it starts to crystalize on glass substrate at 400 ^{o}C, see Figure 3.76 (b). However, the XRD pattern of the sample is very different at 500 ^{o}C on glass. The colors of those crystals are also quite different, see Figure 3.76 (a).

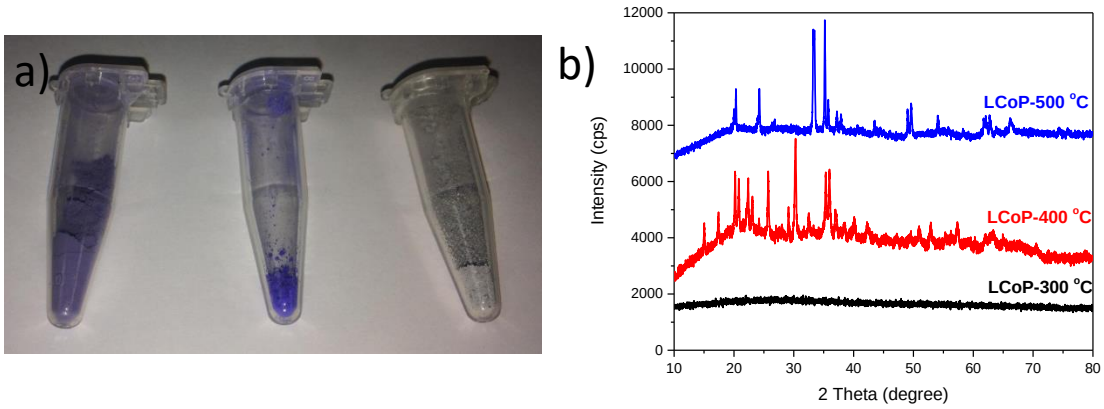

Figure 3.76. a) Photos of LCoP powders prepared at 300, 400, and 500 °C on glass, b) High angle XRD patterns of LCoP calcined at 300, 400, and 500 °C on glass.

The patterns can be indexed to maricite form of $NaCoPO_4$; but the sample calcined at 400 °C is a mixture of two different phases, namely maricite $NaCoPO_4$ and olivine $LiCoPO_4$, see Figure 3.77. The pattern of the sample, calcined at 500 °C on glass matches with the maricite $NaCoPO_4$ reference data, whereas the sample calcined at 500 °C on Pyrex is the pure olivine phase of $LiCoPO_4$, see Figure 3.78.

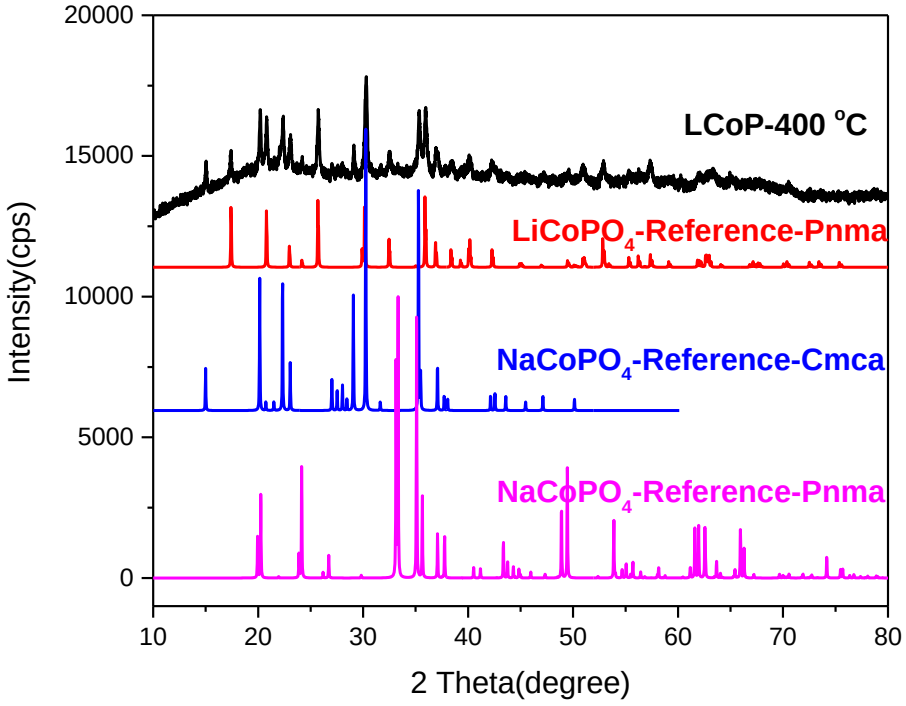

Figure 3.77. High angle XRD patterns of LCoP calcined on glass at 400 °C, $LiCoPO_4$ reference with PDF card no 00-032-0552, $NaCoPO_4$ reference with PDF card no 00-052-0335 for Cmca structure and $NaCoPO_4$ reference with PDF card no 04-009-6022 for Pnma structure.

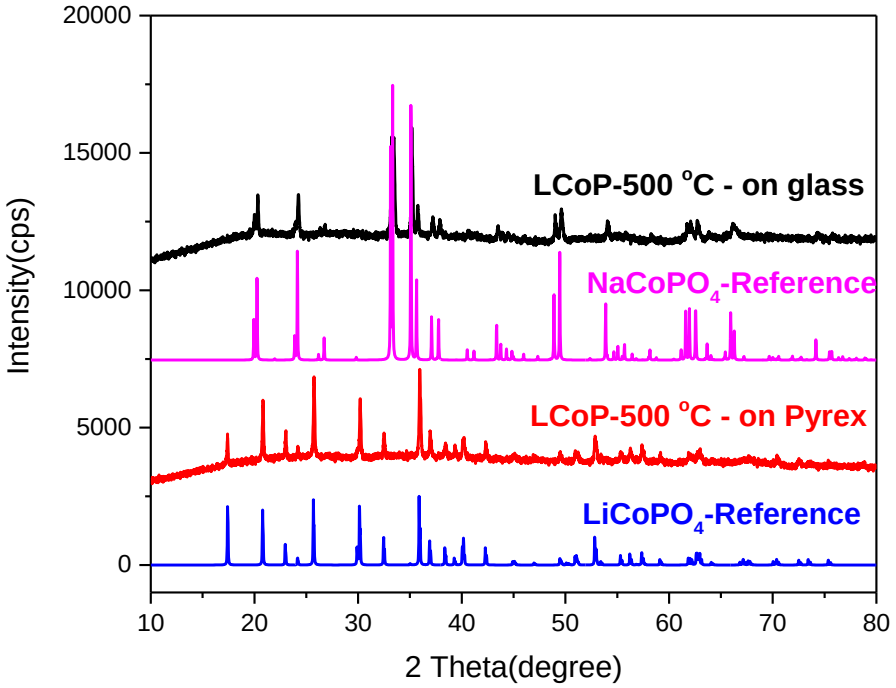

Figure 3.78. High angle XRD patterns of the LCoP calcined at 500 °C on glass and on Pyrex and $LiCoPO_4$ reference with PDF card no 00-032-0552 and $NaCoPO_4$ reference with PDF card no 04-009-6022.

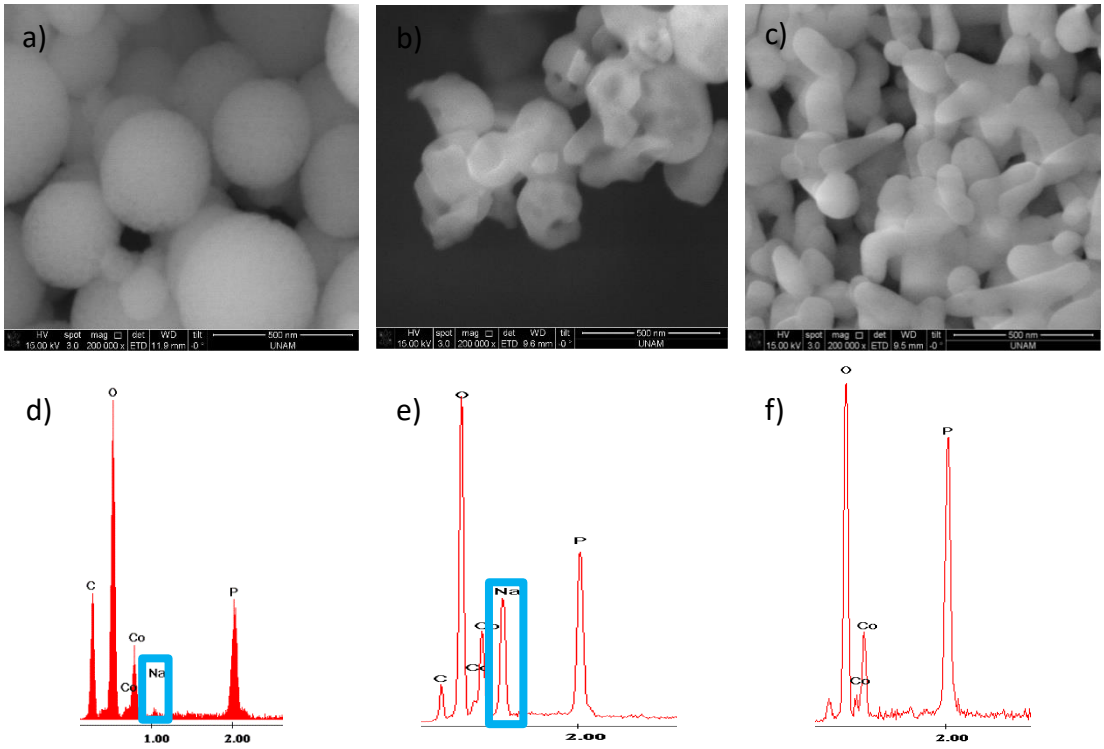

Figure 3.79. SEM images of the LCoP samples, calcined on glass at a) 300 ºC, b) 500 ºC, and c) on Pyrex at 500 ºC; d), e) and f) EDAX data of samples in panels a), b), and c), respectively.

After the exchange of lithium to sodium was proved, the SEM images of those samples were collected to observe the morphology differences, see Figure 3.79. Moreover, we recorded the EDAX data of those samples. The amount of sodium in the sample calcined at 300 ºC on glass is very small, whereas that signal in the EDAX shoots up when the calcination temperature reaches to 500 ºC on glass. Furthermore, when Pyrex is used for the calcination there is no sodium peak in the EDAX data.

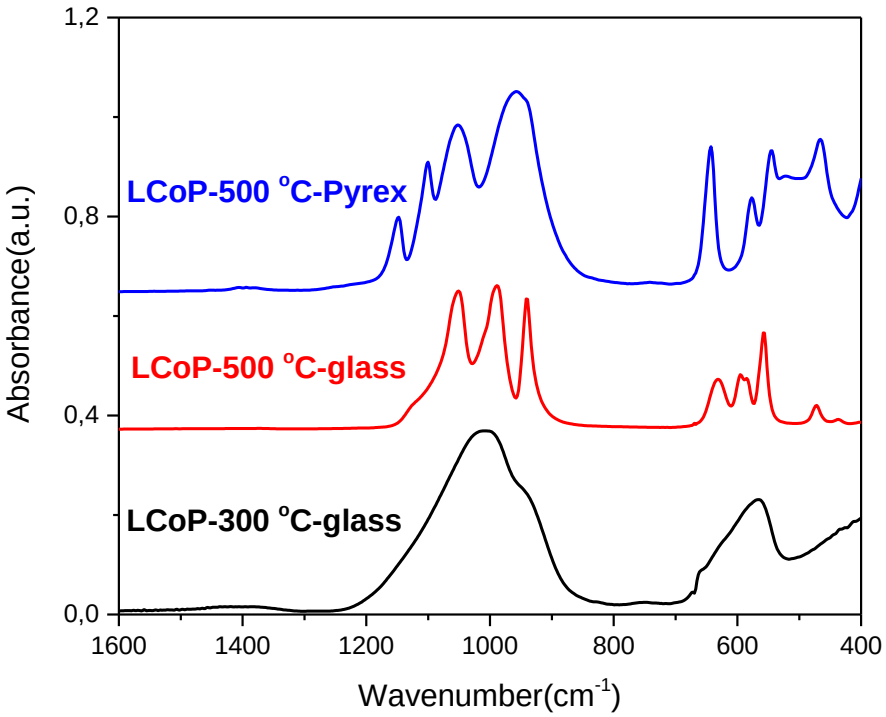

Figure 3.80. ATR-FTIR spectra of LCoP calcined on glass and Pyrex at 300 and 500 °C.

The difference between the samples calcined on different substrate was also analyzed by ATR-FTIR spectrometer. As shown in Figure 3.80, there is quite a difference in the phosphate region between the samples calcined over glass and Pyrex. This is because the structures of the samples are totally different from each other; the symmetry in the structures in terms of PO_4^{3-} ion is quite different. For the further analysis, ICP-MS measurements were performed in Koç University to prove the lithium to sodium exchange over different substrates. Table 3.9 shows that in the samples on glass, the lithium amount is gradually decreasing while the sodium amount is increasing with increasing temperature. However, in the samples, prepared over Pyrex, FTO, and quartz substrates, the lithium and sodium amount almost remains constant. Notice that, the mole ratios are normalized to phosphorous. This is why metal mole ratios seem like more than 1.

Sample-GLASS	Ratio (to PO_4)
LCoP-300°C	$Li_{1.02}Na_{0.38}Co_{1.17}(PO_4)_1$
LCoP-500°C	$Li_{0.05}Na_{1.32}Co_{1.17}(PO_4)_1$
Sample-PYREX	**Ratio (to PO_4)**
LCoP-300°C	$Li_{1.20}Na_{0.20}Co_{1.17}(PO_4)_1$
LCoP-500°C	$Li_{1.12}Na_{0.26}Co_{1.14}(PO_4)_1$
Sample-QUARTZ	**Ratio (to PO_4)**
LCoP-300°C	$Li_{1.13}Na_{0.19}Co_{1.13}(PO_4)_1$
LCoP-500°C	$Li_{1.13}Na_{0.18}Co_{1.13}(PO_4)_1$
Sample-FTO	**Ratio (to PO_4)**
LCoP-300°C	$Li_{1.13}Na_{0.20}Co_{1.13}(PO_4)_1$
LCoP-500°C	$Li_{1.14}Na_{0.18}Co_{1.13}(PO_4)_1$

Table 3.9. ICP-MS results of LCoP on different substrates that are normalized to PO_4 amount.

In order to understand the temperature dependence on the ion exchange, the LCoP samples were calcined various temperatures. Table 3.10 shows the amounts of lithium and sodium with increasing temperature from 100 °C to 500 °C.

Sample-GLASS	Ratio (to PO_4)
LCoP-100 °C	$Li_{1.21}Na_{0.33}Co_{1.17}(PO_4)_1$
LCoP-200 °C	$Li_{1.18}Na_{0.26}Co_{1.18}(PO_4)_1$
LCoP-300 °C	$Li_{1.02}Na_{0.38}Co_{1.17}(PO_4)_1$
LCoP-400 °C	$Li_{0.57}Na_{0.66}Co_{1.17}(PO_4)_1$
LCoP-500 °C	$Li_{0.05}Na_{1.32}Co_{1.17}(PO_4)_1$

Table 3.10. ICP-MS results of LCoP on glass at different temperatures that are normalized to P amount.

To figure out at which temperature the lithium to sodium exchange is starting, the mole ratios of these ions from ICP-MS results were plotted versus temperature. As shown in Figure 3.81, at 100 and 200 ºC there is almost no exchange between lithium and sodium. After 300 ºC, the exchange starts and increases gradually and at 500 ºC it is almost complete. From 300 to 500 ºC, the increase of the exchange rate is linearly dependent on the temperature.

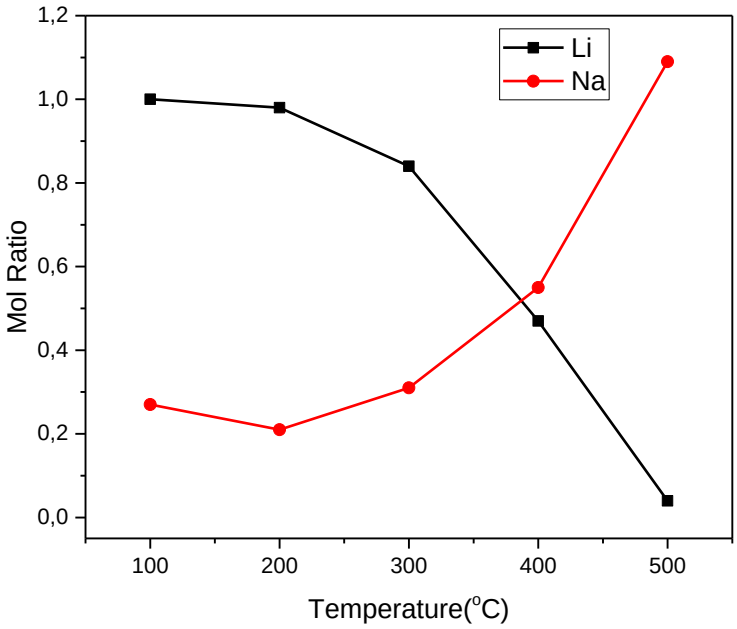

Figure 3.81. The graph of mole ratios of Li and Na versus temperature.

The same exchange process happens in all LMPs on the glass substrate during calcination or annealing at high temperature. By changing the glass by Pyrex, the exchange can be stopped and the target olivine phases can be produced.

Sample-GLASS	Ratio (to PO_4)
Mn60-300 °C-glass	$Li_{0.85}Na_{0.46}Mn_{1.08}(PO_4)_1$
Mn60-500 °C-glass	$Li_{0.02}Na_{1.18}Mn_{1.11}(PO_4)_1$

Sample-PYREX	Ratio (to PO_4)
Mn60-300 °C-pyrex	$Li_{1.11}Na_{0.22}Mn_{1.10}(PO_4)_1$
Mn60-500 °C-pyrex	$Li_{1.09}Na_{0.22}Mn_{1.09}(PO_4)_1$

Sample - GLASS	Ratio (to PO_4)
Ni60-300°C-glass	$Li_{0.98}Na_{0.43}Ni_{1.12}(PO_4)_1$
Ni60-500°C-glass	$Li_{0.09}Na_{1.14}Ni_{1.14}(PO_4)_1$

Sample-PYREX	Ratio (to PO_4)
Ni60-300 °C-pyrex	$Li_{1.16}Na_{0.16}Ni_{1.14}(PO_4)_1$
Ni60-500 °C-pyrex	$Li_{1.10}Na_{0.22}Ni_{1.14}(PO_4)_1$

Sample - GLASS	Ratio(to PO_4)
Fe60-300°C-glass	$Li_{0.71}Na_{0.63}Fe_{1.07}(PO_4)_1$
Fe60-500°C-glass	$Li_{0.05}Na_{1.04}Fe_{0.91}(PO_4)_1$

Sample-PYREX	Ratio(to PO_4)
Fe60-300 °C-pyrex	$Li_{1.04}Na_{0.23}Fe_{1.09}(PO_4)_1$
Fe60-500 °C-pyrex	$Li_1Na_{0.30}Fe_{1.05}(PO_4)_1$

Table 3.11. ICP-MS results for LMnP, LNiP and LFeP samples on both glass and Pyrex substrate at 300 and 500 °C.

Chapter 4

4. Conclusion

The gels and gelation of solutions of a mixture of PA and P123 and also a mixture of lithium salt, transition metal salt (Mn(II), Fe(II)/Fe(III), Co(II) or Ni(II)), PA, and P123 form LLC mesophases in a broad range of inorganic/P123 mole ratios. Mesophases of the gels of PA-P123 are highly ordered at PA/P123 of 10 to 30 mole ratios (PA-P123-10 to PA-P123-30) with a 2D hexagonal mesostructure. Above 30 mole ratio (PA-P123-30 to PA-P123-90), the mesophase changes from 2D hexagonal to a cubic structure with an increasing unit cell parameter by small increments. The mesophases, obtained from solutions of PA-P123 are not ordered in the gel forms even after evaporation of excess water from the media, likely due to the excess water presence in the mesophases. With the addition of inorganic salt species to a PA and P123 mixture, the mesophase becomes ordered and display diffraction line(s) with a low intensity.

The gels can be calcined at 300 ^{o}C to produce mesoporous amorphous lithium metal phosphates (LMPs) in all metal cases. The amorphous LMPs become crystalline after annealing process at higher temperatures, typically 400 to 500 ^{o}C. The crystalline phases of the LMnP and LCoP are in the olivine phase. However, the LNiP requires

a higher pH in the initial solutions to form its olivine phase. The pH in the solution phase can be adjusted by using different percentages of LiH_2PO_4 as a phosphate and lithium precursor. Moreover, the excess lithium (10% or 20%) also enhances formation of the olivine phase of LNiP. These changes improve the formation of the olivine phase but also, it is found that at high temperature synthesis, there is an ion-exchange (Li^+ to Na+) between our LMP samples and glass substrate. This is the main reason why we could not obtain the olivine phases in the nickel system. Because of ion-exchange, the sample calcined at high temperature over a glass slide is assigned to be $Na_4Ni_3(PO_4)_2P_2O_7$ and $NaNiPO_4$.

Except Fe(II), all LMPs formed the olivine phase upon calcination over 400 ^oC. However, iron undergoes oxidation and always produces Fe(III) species during calcination step, no matter if the initial iron precursor is Fe(II) or Fe(III). Even though the synthesis of LFeP begins with Fe(II) salts, keeping Fe(II) stable in the solution and solid phases is very difficult; it can easily form Fe(III) species (such Fe_2O_3 and $Li_3Fe_2(PO_4)_3$, or $Na_3Fe_2(PO_4)_3$ if prepared on glass substrate) upon calcination. Even in the solution phase, to keep iron in 2+ oxidation state, it requires excess acid (HNO_3, HCl or H_2SO_4) or perfect sealing from the air. Since it is very complicated to stabilize the system with Fe(II), the Fe(III) compounds, $FePO_4$ and $Li_3Fe_2(PO_4)_3$ were successfully synthesized. The method is adoptable for the synthesis of Fe(III) compounds.

Moreover, if the calcination of LMPs is carried directly at a high temperature (such as over 500 ^oC) over glass substrates, we found that the Li^+ ions in the LMPs and Na^+ ion in the glass undergo exchange reaction to form NaMPs in the maricite phase. To eliminate the maricite formation of NaMPs, the glass can be replaced with another

substrate such as, Pyrex (low sodium containing glass), quartz, or FTO for high temperature processes. However, normal glass microscope slides can still be used till 300 ^{o}C and for the further calcination alumina ash tray or the other substrates should be utilized.

However, this exchange process can still be used to produce mesoporous maricite form of NaMPs that may not be synthesized though LLC phase, because sodium salts do not form the LLC phases with non-ionic surfactants.

Chapter 5

5. Future Work

5.1. Synthesis of Characterization of Mesoporous $NaCoPO_4$ using Sodium Precursor

As mentioned, after the Li^+ to Na^+ ion exchange from glass slide, $NaCoPO_4$ (NCoP) synthesis was performed accidentally. Instead of ion exchange synthesis, we also tried to synthesize mesoporous NCoP by using $NaNO_3$ as a precursor and keeping the other chemicals same as in the preparation of $LiCoPO_4$. We chose the 60 mole ratio for this preparation as well and the clear solution of NCoP was obtained. The analysis of mesophases part of that sample was skipped for now; it was directly calcined to obtain mesoporous materials at lower temperatures and to characterize the crystals of the desired sample with further calcination.

In the high angle XRD pattern (see Figure 5.1), it is shown that the material is amorphous at 300 ^oC and starts to crystalline at 500 ^oC as other samples. The lines of the crystal structure at 500 ^oC are fitting with two different structure form of $NaCoPO_4$, orthorhombic and hexagonal structures.

The crystal structure of the samples obtained from the ion exchange part is totally pure as orthorhombic phase (see Figure 5.2). The difference between the samples that are synthesized by exchange and normal synthesis is the purity of the structure phases. This may be related with the synthesis conditions that are confirmed on the

glass slides. The detailed experiments will be done later to synthesize both structure as a pure forms.

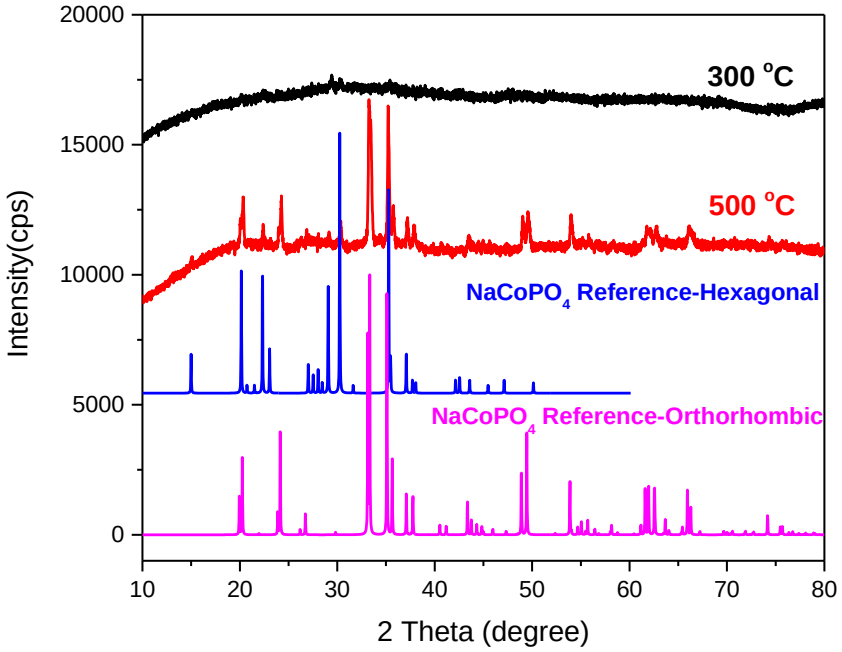

Figure 4.1. High angle XRD pattern of NCoP-60 at 300 and 500 °C and $NaCoPO_4$ reference with PDF card no 00-052-0335 for hexagonal structure and 04-009-6022 for orthorhombic structure.

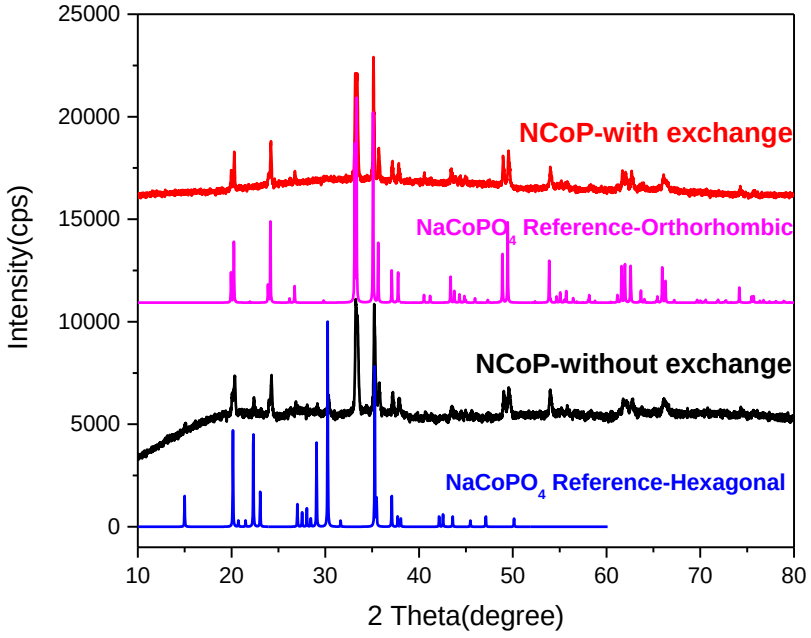

Figure 4.2. High angle XRD pattern of NCoP-60 with and without ion exchange synthesis and $NaCoPO_4$ reference with PDF card no 00-052-0335 for hexagonal structure and 04-009-6022 for orthorhombic structure.

The SEM images of NCoP-60 samples also show that the morphologies of the particles are quite similar to the LCoP-60 samples. There are mostly spherical particles in the sample. However, in same parts there are differences between two samples; in the NCoP sample, film like structures form (see Figure 5.3).

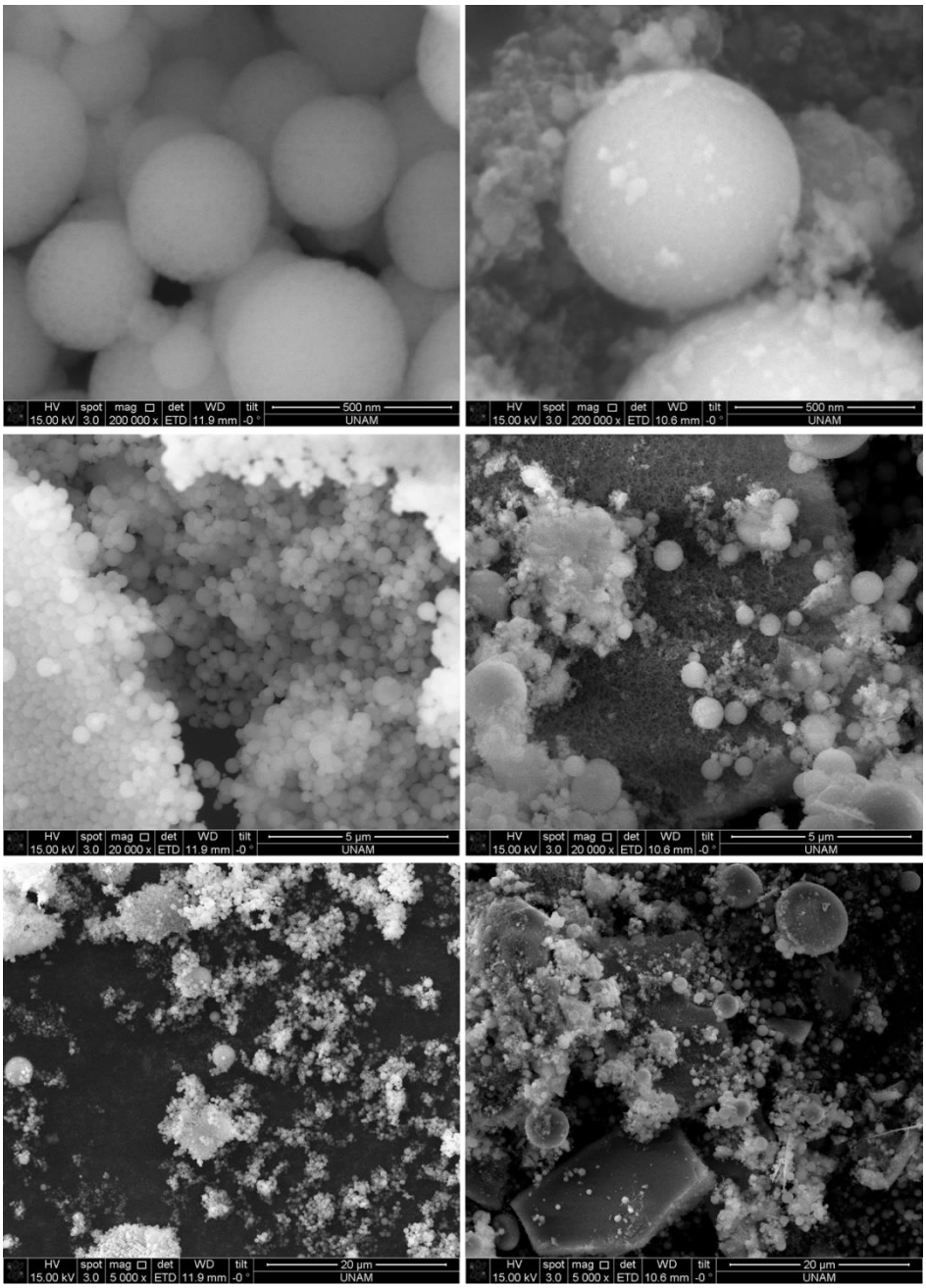

Figure 4.3. SEM images of LCoP-60 (left column) and NCoP-60 (right column) at 300 ºC.

The porosities of the samples are not visible from the SEM images. To understand whether it is mesoporous material or not, we measured the BET surface area of NCoP-60 sample at 300 ^{o}C via N_2-adsorption desorption technique (see Table 5.1). The surface area was quite low compared to the other samples synthesized by Li(I) ion. The detailed experiments will be done to expand the surface area of sample.

Sample (XCoP-60)	BET Surface Area (m^2/g)	BJH Pore Size (Å)	BJH Pore Volume (cm^3/g)
NCoP-60	**7**	**399**	**0.008**

Table 4.1. The BET surface areas, BJH pore sizes, and pore volumes of LMnP-60 at 300 and 500 ^{o}C.

5.2. Synthesis and Characterization of Mesoporous $M_2P_2O_7$ (M=Mn, Co, Ni)

As a future work, lithium-free version of metal pyrophosphates (MPP) has been investigated. The MPPs are widely used as a supercapacitor (SC). Since they have huge ability to store energy, they have been preferred compared to the conventional batteries and drawn attention in the literature [94]–[96]. Moreover, the evaluation of supercapacitor is easier than the normal battery applications; we choose to continue the project in this direction.

Therefore, we did some preliminary investigation to show if our synthesis method is applicable for the synthesis of MPPs. Also note that there is no example of mesoporous MPPs, synthesized using surfactant templating approaches.

Firstly, we have chosen 3 metals (Mn(II), Co(II) and Ni(II)) and prepared their solutions similar to the LMPs without Li(I) salt. As a surfactant, P123 was used and the solutions were prepared in 10 ml of water. 60:60:1 (M(II):PA:P123) mole ratio was chosen as a starting composition, because this composition was the best composition in the LMP system. The MPP-60 notation is used to represent the metal pyrophosphates for $M_2P_2O_7$.

Mesophases of those samples were not analyzed yet; but the calcination of the gel phases directly at 300 and 700 ^{o}C produce an amorphous and crystalline material, respectively. The crystalline phase is the desired materials, $M_2P_2O_7$. The high angle

XRD patterns of all MPPs are shown Figures 5.4-5.6. For each metal, at 300 ^{o}C the material is amorphous and at 700 ^{o}C it is in crystalline form. For the MPPs, the crystallization temperature is quite high.

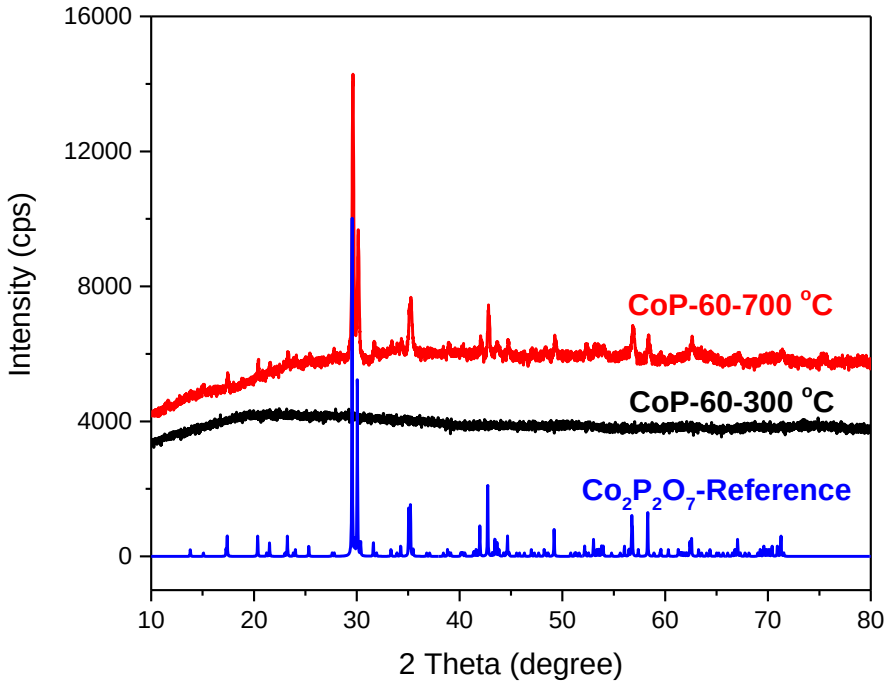

Figure 4.4. High angle XRD pattern of CoPP-60 at 300 and 700 ^{o}C and $Co_2P_2O_7$ reference with PDF card no 00-049-1091.

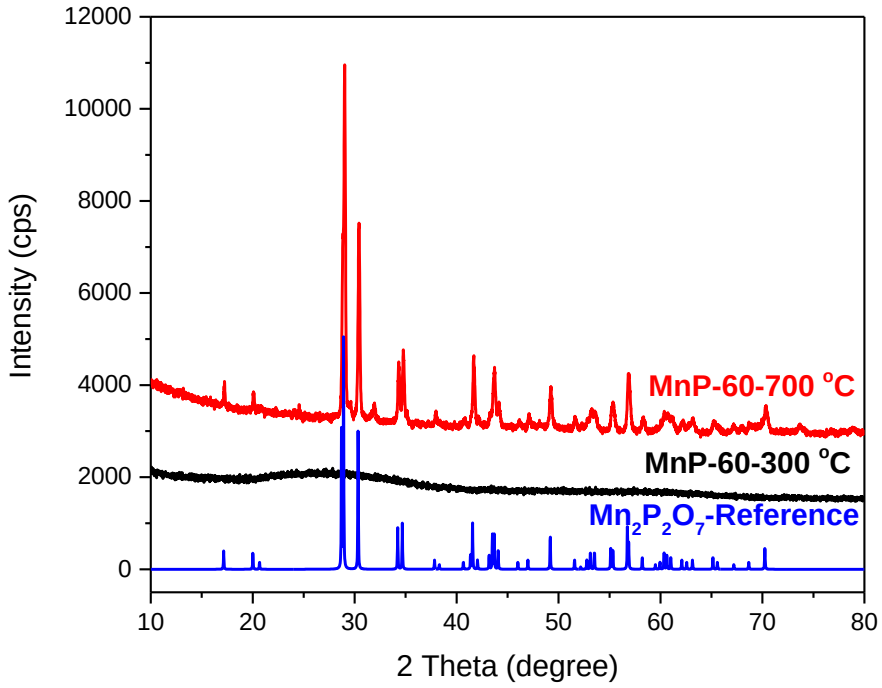

Figure 4.5. High angle XRD pattern of MnP-60 at 300 and 700 ^{o}C and $Mn_2P_2O_7$ reference with PDF card no 00-029-0891.

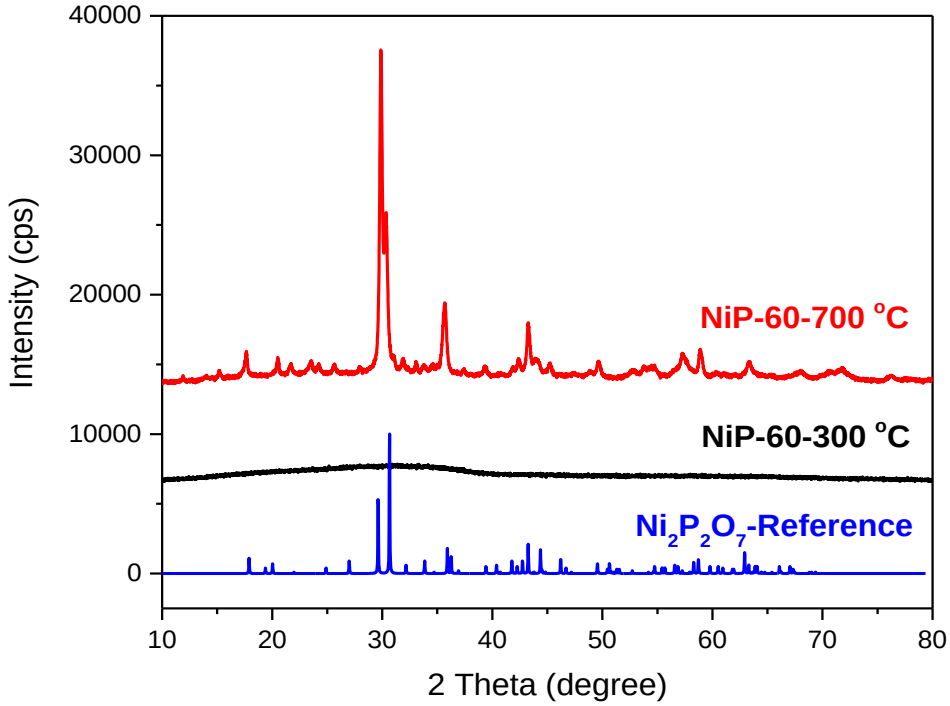

Figure 4.6. High angle XRD pattern of NiPP-60 at 300 and 700 ºC and $Ni_2P_2O_7$ reference with PDF card no 00-049-1082.

After the target materials were obtained as crystalline forms, it is also important to determine if the samples are mesoporous. Therefore, the amorphous phases of MPPs were scraped from the glass substrates and their N_2-adsorption desorption measurements were performed. The detailed characterization was not done yet, the BET surface areas were quite reasonable to conclude that they are mesoporous, see Table 5.2. The BET surface area is very similar to the values of LMPs. To further improve those numbers, optimization of the mole ratios of the inorganic species to surfactant and calcination temperature needs tedious work. Since, our work is the first example on both LMPs and MPPs; more work is needed to establish better synthesis methods on these technologically important materials.

Sample (MPP-60)	BET Surface Area (m^2/g)
NiPP-60	62
CoPP-60	18
MnPP-60	13

Table 4.2. BET surface area of MPP-60 samples at 300 ºC.

As a preview about the morphologies, the SEM images were also collected from the sample calcined at 300 ºC, see Figures 5.7-5.8. The shapes of the particles are spherical with a wide range in size. Since the surface area of NiPP-60 sample is much higher than the others, the pores can be observable for those samples (see Figure 5.7 (left one)). In the CoPP-60 sample, the shapes of the particles are more spherical (see Figure 5.8). However, the pores in the CoPP-60 are not visible in those images; it requires a detailed TEM analysis for the identification pore structure of MPPs.

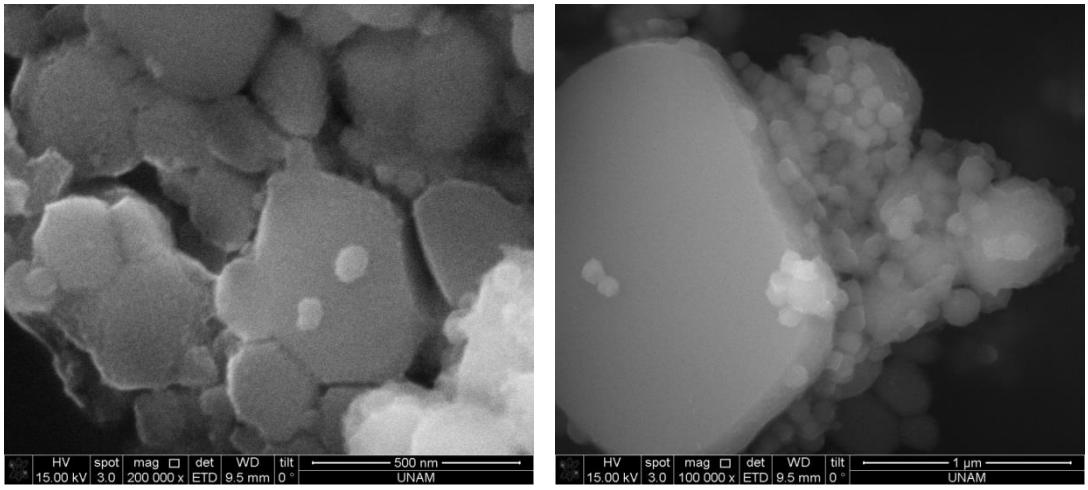

Figure 4.7. SEM images of NiPP-60 sample calcined at 300 ºC.

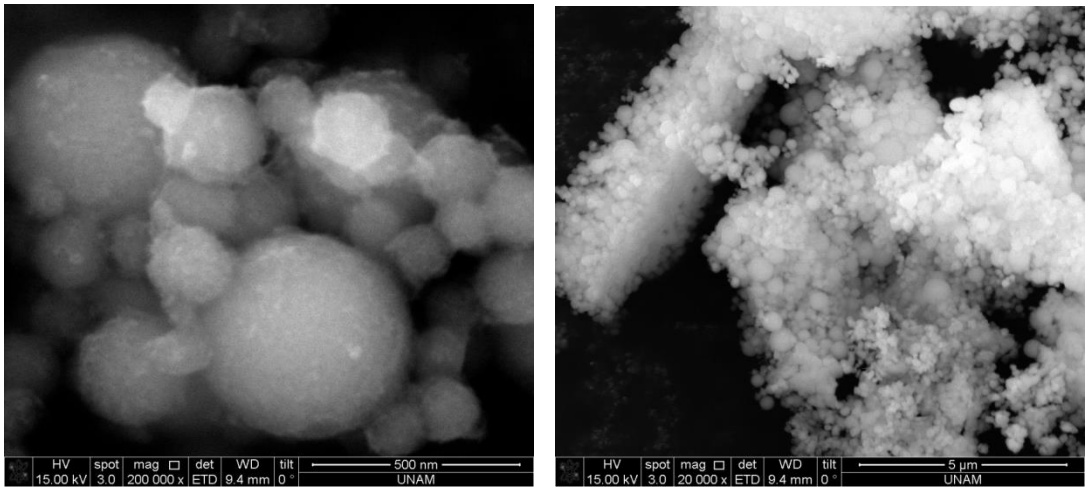

Figure 4.8. SEM images of CoPP-60 sample calcined at 300 ºC.

ATR-FTIR spectra were also collected at those two calcination temperatures, see Figure 5.9. The spectra of the calcined samples at 300 ºC are almost the same in all MPPs. The stretching region of phosphate has two broad peaks, whereas there is one broad peak for the bending region. Moreover, there is an extra peak at around 750 cm^{-1} originated from the $P_2O_7^{4-}$ species [97]. After crystallization of the samples, the peaks become better resolved; the peaks in both stretching and bending regions split into many peaks. A detailed analysis will be performed later with further optimization and characterization.

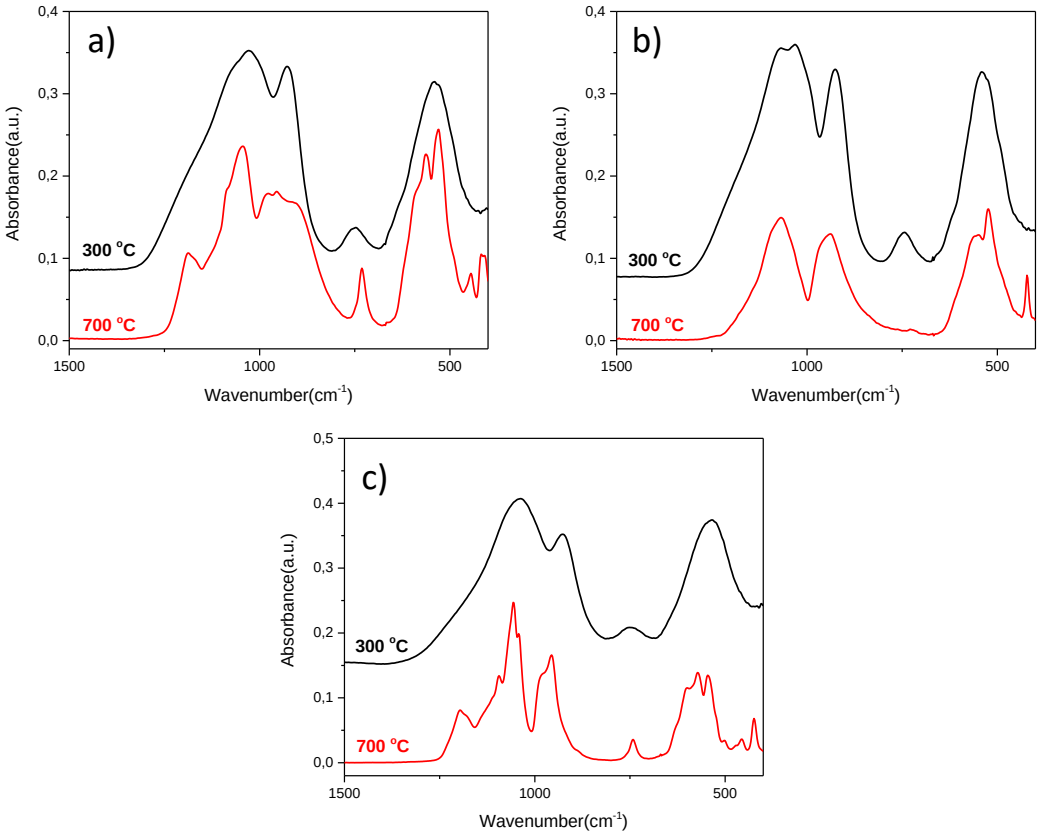

Figure 4.9. ATR-FTIR spectra of MPP-60 samples at 300 and 700 ºC of (a) Co, (b) Mn and (c) Ni.

Bibliography

[1] M. S. Whittingham, “Lithium Batteries and Cathode Materials,” *Chem. Rev.*, vol. 104, no. 10, pp. 4271–4302, 2004.

[2] H. Huang, T. Faulkner, J. Barker, and M. Y. Saidi, “Lithium Metal Phosphates, Power and Automotive Applications,” *J. Power Sources*, vol. 189, no. 1, pp. 748–751, 2009.

[3] J. W.Fergus, “Recent Developments in Cathode Materials for Lithium Ion Batteries,” *J. Power Sources*, vol. 195, no. 4, pp. 939–954, 2010.

[4] A. K. Padhi, “Phospho-olivines as Positive-Electrode Materials for Rechargeable Lithium Batteries,” *J. Electrochem. Soc.*, vol. 144, no. 4, pp. 1188–1194, 1997.

[5] M. S. Whittingham, Y. Song, S. Lutta, P. Y. Zavalij, and N. A. Chernova, “Some Transition Metal (oxy) Phosphates and Vanadium Oxides for Lithium Batteries,” *J. Mater. Chem.*, vol. 15, no. 33, pp. 3362–3379, 2005.

[6] K. Amine, M. Yamachi, and H. Yasudab, “Olivine $LiCoPO_4$ as 4.8 V Electrode Material for Lithium Batteries,” *Electrochem. Solid-State Lett.*, vol. 3, no. 4, p. 178, 1999.

[7] S. Okada *et al.*, “Cathode Properties of Phospho-Olivine $LiMPO_4$ for Lithium Secondary Batteries,” *J. Power Sources*, vol. 97–98, pp. 430–432, 2001.

[8] M. T. Guohua Li, Hideto Azuma, “$LiMnPO_4$ as the Cathode for Lithium Batteries,” *Electrochem. Solid-State Lett.*, vol. 5, no. 6, pp. A135–A137, 2002.

[9] P. Deniard *et al.*, “High Potential Positive Materials for Lithium-Ion Batteries: Transition Metal Phosphates,” *J. Phys. Chem. Solids*, vol. 65, no. 2–3, pp. 229–233, 2004.

[10] S. Y. Chung, J. T. Bloking, and Y. M. Chiang, “Electronically Conductive Phospho-Olivines as Lithium Storage Electrodes,” *Nat. Mater.*, vol. 1, no. 2, pp. 123–128, 2002.

[11] V. Koleva *et al.*, “Precursor-Based Methods for Low-Temperature Synthesis of Defectless $NaMnPO_4$ with an Olivine- and Maricite-Type Structure,” *CrystEngComm*, vol. 15, no. 44, pp. 9080–9089, 2013.

[12] P. Moreau, D. Guyomard, J. Gaubicher, and F. Boucher, “Structure and Stability of Sodium Intercalated Phases in Olivine $FePO_4$,” *Chem. Mater.*, vol. 22, no. 14, pp. 4126–4128, 2010.

[13] D. Dai, M. H. Whangbo, H. J. Koo, X. Rocquefelte, S. Jobic, and A. Villesuzanne, “Analysis of the Spin Exchange Interactions and the Ordered Magnetic Structures of Lithium Transition Metal Phosphates $LiMPO_4$ (M = Mn, Fe, Co, Ni) with the Olivine Structure,” *Inorg. Chem.*, vol. 44, no. 7, pp. 2407–2413, 2005.

[14] M. Avdeev *et al.*, “Magnetic Structures of $NaFePO_4$ Maricite and Triphylite Polymorphs for Sodium-Ion Batteries,” *Inorg. Chem.*, vol. 52, no. 15, pp. 8685–8693, 2013.

[15] M. Minakshi and D. Meyrick, “Reversible Sodiation in Maricite $NaMn_{1/3}Co_{1/3}Ni_{1/3}PO_4$ for Renewable Energy Storage,” *J. Alloys Compd.*, vol. 555, pp. 10–15, 2013.

[16] Y. Lepage and G. Donnay, “The Crystal Structure of The New Mineral Maricite; $NaFePO_4$,” *Can. Mineral.*, vol. 15, pp. 518–521, 1977.

[17] B. Senthilkumar, K. V. Sankar, L. Vasylechko, Y. S. Lee, and R. K. Selvan, “Synthesis and Electrochemical Performances of Maricite-$NaMPO_4$ (M = Ni, Co, Mn) Electrodes for Hybrid Supercapacitors,” *RSC Adv.*, vol. 4, no. 95, pp. 53192–53200, 2014.

[18] S. P. Ong *et al.*, “Voltage, Stability and Diffusion Barrier Differences between Sodium-Ion and Lithium-Ion Intercalation Materials,” *Energy Environ. Sci.*, vol. 4, pp. 3680–3688, 2011.

[19] K. T. Lee, T. N. Ramesh, F. Nan, G. Botton, and L. F. Nazar, “Topochemical Synthesis of Sodium Metal Phosphate Olivines for Sodium-Ion Batteries,”

Chem. Mater., vol. 23, no. 16, pp. 3593–3600, 2011.

[20] J. N. Bridson, S. E. Quinlan, and P. R. Tremaine, "Synthesis and Crystal Structure of Maricite and Sodium Iron(III) Hydroxyphosphate," *Chem. Mater.*, vol. 10, no. 3, pp. 763–768, 1998.

[21] C. Delacourt, P. Poizot, M. Morcrette, J. M. Tarascon, and C. Masquelier, "One-Step Low-Temperature Route for the Preparation of Electrochemically Active $LiMnPO_4$ Powders," *Chem. Mater.*, vol. 16, pp. 93–96, 2004.

[22] J. Yang and J. J. Xu, "Synthesis and characterization of carbon-coated lithium transition metal phosphates $LiMPO_4$ (M=Fe, Mn, Co, Ni) prepared via a nonaqueous Sol-Gel route," *J. Electrochem. Soc.*, vol. 153, no. 4, pp. A716–A723, 2006.

[23] J. Chen, S. Wang, and M. S. Whittingham, "Hydrothermal Synthesis of Cathode Materials," *J. Power Sources*, vol. 174, no. 2, pp. 442–448, 2007.

[24] T. R. Kim *et al.*, "Synthesis of Lithium Manganese Phosphate Nanoparticle and Its Properties," *J. Phys. Chem. Solids*, vol. 68, pp. 1203–1206, 2007.

[25] T. J. Richardson, "Phosphate-Stabilized Lithium Intercalation Compounds," *J. Power Sources*, vol. 119–121, no. 1, pp. 262–265, 2003.

[26] C. M. Julien, A. Ait Salah, F. Gendron, J. F. Morhange, A. Mauger, and C. V. Ramana, "Microstructure of $LiXPO_4$ (X = Ni, Co, Mn) Prepared by Solid State Chemical Reaction," *Scr. Mater.*, vol. 55, no. 12, pp. 1179–1182, 2006.

[27] R. Dominko *et al.*, "Porous Olivine Composites Synthesized by Sol-Gel Technique," *J. Power Sources*, vol. 153, no. 2, pp. 274–280, 2006.

[28] M. Gaberscek, R. Dominko, M. Bele, M. Remskar, D. Hanzel, and J. Jamnik, "Porous, Carbon-dDecorated $LiFePO_4$ Prepared by Sol-Gel Method Based on Citric Acid," *Solid State Ionics*, vol. 176, no. 19–22, pp. 1801–1805, 2005.

[29] C. Delacourt, C. Wurm, L. Laffont, J. B. Leriche, and C. Masquelier, "Electrochemical and Electrical Properties of Nb- and/or C-Containing

$LiFePO_4$ Composites," *Solid State Ionics*, vol. 177, no. 3–4, pp. 333–341, 2006.

[30] L. B. McCusker, F. Liebau, and G. Engelhardt, "Commossion on Colloid and Surface Chemistry Including Catalysis Nomenclature of Structural and Compositional Characteristics of Ordered Microporous and Mesoporous Materials with Inorganic Hosts," *Pure Appl. Chem.*, vol. 73, no. 2, pp. 381–394, 2001.

[31] W. Li and D. Zhao, "An Overview of the Synthesis of Ordered Mesoporous Materials," *Chem. Commun.*, vol. 49, no. 10, pp. 943–946, 2013.

[32] A. Sayari, "Catalysis by Crystalline Mesoporous Molecular Sieves," *Chem. Mater.*, vol. 8, no. 8, pp. 1840–1852, 1996.

[33] G. Øye *et al.*, "Synthesis, Functionalisation and Characterisation of Mesoporous Materials and Sol-Gel Glasses for Applications in Catalysis, Adsorption and Photonics," *Adv. Colloid Interface Sci.*, vol. 123–126, pp. 17–32, 2006.

[34] F. Schüth, "Non-Siliceous Mesostructured and Mesoporous Materials," *Chem. Mater.*, vol. 13, no. 10, pp. 3184–3195, 2001.

[35] S. Wang, "Ordered Mesoporous Materials for Drug Delivery," *Microporous Mesoporous Mater.*, vol. 117, no. 1–2, pp. 1–9, 2009.

[36] Y. Wan and D. Zhao, "On the Controllable Soft-Templating Approach to Mesoporous Silicates," *Chem. Rev.*, vol. 107, no. 7, pp. 2821–2860, 2007.

[37] J. S. Beck *et al.*, "A New Family of Mesoporous Molecular Sieves Prepared with Liquid Crystal Templates," *J. Am. Chem. Soc.*, vol. 114, no. 27, pp. 10834–10843, 1992.

[38] W. J. R. C. T. Kresge, M. E. Leonowicz and J. C. V. & J. S. Beckt, "Ordered Mesoporous Molecular Sieves Synthesized by a Liquid Crystal Template Mechanism," *Nature*, vol. 359, pp. 710–712, 1992.

[39] S. Inagaki, Y. Fukushima, and K. Kuroda, “Synthesis of Highly Ordered Mesoporous Materials from a Layered Polysilicate,” *J. Chem. Soc. Chem. Commun.*, pp. 680–682, 1993.

[40] K. C. Yanagisawa Tsuneo, Shimizu Toshio, Kuroda Kazuyuki, “The Preparation of Alkyltriinethylaininonium–Kaneinite Complexes and Their Conversion to Microporous Materials,” *Chem. Soc. Japan*, vol. 63, no. 4, pp. 988–992, 1990.

[41] C. Y. Chen, S. Q. Xiao, and M. E. Davis, “Studies on Ordered Mesoporous Materials III. Comparison of MCM-41 to Mesoporous Materials Derived from Kanemite,” *Microporous Mater.*, vol. 4, no. 1, pp. 1–20, 1995.

[42] Z. Yuan and W. Zhou, “A Novel Morphology of Mesoporous Molecular Sieve MCM-41,” *Chem. Phys. Lett.*, vol. 333, no. 6, pp. 427–431, 2001.

[43] E. Leontidis, “Hofmeister Anion Effects on Surfactant Self-Assembly and the Formation of Mesoporous Solids,” *Curr. Opin. Colloid Interface Sci.*, vol. 7, no. 1–2, pp. 81–91, 2002.

[44] H. P. Lin and C. Y. Mou, “Structural and Morphological Control of Cationic Surfactant-Templated Mesoporous Silica,” *Acc. Chem. Res.*, vol. 35, no. 11, pp. 927–935, 2002.

[45] A. S. Poyraz and Ö. Dag, “Role of Organic and Inorganic Additives on the Assembly of CTAB-P123 and the Morphology of Mesoporous Silica Particles,” *J. Phys. Chem. C*, vol. 113, no. 43, pp. 18596–18607, 2009.

[46] D. Gu and F. Schüth, “Synthesis of Non-Siliceous Mesoporous Oxides,” *Chem. Soc. Rev.*, vol. 43, no. 1, pp. 313–344, 2014.

[47] J. Y. J. D.M. Antonelli, “Synthesis of Hexagonally Packed Mesoporous TiO, by a Modified Sol-Gel Method,” *Angw. Chem. lnr. Ed. Engl.*, vol. 34, no. 18, pp. 2014–2017, 1995.

[48] Y. Ren, Z. Ma, and P. G. Bruce, “Ordered Mesoporous Metal Oxides: Synthesis and Applications,” *Chem. Soc. Rev.*, vol. 41, no. 14, pp. 4909–4927,

2012.

[49] K. L. Turner, S. A. Miller, P. G. Hartwell, N. C. Macdonald, and S. H. Strogatz, “Generalized Syntheses of Large-Pore Mesoporous Metal Oxidies with Semicrystalline Frameworks,” *Nature*, vol. 396, no. November, pp. 149–152, 1998.

[50] Y. Yamauchi and K. Kuroda, “Rational Design of Mesoporous Metals and Related Nanomaterials by a Soft-Template Approach,” *Chem. - An Asian J.*, vol. 3, no. 4, pp. 664–676, 2008.

[51] W. C. Li, A. H. Lu, C. Weidenthaler, and F. Schüth, “Hard-Templating Pathway to Create Mesoporous Magnesium Oxide,” *Chem. Mater.*, vol. 16, no. 26, pp. 5676–5681, 2004.

[52] C. Avci *et al.*, “Molten Salt Assisted Self Assembly (MASA): Synthesis of Mesoporous Metal Titanate ($CoTiO_3$, $MnTiO_3$, and $Li_4Ti_5O_{12}$) Thin Films and Monoliths,” *Chem. Mater.*, vol. 26, no. 20, pp. 6050–6057, 2014.

[53] G. Saat, F. M. Balci, E. P. Alsaç, F. Karadas, and Ö. Dag, “Molten Salt Assisted Self-Assembly: Synthesis of Mesoporous $LiCoO_2$ and $LiMn_2O_4$ Thin Films and Investigation of Electrocatalytic Water Oxidation Performance of Lithium Cobaltate,” *Small*, vol. 14, no. 1, pp. 1–11, 2018.

[54] R. Ryoo, S. H. Joo, and S. Jun, “Synthesis of Highly Ordered Carbon Molecular Sieves via Template-Mediated Structural Transformation,” *J. Phys. Chem. B*, vol. 103, no. 37, pp. 7743–7746, 1999.

[55] J. Jang and J. Bae, “Fabrication of Mesoporous Polymer Using Soft Template Method,” *Chem. Commun.*, vol. 1, no. 9, pp. 1200–1202, 2005.

[56] C. J. Brinker, Y. Lu, A. Sellinger, and H. Fan, “Evaporation-Induced Self-Assembly: Nanostructures Made Easy,” *Adv. Mater.*, vol. 11, no. 7, pp. 579–585, 1999.

[57] A. Dominguez, A. Fernandez, N. Gonzalez, E. Iglesias, and L. Montenegro, “Determination of Critical Micelle Concentration of Some Surfactants by

Three Techniques," *J. Chem. Educ.*, vol. 74, no. 10, p. 1227, 2009.

[58] T. Brezesinski, M. Groenewolt, A. Gibaud, N. Pinna, M. Antonietti, and B. M. Smarsly, "Evaporation-Induced Self-Assembly (EISA) at Its Limit: Ultrathin, Crystalline Patterns by Templating of Micellar Monolayers," *Adv. Mater.*, vol. 18, no. 17, pp. 2260–2263, 2006.

[59] D. Grosso *et al.*, "Periodically Ordered Nanoscale Islands and Mesoporous Films Composed of Nanocrystalline Multimetallic Oxides," *Nat. Mater.*, vol. 3, pp. 787–792, 2004.

[60] D. Grosso, C. Boissière, L. Nicole, and C. Sanchez, "Preparation, Treatment and Characterisation of Nanocrystalline Mesoporous Ordered Layers," *J. Sol-Gel Sci. Technol.*, vol. 40, no. 2–3, pp. 141–154, 2006.

[61] F. Jiao, A. Harrison, J. C. Jumas, A. V. Chadwick, W. Kockelmann, and P. G. Bruce, "Ordered Mesoporous Fe_2O_3 with Crystalline Walls," *J. Am. Chem. Soc.*, vol. 128, no. 16, pp. 5468–5474, 2006.

[62] L. Ye *et al.*, "Crystalline Three-Dimensional Cubic Mesoporous Niobium Oxide," *CrystEngComm*, vol. 12, pp. 344–347, 2010.

[63] C. Karakaya, Y. Türker, C. Albayrak, and Ö. Dag, "Assembly of Molten Transition Metal Salt-Surfactant in a Confined Space for the Synthesis of Mesoporous Metal Oxide-Rich Metal Oxide-Silica Thin Films," *Chem. Mater.*, vol. 23, no. 12, pp. 3062–3071, 2011.

[64] Y. Türker, C. Karakaya, and Ö. Dag, "Fabrication of Mesoporous Metal Chalcogenide Nanoflake Silica Thin Films and Spongy Mesoporous CdS and CdSe," *Chem. - A Eur. J.*, vol. 18, no. 12, pp. 3695–3705, 2012.

[65] C. Karakaya, Y. Türker, and Ö. Dag, "Molten-Salt-Assisted Self-Assembly (MASA)-Synthesis of Mesoporous Metal Titanate-Titania, Metal Sulfide-Titania, and Metal Selenide-Titania Thin Films," *Adv. Funct. Mater.*, vol. 23, no. 32, pp. 4002–4010, 2013.

[66] J. Prost and P. G. Gennes, *The Physics of Liquid Crystals*. 1993.

[67] F. Reinitzer, “Beitr ge zur Kenntniss des Gholesterins,” *Monatshefte für Chemie*, vol. 9, no. 1, pp. 421–441, 1888.

[68] G. Vertogen and W. H. de Jeu, *Thermotropic Liquid Crystals, Fundamental*. 1988.

[69] N. K. Raman, M. T. Anderson, and C. J. Brinker, “Template-Based Approaches to the Preparation of Amorphous, Nanoporous Silicas,” *Chem. Mater.*, vol. 8, no. 8, pp. 1682–1701, 1996.

[70] G. S. Attard, J. C. Glyde, and C. G. Göltner, “Liquid-Crystalline Phases as Templates for the Synthesis of Mesoporous Silica,” *Nature*, vol. 378, pp. 366–368, 1995.

[71] O. Celik and O. Dag, “A New Lyotropic Liquid-Crystalline System: Oligo(Etylene Oxide) Surfactants with Transition Metal Complexes,” *Angew. Chem. Int. Ed.*, vol. 40, no. 20, pp. 3799–3803, 2001.

[72] Ö. Dag, S. Alayoğlu, C. Tura, and Ö. Çelik, “Lyotropic Liquid-Crystalline Phase of Oligo(Ethylene Oxide) Surfactant/Transition Metal Salt and the Synthesis of Mesostructured Cadmium Sulfide,” *Chem. Mater.*, vol. 15, no. 14, pp. 2711–2717, 2003.

[73] Ö. Dag, S. Alayoğlu, and I. Uysal, “Effects of Ions on the Liquid Crystalline Mesophase of Transition-Metal Salt: Surfactant (C_nEO_m),” *J. Phys. Chem. B*, vol. 108, no. 24, pp. 8439–8446, 2004.

[74] A. Faik Demirörs, B. E. Eser, and Ö. Dag, “Liquid Crystalline Mesophases of Pluronics (L64, P65, and P123) and Transition Metal Nitrate Salts ($[M(H_2O)_6](NO_3)_2$),” *Langmuir*, vol. 21, no. 9, pp. 4156–4162, 2005.

[75] C. Albayrak, G. Gülten, and Ö. Dag, “Phase Separation in Liquid Crystalline Mesophases of $[Co(H_2O)_6]X_2$:P65 Systems (X = NO_3^-, Cl^-, or ClO_4^-),” *Langmuir*, vol. 23, no. 2, pp. 855–860, 2007.

[76] H. Schmalzried, *Solid State Reactions*. 1981.

[77] V. A. Fedorov, V. A. Ganshin, and Y. N. Korkishko, “Ion Exchange in II–VI Crystals: Thermodynamics, Kinetics, and Technology,” *Phys. status solidi*, vol. 139, no. 9, pp. 9–65, 1993.

[78] H. S. Dong, S. M. Hughes, Y. Yin, and A. P. Alivisatos, “Cation Exchange Reactions in Ionic Nanocrystals,” *Science (80-.).*, vol. 306, no. 5698, pp. 1009–1012, 2004.

[79] J. An and N. L. Rosi, “Tuning MOF CO_2 Adsorption Properties via Cation Exchange,” *J. Am. Chem. Soc.*, vol. 132, no. 16, pp. 5578–5579, 2010.

[80] H. M. Garfinkel and C. B. King, “Ion Concentration and Stress in a Chemically Tempered Glass,” *J. Am. Ceram. Soc.*, vol. 53, no. 12, pp. 686–691, 1970.

[81] W. Smit and H. N. Stein, “Interdiffusion of Hydrogen and Alkali Ions in Glass Surfaces,” *J. Non. Cryst. Solids*, vol. 34, no. 3, pp. 357–370, 1979.

[82] H. Yunqiu, P. H. Duvigneaud, and E. Plumat, “Influence of Anion Groups on Li^+ for Na^+ Exchange in Soda-Lime Glass,” *J. Non. Cryst. Solids*, vol. 127, no. 1, pp. 81–89, 1991.

[83] E. Tunkara and Ö. Dag, “Salt-Acid-Surfactant Lyotropic Liquid Crystalline Mesophases: Synthesis of Highly Transparent Mesoporous Calcium Hydroxyapatite Thin Films,” *Eur. J. Inorg. Chem.*, vol. 2016, no. 13–14, pp. 2114–2121, 2016.

[84] E. Tunkara, C. Albayrak, E. O. Polat, C. Kocabas, and Ö. Dag, “Highly Proton Conductive Phosphoric Acid-Nonionic Surfactant Lyotropic Liquid Crystalline Mesophases and Application in Graphene Optical Modulators,” *ACS Nano*, vol. 8, no. 10, pp. 11007–11012, 2014.

[85] C. Albayrak, A. Cihaner, and Ö. Dag, “Inside Cover: A New, Highly Conductive, Lithium Salt/Nonionic Surfactant, Lyotropic Liquid-Crystalline Mesophase and Its Application (Chem. Eur. J. 14/2012),” *Chem. - A Eur. J.*, vol. 18, no. 14, pp. 4190–4194, 2012.

[86] N. Iyi, F. Geng, and T. Sasaki, “Effect of KBr on the FTIR Spectra of NO_3 − LDHs (Layered Double Hydroxides),” *Chem. Lett.*, vol. 38, no. 8, pp. 808–809, 2009.

[87] N. Ravet *et al.*, “Mechanism of the Fe^{3+} Reduction at Low Temperature for $LiFePO_4$ Synthesis from a Polymeric Additive,” *Chem. Mater.*, vol. 19, no. 1012595–2602, 2007.

[88] M. Thommes *et al.*, “Physisorption of Gases, with Special Reference to the Evaluation of Surface Area and Pore Size Distribution (IUPAC Technical Report),” *Pure Appl. Chem.*, vol. 87, no. 9–10, pp. 1051–1069, 2015.

[89] J. Chen and M. S. Whittingham, “Hydrothermal Synthesis of Lithium Iron Phosphate,” *Electrochem. commun.*, vol. 8, no. 5, pp. 855–858, 2006.

[90] B. Boonchom and R. Baitahe, “Synthesis and Characterization of Nanocrystalline Manganese Pyrophosphate $Mn_2P_2O_7$,” *Mater. Lett.*, vol. 63, no. 26, pp. 2218–2220, 2009.

[91] C. M. Burba and R. Frech, “Raman and FTIR Spectroscopic Study of Li_xFePO_4 ($0 \leq x \leq 1$),” *J. Electrochem. Soc.*, vol. 151, no. 7, pp. A1032–A1038, 2004.

[92] O. Haas, A. Deb, E. J. Cairns, and A. Wokaun, “Synchrotron X-Ray Absorption Study of $LiFePO_4$ Electrodes,” *J. Electrochem. Soc.*, vol. 152, no. 1, pp. A191–A196, 2004.

[93] M. D. Wirt, I. Sagi, E. Chen, S. M. Frisbie, R. Lee, and M. R. Chance, “Geometric Conformations of Intermediates of B12 Catalysis by X-Ray Edge Spectroscopy: Co(I) B12, Co(II) B12, and Base-Off Adenosylcobalamin,” *J. Am. Chem. Soc.*, vol. 113, no. 14, pp. 5299–5304, 1991.

[94] T. Hibino, K. Kobayashi, M. Nagao, and S. Kawasaki, “High-Temperature Supercapacitor with a Proton-Conducting Metal Pyrophosphate Electrolyte,” *Sci. Rep.*, vol. 5, p. 1,7, 2015.

[95] R. K. B. Gover, N. D. Withers, S. Allen, R. L. Withers, and J. S. O. Evans,

"Structure and Phase Transitions of SnP_2O_7," *J. Solid State Chem.*, vol. 166, no. 1, pp. 42–48, 2002.

[96] Y. Jin, Y. Shen, and T. Hibino, "Proton Conduction in Metal Pyrophosphates (MP_2O_7) at Intermediate Temperatures," *J. Mater. Chem.*, vol. 20, pp. 6214–6217, 2010.

[97] A. Ait Salah *et al.*, "FTIR Features of Lithium-Iron Phosphates as Electrode Materials for Rechargeable Lithium Batteries," *Spectrochim. Acta - Part A Mol. Biomol. Spectrosc.*, vol. 65, pp. 1007–1013, 2006.